THE MOTILITY AND CHEMOTACTIC RESPONSE OF *ESCHERICHIA COLI*

by

Corey N. Dominick

BS in Physics, Pennsylvania State University, 2013

MS in Physics, University of Pittsburgh, 2016

Submitted to the Graduate Faculty of

the Dietrich School of Arts and Sciences in partial fulfillment

of the requirements for the degree of

Doctor of Philosophy

University of Pittsburgh

2020

UNIVERSITY OF PITTSBURGH

DIETRICH SCHOOL OF ARTS AND SCIENCES

This dissertation was presented

by

Corey N. Dominick

It was defended on

January 21st 2020

and approved by

Xiao-Lun Wu, Department of Physics and Astronomy

Hanna Salman, Department of Physics and Astronomy

David Jasnow, Department of Physics and Astronomy

Vittorio Paolone, Department of Physics and Astronomy

Jeffrey Lawrence, Department of Biological Science

Dissertation Director: Xiao-Lun Wu, Department of Physics and Astronomy

THE MOTILITY AND CHEMOTACTIC RESPONSE OF *ESCHERICHIA COLI*

Corey N. Dominick, PhD

University of Pittsburgh, 2020

We have studied several aspects of the chemotactic network of *Escherichia coli*, as well as the motility of these cells near solid surfaces. In the first chapter, we develop a novel assay for our research that takes advantage of a "self-trapping" phenomenon in which fully motile bacteria rotate in place at a solid boundary. We then use this assay to study the chemotactic and thermotactic response to impulse stimuli, quantifying the response of the bacteria to heat and serine. In addition, our data illustrates the amplification in the chemotactic network and the motor.

We provide evidence that CheZ is actively regulated in its role as the network phosphatase. In chapter 4, we further study the impulse response at the lower limit of attractant concentrations and find that bacteria are capable of sensing and responding to single molecules of amino acids. Our data is compared to existing models with the aid of a calculation of diffusion inside the cell. The fit of the model is further improved under a modification inspired by our finding that CheZ is actively regulated. Finally we use our self-trapping assay to understand transitions between the run and tumble states in wild-type bacteria, and show that a single filament organizes the flagella bundle and drives the transitions between the run and tumble states of bacterial swimming.

TABLE OF CONTENTS

LIST OF TABLES

LIST OF FIGURES

1.0   INTRODUCTION

In the second half of the 20th century, *Escherichia coli* became a model bacteria for the biophysical study of microorganisms. The cells are rod shaped, peritrichously flagellated, and fast growing: division in as little as 20 minutes is possible in favorable conditions. *E. coli* are chemoheterotrophic, requiring a carbon, nitrogen and a chemical energy source, such as sugars or amino acids for growth. These bacteria are typically 3 to 5 μm long by 1 μm wide and have a double layered cell membrane (gram negative) as illustrated in Fig 1 C. Their natural habitat is in the guts of mammals.

1.1   THE TAXIS OF *Echerichia coli* AT THE BEHAVIORAL LEVEL

1.1.1   Motility

Simple observation of *E. coli* cells in liquid samples showed that individual cells typically swim at speeds of 20-30 μm/s. Cells swim in the direction of the long axis of the cell body and trajectories are generally slightly curved paths that are interrupted by brief but significant changes in direction. See Fig. 1 B for an example of a typical single cell trajectory. The straight segments have become known as "runs" and have an average duration of $\sim$ 1 s. The abrupt changes in direction that separate the runs, known as "twiddles" or "tumbles", are significantly shorter than runs, with an average duration of $\sim$ 0.2 s. The tumbles are random in nature, thus individual cells, in the absence of the external stimuli discussed below, perform random walks in their environment.

The motion of these bacteria is driven by an average of 4 flagella per cell [1], which are up to 8 μm in length. Each flagellum is connected to a rotary motor via a flexible hook, which has a length of 55 nm [2]. The filaments are semi-rigid, and when unstressed form left-handed helices with a pitch of $\sim$ 2 μm [3]. When motors of the cell turn counter-clockwise (CCW), the filaments produce a thrust and torque that act to collect the flagella together

1

into a bundle and the cell runs [4]. A bacterium in a run state is illustrated in Fig. 1 C. The tumble state of the cell was originally thought to be a highly coordinated reversal of the motors to the clockwise (CW) direction [4, 5]. Such a reversal will disorder the bundle and cause each flagellum to act independently, producing a random reorientation of the cell body. Studies using fluorescently labeled flagella in combination with dark-field microscopy revealed that tumbles may be produced with as little as a single motor reversal [3, 6].

1.1.2   Stimulation Directed Taxis of *E coli*

Stimulus directed motion of bacteria was first observed in the late 19$^{\text{th}}$ century when it was noticed that motile cells accumulated near air bubbles in liquid samples [7]. Subsequent studies by Pfeffer, and independently, Engelmann determined that many species of bacteria were either attracted to, or repelled from, oxygen. They observed that the random walk performed by individual cells becomes biased in the presence of oxygen or other chemicals. The net effect is an increased concentration of motile cells in favorable regions. These experiments were often performed in capillary tubes, and the resulting accumulation was macroscopically visible as sharp bands along the length of the tube. Thermotaxis, the movement of bacteria along a temperature gradient, was observed in 1920 by Metzner when bacteria accumulated near a heated wire placed in a liquid sample [7].

Chemotaxis in *E. coli* was studied extensively in the 1960's and 1970's by Julius Adler. This organism was chosen because there was already a knowledge of the biochemistry and genetics [8]. Specifically, the behavior of the bacteria in response to numerous stimuli was quantified, including oxygen [9], amino acids [10], sugars [11], and pH [9]. These experiments were performed by examining the bulk migration of cells either in liquid samples or on solid agar plates. Adler also performed an extensive study of chemorepellents to *E. coli* [12]. Much of the work on this subject since then has focused on the molecular details of the chemotaxis network, and the mechanisms by which cells sense and respond to their environment.

1.2   THE CHEMOTACTIC NETWORK OF *E coli*

The chemotaxis network of bacteria is essentially a computation device. The inputs of the device are external stimuli, such as chemical effectors or temperature changes, and internal feedbacks from the cell's memory. The output is the kinase activity, or the rate of modification of the chemotaxis signaling protein from CheY to CheY-p. In one extreme, the input of a strong attractant will result in a net negative output, i.e. rapidly decreasing the concentration of CheY-p inside the cell. The other extreme is the opposite, with strong repellents sharply increasing concentration of CheY-p. In a steady state, the output rate is slightly positive, resulting in a net production of CheY-p. This net production is balanced by the slow spontaneous decay of CheY-p into CheY.

The molecular details of this network are well understood and are summarized here in Fig. 2. The principle components are the membrane bound chemoreceptors. The chemoreceptors extend through the inner membrane of the cell and sense chemoeffectors in the periplasm. The receptor conformation is thought to exist in two conformation states, either "active" or "inactive" [13]. The information is relayed to CheA through the membrane via this conformation change. The kinase CheA is a hetero-dimer of two forms: a long form with a terminal domain that transfers a phospho-group to CheY, and a short form that does not have the terminal domain but instead binds to CheW. CheA and CheW bind to the chemoreceptors to create a highly stable structure, which is discussed further below. CheA dimers that are bound to receptors in the active state phosphorphylate CheY, whereas CheA bound to inactive receptors does not. The role of CheZ is as the phosphoryl-sink and catalyses the decay of CheY-p to CheY. It is assumed in the literature that CheZ is constitutively active, dephophorylating CheY-p at a rate that is independent of the rest of the network. In this work we provide evidence that CheZ is actively regulated in a similar fashion to CheA (see Ch. 3).

A hallmark of the network is its ability to adapt to a changing environment. For example, a bacterium exposed to a step increase in chemoattractant will immediately respond by increasing the time spent in the run state. However the run duration will return to a pre-stimulus level after some time, and the cell reverts to normal run/tumble behavior [14].

This is known as *adaptation.* The adaptation acts at the level of the receptors via 4 methylation sites per receptor. The addition of methyl groups to these sites shifts the equilibrium toward the active state, and the removal shifts the equilibrium toward the inactive state. Methylation of the receptors is accomplished via CheR and the de-methylation via CheB. CheR preferentially interacts with receptors in the inactive state, providing a feedback based on the current state of the receptors. CheB, which preferentially interacts with inactive receptors, competes with CheY for phosphorlyation from CheA thus providing a feedback from the output side of the network.

1.2.1   The Receptor Cluster

The two most abundant receptors in *E. coli* are the serine receptor, Tsr and the aspartate receptor, Tar. These two receptors make up the majority (>90%) of chemoreceptors in a single cell [15]. There are 3 other types of receptor: Trg for sensing ribose and galactose, Tap for sensing dipeptides, and Aer that senses oxygen. The receptor molecules themselves form homodimers, with two identical monomers forming a functional receptor. When embedded into the cell wall of *E. coli*, these dimers form mixed arrays at one or both cell poles [16, 17, 18, 13] rather than becoming distributed randomly about the cell. These extended arrays recruit CheW, CheA, and CheZ [19], with this grouping being required for fully functional chemotaxis. The smallest "functional unit" capable of all of the functions of chemotaxis is 2 trimers of receptor dimers, 2 CheW, and 1 CheA dimer [20].

Calculations involving only the physics of diffusion show that a concentration measurement by a bacterium is made most accurate by placing receptors randomly about the cell, and that grouping them together greatly reduces the accuracy [21]. The current understanding is that receptors cluster together not to affect the accuracy of measurement but in an effort to increase the gain of the chemotactic network [22, 23, 24]. In this way, the receptors act like spins in an Ising magnet with the concentration of attractant acting as the random external field. In the limit of strong coupling (low temperature), the activity (magnetization) becomes a very steep function of chemoattractant concentration (field). Although the qualitative idea is thought to be settled, the exact details are still unclear. For example, it

4

is not known the extent to which receptors affect their neighbors, or how far along the array the receptor state is correlated. It is also unclear if the coupling within the array is fixed once assembled, or if it is a dynamic process that changes with environmental conditions.

In chapter 4 we examine the bacterial behavior response in the limit of very low chemoattractant concentrations, where coupling between neighboring receptors is required to produce a large enough perturbation to the CheY-p concentration in the cell to be detected in our measurement. We find that the network is sensitive enough to respond to single attractant molecules, and that the coupling among receptor types is very heterogeneous.

1.3   THE ROTARY MOTOR OF *E. coli*

Each flagellum of an *E. coli* cell is attached at its base to a rotary motor. The fact that each flagellum undergoes true rotation was hypothesized by multiple scientists and argued for strongly by Berg and Anderson in 1973 [25]. Because of their small diameter (~ 10 nm), the filaments are difficult to image by normal optical microscopy, requiring either electron microscopy, which requires fixed samples or high intensity dark-field microscopy. Although dark-field microscopy has been used effectively, this technique was unable to resolve the mechanism by which helical waves propagated along the filaments. The first experiment to prove that the flagella undergo true rotation was performed by Silverman and Simon in 1974 [26]. In this study, antibodies to the hook protein were mixed with mutant cell cultures that produced hooks without filaments. The result was that hooks became attached to glass microscope slides, and the cell bodies rotated about the "tethered" motor. Tethering cells by a single motor has since evolved into a standard technique in the field, and was first used to study chemotaxis by Larsen et. al. in 1974 [27].

The motor alone is a remarkable nano-machine. Figure 3 shows an illustration as well as an electron micrograph. Under normal conditions, the rotor spins at ~ 120 Hz and generates ~ 1000 pN nm of torque [6]. In a similar way to the receptor array, the switching of the direction of the motor is driven by highly allosteric interactions at the motor base. The effect is a steep dependence of the motor direction on the concentration of CheY-p. In appendix

B.2 (Fig. 41) we plot the data from Ref. [28] that shows this sharp switch. In this way, the motor senses the output of the chemotactic network. For a single flagellum, the picture is clear: a low concentration of CheY-p causes a CCW rotating motor (as viewed from outside the cell), whereas a high concentration causes a CW rotating motor. Since the attached filament is a left handed helix, the CCW rotation will push the cell forward.

The current understanding of how a cell's flagella behave during run and tumble states began with Macnab in the 1970's [4, 5]. Using dark field-microscopy with a high intensity light source, he was able to visualize and photograph the flagella of swimming bacteria [29, 30]. The main observation was that running cells have a coherent flagellar bundle that drives the cell forward, as displayed in Fig 4 A. When a cell was observed to tumble, the bundle would destabilize and individual filaments could be seen extending in random directions, which is shown in Fig. 4 B. The explanation for these observations is that the various motors on a cell rotate coherently: When all motors rotate counter-clockwise (CCW), the left handed helical filaments bundle together. In the opposite case, all motors turn clockwise (CW) and a bundle is unable to form. This painted a conceptual picture that CCW motors were in a "run" state and CW motors were in a "tumble" state.

The transitions between these states, however, are still not well understood. In 1983 two studies that monitored multiple motors on single cells established that in the absence of chemotactic stimuli, there is no global synchronization mechanism of the multiple motors [31, 32]. This provides a paradox when combined with the fact that the CCW bias, or the probability of rotating CCW, of a single motor is typically between 50% and 80%. If the motors are not correlated, and the rotation direction probability is split nearly evenly, then one should expect that a coherent CCW bundle is a rare event. In light of this finding, Macnab proposed that the synchronicity of motors was enforced mechanically via the inter-action of the filaments. In this scheme, a motor would alter its switching rate in response to a mechanical change at the motor. Evidence for such a "mechano-sensing" mechanism was found in 2003 by Fahrner et.al. who observed that the rate of switching of a motor from CW to CCW increased significantly as the load on the motor decreased [33]. However, it is not clear if motor is sensing load or the rotation speed.

A more recent study again looked at the simultaneous rotation of multiple motors on

single cells [34]. This study used small microspheres as markers to track motor rotation, and found a moderate degree of correlation between nearby motors on the same cell. The authors suggested this to be evidence of global regulation by fluctuations in CheY-P concentration. However, authors of a theoretical study on the same data disagree and claim that mechano-sensing is a more plausible explanation [35]. In this work (Ch. 6) we provide evidence that supports the idea that one of the filaments of the cell acts to organize flagella into bundles.
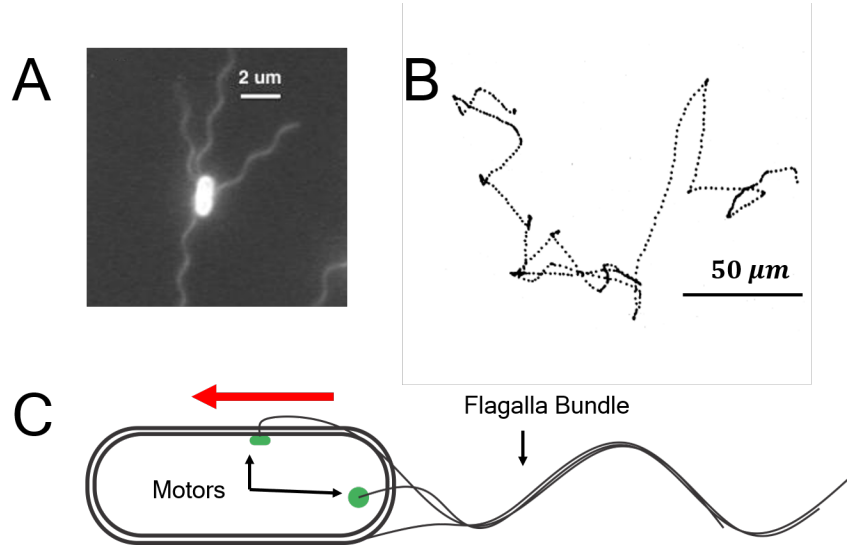
Figure 1: The Size, Shape and Motility Pattern of *Escherichia coli.* A) a fluorescently labeled cell has been immobilized to a glass surface and imaged. Four filaments can be seen extending away from the cell body. B) A track from a single cell swimming in 3 dimensions. This 30 second trajectory clearly shows the run and tumble behavior. C) An *E coli* cell is shown in a run state. The CCW turning flagella have bundled together to propel the bacterium in the direction of the long axis. The red arrow designates the direction of motion of the cell body. A) is from Fig. 2A of ref. [3] and B) is from Fig. 1 of ref. [36].
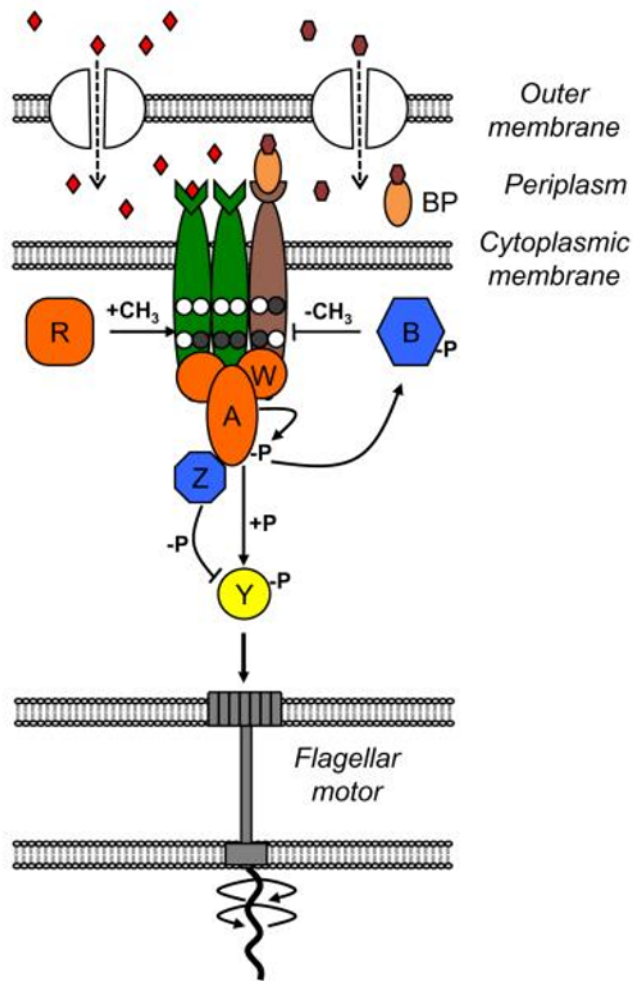
Figure 2: Summary of The Chemotaxis Network of *E coli*. The receptors extend through the inner membrane of the cell. These receptors bind to chemoeffector ligands (red diamonds) or small molecules (orange ovals) in the periplasm. The receptors are bound to CheW, and adapter protein, and CheA, the kinase. CheA can transfer a phosphor group to CheY, and CheZ can dephosphorylate CheY-p. CheR acts to methylate inactive receptors, and CheB de-methylates inactive receptors. The signaling protein, CheY, diffuses throughout the cytoplasm, and in its active form, can cause a switch in motor direction. This image is from Fig. 1 of ref. [37]

9
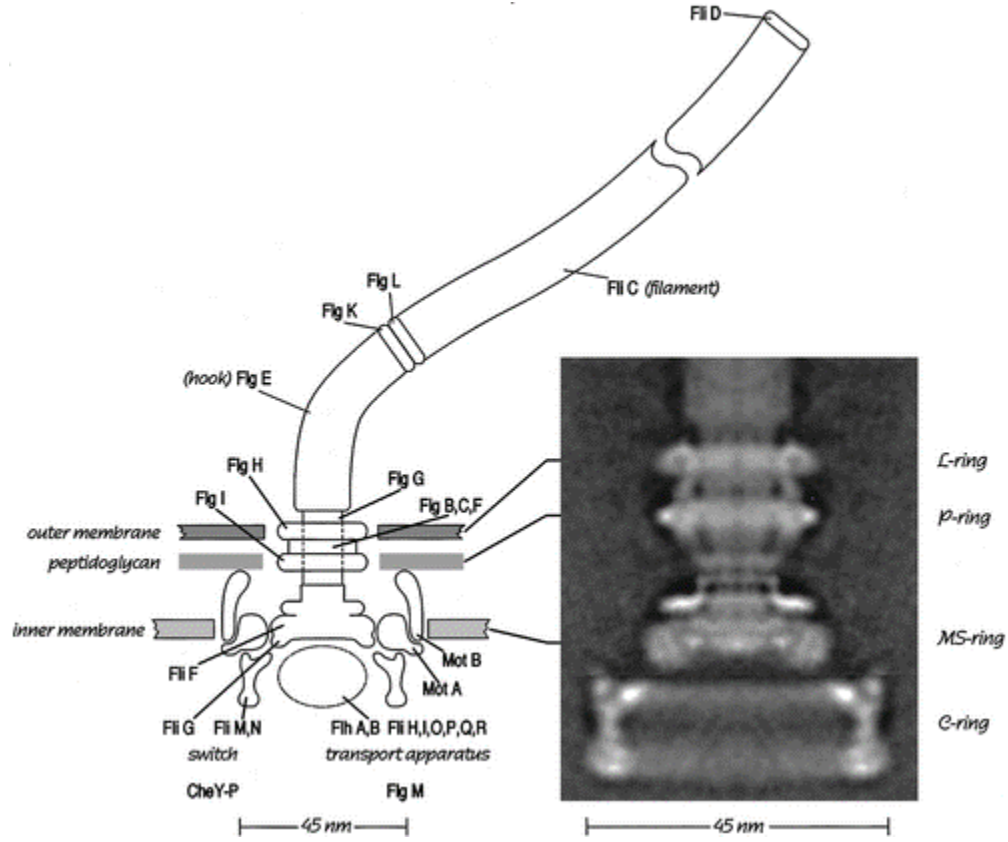
Figure 3: The Rotary Motor of *E coli*. The illustration shows the bacteria motor embedded within the membrane. The labels in normal font denote the proteins that comprise, whereas italic labels denote the features or function. The L-and p-rings serve as bushings between the rotating motor shaft and the membranes. The MS-ring is the rotor, and the C-ring is the switching apparatus. The inset is an average micrograph (100 samples) of the flagella motor with the rings labeled. This image is Fig. 1 from Ref. [38]
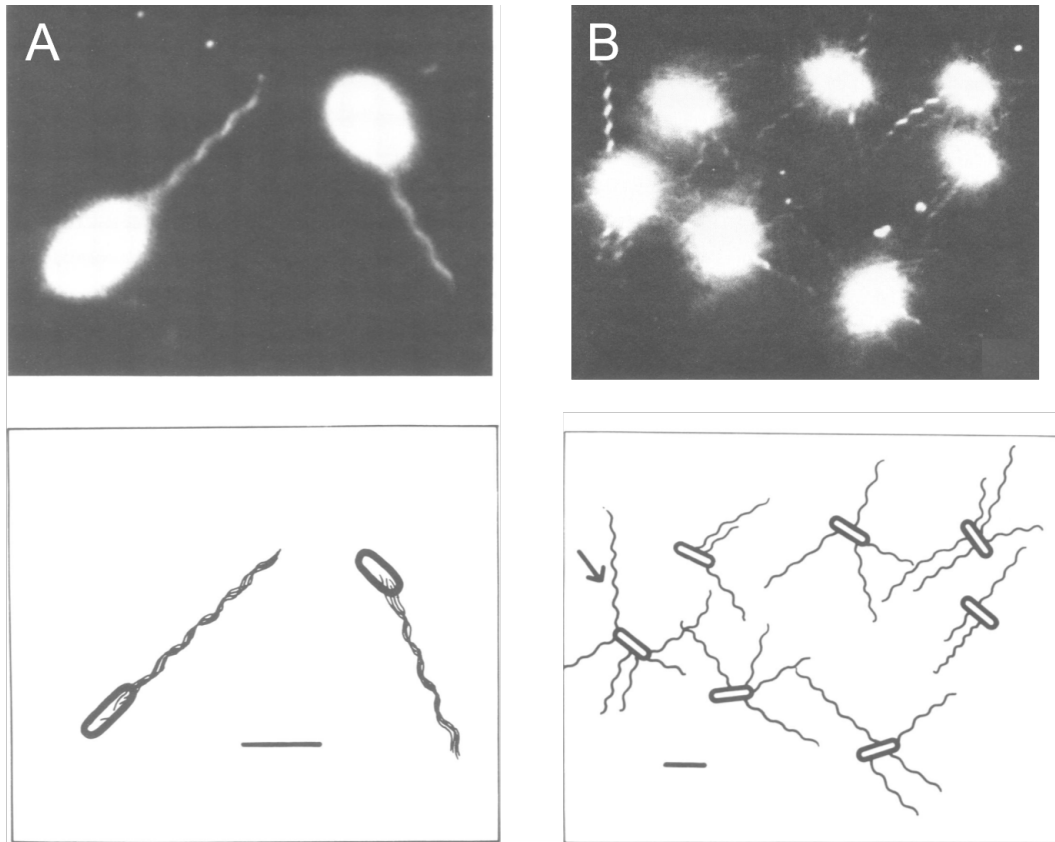
Figure 4: Filaments in A Run State vs A Tumble State. These images were captured by Macnab in 1976 using dark field microscopy [30]. Panel (A) shows an image of two swimming (running) bacteria. The cell bodies produces a large flare, but a single helical bundle of in-phase filaments is seen extending behind the each cell. These bacteria were only exposed to the yellow portion of the arc lamp illumination. The lower image is a drawing by Macnab that clearly shows individual filaments. (B) This image shows the result of exposing the bacteria to the full spectrum of the arc lamp. The cells tumble as a result, and now filaments are clearly seen extending in random directions.

2.0 ROTATING BACTERIA ON SOLID SURFACES

Much of the experimental findings in this work were aided by the use of the observation chamber in figure 5, in combination with an inverted microscope (TE300; Nikon). The chamber is open to air and contains liquid ~ 8 mm in depth, with samples viewed from below. This allows an experimenter to administer chemicals or heat from above to stimulate bacteria while observing or recording via the microscope. All experiments using this chamber were conducted with the focus near ($< 10\,\mu$m) the planar glass surface.

A swimming bacterium is hydrodynamically attracted to a solid surface due to its own image [39]. This attractive force is the reason that many cells swim close to a surface [40] and some of them eventually become immobile. Surface localization is a first step for bacteria to change lifestyles from planktonic to colony forming. This switch provides bacteria with many advantages, such as being close to a nutrient source where organic materials are deposited [41] or spatial refuge where bacteria are protected by a heterogeneous environment [42]. A fascinating example is *Caulobacter crescentus* that alternates between stalked and motile cell phenotypes and is able to adapt to both aqueous and surface environments.

When wild-type (*wt E. coli*) RP437 were introduced into the observation chamber, there was an excess of bacteria swimming near the glass surface. Viewing under our inverted microscope or via the video system shows that most of these bacterial trajectories are smooth and arc in the clockwise (CW) direction. When observing from above the solid surface, CW turning trajectories are expected with *E coli* [43, 44, 45] and are a result of flagellar bundles being left-handed helices and turning in the counter-clockwise (CCW) direction during a run interval. An example of a typical cell trajectory from near the surface in our chamber is shown in Fig. 6. Even though samples on our system are viewed from below, the optics are such that samples viewed through the microscope, appear, in a directional sense, as if viewed from above. In other words, letters written on a microscope slide and placed on the microscope face up would read normally if viewed through the eyepiece. Thus when *E coli* were introduced into the observation chamber, most motile cells have trajectories that were smooth and arc in the clockwise (CW) direction, as expected due to the presence of the

surface [43, 44, 45].

In addition to free swimming cells, we observed many motile cells that spun in place about a fixed axis at the surface of the glass. Herein we describe this particular subgroup of motile cells, and show that this effect, which we named "self-Trapping", can be effectively used as an assay to study bacterial behavior.

2.1   THE SELF-TRAPPING PHENOMENON

The motion of the self-trapped (ST) cells is reminiscent of single motor tethering, which has become a commonly used technique for studying *E. coli* chemotaxis [26, 46]. In the tethering assay, the flagella of the bacteria are sheared short and a single flagellar stub is adhered to the glass surface as depicted in Fig. 9 A. The resulting rotation of the cell body effectively reports the rotation direction of the tethered motor. We constructed a strain specifically to use the tethering assay: XLWU100 was obtained by deletion of the flagellar protein fliC from the wild-type (WT) strain RP437 (see appendix A.1 for details). This new strain was then transformed with the plasmid pFD313, which encodes a mutant 'sticky" version of fliC that adheres to glass.

If ST cells were tethered by a single flagellum, one would expect the rotation to be split between the CCW and CW directions according to the CCW bias of the motor. This is indeed what we observed using XLWU100 as shown in Fig. 7 G-I. However the WT bacteria in our experiment were overwhelmingly biased in the CW direction; most of them are in the CW state $\sim 90\%$ of the time. Use of the smooth swimming mutant RP5232 confirmed that ST cells were not tethered by a single motor as surface rotating mutants exclusively turned in the CW direction. The major difference between ST wild-type (RP437) and RP5232 is the temporal fluctuations of the cell-body rotation velocity, $\Omega(t)$. For WT bacteria, $\Omega(t)$ varies widely over time and its probability density function (PDF) $P(\Omega)$ is bimodal as shown in Fig. 7 A-C. On the other hand, $\Omega(t)$ for RP5232 fluctuates less and $P(\Omega)$ is unimodal as displayed in Fig. 7 D-F.

In addition to observing the smooth swimming mutant, another experiment was per-

formed in which a micropipette filled with $5\,\mu$M serine, a strong chemoattractant, was used to stimulate surface rotating cells. All WT bacteria tested rotated steadily CW in response to the attractant. The same experiment was performed on tethered XLWU100 and resulted in the opposite effect: tethered bacteria rotated steadily CCW in response to attractant.

To determine the location of the flagella of ST bacteria, we implemented a modified version of the classical Ryu flagella staining technique [47] (see appendix A.2.1 for details). Ryu flagellar stain forms a precipitate on the flagella, increasing their effective size and allowing flagella to be visible under standard microscopy. Our new technique allows a pre-selected bacterium to be stained in real-time, making visible the flagella that drive the motion. Some of our results are presented in Fig. 8. Surprisingly, most ST cells were found to have numerous long flagella, many of which extended away from the glass surface as displayed in Fig. 8 A. This result led us to conclude that ST bacteria form flagellar bundles that extend normal to the surface, as illustrated in Fig. 9 B. Bundles rotating CCW would result in a counter-rotating cell body, i.e., CW, which is consistent with our observations.

We note that nearly all stained WT cells have flagella oriented in random directions, analogous to Fig. 8 A. We believe that this is due to cells tumbling in response to the stain. This is plausible because the stain contains ethanol, a known repellent for *E coli* [12], and phenol, which sometimes acts as a repellent [12, 48]. This hypothesis is further supported by the staining of smooth-swimming RP5232, with the results showing a flagellar bundle extending away from each cell body (Fig. 8 B).

2.2   THE USE OF SELF TRAPPING AS AN ASSAY

Based on our observations, it seems feasible that self-trapped cells can be used, in a similar fashion as the classical rotation assay, to study bacterial swimming and responses to external stimuli. In addition to being simple experimentally, the advantage of our technique is that one can use intact cells directly without chemical and biological modifications. Consequently the conditions a cell experiences in our assay are less contrived, i.e., cells have a functional flagellar bundle and the motors are under near physiological load.

The goal of our assay is to determine the "rotation state", $\omega(t_i)$, for a single cell given that we have the rotation speed, $\Omega(t_i)$ (Fig 10 A). Here, t_i denotes a discrete time point, i.e., a frame from a video recording, where $t_i - t_{i-1} = 20$ ms. To begin, we make the simple assertion that the slow and fast rotation states seen in the PDFs of ST cells correspond to the "tumble" and "run" states, respectively. For each cell, a normalized histogram of Ω is constructed and fit with a bimodal distribution:

$$P(\Omega) = P_t(\Omega) + P_r(\Omega) = A_t e^{-c_t(\Omega - b_t)^2} + A_r e^{-c_r(\Omega - b_r)^2} \, , \tag{2.1}$$

where $b_t < b_r$. Two thresholds, Ω_t and Ω_r, are defined by $P_t(\Omega_t)/P(\Omega_t) = 0.75$, and $P_r(\Omega_r)/P(\Omega_r) = 0.75$, i.e., the speeds at which the relative probability of being in a particular state is 75% (Fig. 10 B). To assign a rotation state to each speed, we use a two-threshold crossing algorithm adapted from Yuan et al. [49]:

$$\omega(t_i) = \begin{cases} 0 & \text{if } \Omega(t_i) \leq \Omega_t \\ 1 & \text{if } \Omega(t_i) \geq \Omega_r \\ \omega(t_{i-1}) & \text{if } \Omega_t < \Omega(t_i) < \Omega_r \end{cases} \, , \tag{2.2}$$

where CW rotation is defined as $\Omega > 0$. The ambiguity that arises if the first point in a time trace falls between the thresholds is resolved by assigning

$$\omega(t_1) = \begin{cases} 0 & \text{if } P_r(\Omega(t_1)) \leq P_t(\Omega(t_1)) \\ 1 & \text{if otherwise} \end{cases} \, .$$

Any error caused by assigning the first point is likely to be resolved within $1s$, which is the decay time of the autocorrelation of a typical $\omega(t_i)$ trace. For this reason, all stimulation experiments begin at least $1s$ after the start of a recording. An example of the application of this algorithm for a typical WT cell is shown in Fig. 10 C.

15

To test this idea, two separate experiments were conducted using chemical and temperature stimulation with XLWU100 tethered cells as a comparison. The well separated rotation states of tethered bacteria allow us to simply set ω based on the motor direction:

$$\omega(t_i) = \begin{cases} 1 & \text{if } \Omega(t_i) \leq 0 \\ 0 & \text{if } \Omega(t_i) > 0 \end{cases}. \tag{2.3}$$

Note that we define the CW direction to be positive for both assays, which explains why the negative direction is the "run" direction for tethered cells.

2.3 RESULTS

It was found during preliminary experiments that some surface bound rotating bacteria exhibit various effects that make them unsuitable for measurement, such as periodic stops in the rotation or precession of the rotation axis. To exclude these deleterious effects, we adopted the following criteria for choosing cells in a measurement:

1. the candidate cell rotates freely without periodic stops,

2. the pitch of the cell body with respect to the glass surface should not noticeably change during rotation, and

3. the average speed of the cell should be above a threshold, which we set to be 2 Hz.

Individual cells meeting these criteria were found and recorded at least 10 times for 10 seconds each during which a single stimulation pulse was delivered at $t = 1\,\text{s}$.

We found that there is a noticeable difference in the steady-state bias Φ_0 for RP437 and XLWU100, ~ 0.75 to 0.8 for the former and ~ 0.5 to 0.7 for the latter, as shown in the insets of Fig. 11. However, upon stimulation, $\Phi(t)$ changes in a time-dependent manner, and the responses of the two bacteria appear similar as delineated in Fig. 11. Here the changes in the bias $\Delta\Phi(t) \equiv \Phi(t) - \Phi_0$, normalized by their maximum values $\Delta\Phi_{max}$, are plotted as a function of time. It is seen that immediately after the application of chemical stimulation, $\Delta\Phi(t)/\Delta\Phi_{max}$ increases and plateaus for about $1\,\text{s}$ before decaying. The persistent time,

under serine stimulation, for XLWU100 is slightly longer than *wt* RP437 which is possibly due to the fact that a flagellar motor in XLWU100 experiences a higher load than that of RP437. This is consistent with Ref. [49], which shows that under a high load the motor increases it's dwell times for both CW and CCW intervals, but significantly more so for CW than CCW. Our measurements therefore support the notion that a cell's response to a chemical stimulus is not entirely determined by the chemotaxis network alone; rather the load on the motor contributes as well. In addition, there is a sharp decrease in bias of RP437 during the serine pulse at $t = 1s$. Because this decrease is not seen for XLWU100, nor for temperature pulsing on RP437, we believe that the brief velocity field caused by serine stimulation disrupts the flagella bundle enough to measurably affect the cell body rotation.

Aside from these differences, we found that there is general agreement between measurements using the two strains, e.g. (i) $\Delta\Phi(t)$ are biphasic displaying a large positive response followed by a slow negative response, and (ii) $\Delta\Phi(t)$ recovers the pre-stimulation level in long times for both cases. These measurements demonstrate that self-trapped rotating cells can be used to measure response functions of bacteria to external stimuli. In our new assay, the cell-body rotation is driven by multiple flagella with a reduced load on individual motors, and hence the chemotactic behavior is expected to be closer to a free-swimming state. The measurements are somewhat noisier for the trapped RP437 than for tethered XLWU100, but such noise can be reduced if more cells are included in the average.

Finally we demonstrated that our assay can also be used to study thermal response of RP437, which is displayed in Fig.11 B. In this case, repetitive short heat pulses, $50\,\mathrm{ms}$ in duration, were delivered to surface-bound rotating bacteria using an IR laser (see A.3). Each pulse causes a transient temperature change of $\Delta T \simeq 5\,^o\mathrm{C}$, which relaxes very rapidly due to localized heating by a small optical fiber tip and the large thermal diffusivity of water $(D_T = 1.46{\times}10^5\,\mu\mathrm{m}^2/\mathrm{s})$ at room temperature. Despite a much faster thermal relaxation time the response function nevertheless appears very similar to when the same RP437 bacteria were stimulated by serine.

The precise timing employed in this measurement also reveals a clear delay in bacterial response and the applied pulses. Inspection of Fig. 11 shows that the delay is not restricted

to temperature but to chemical stimulation as well. Interestingly, we found that the delay time of $\sim 150 \pm 10\,\mathrm{ms}$ is about the same for both cases after accounting for the time delay of the serine pulse. This observation rules out the possibility that the delay is a result of diffusion of stimulants outside of the cell. The delay, however, is consistent with diffusion of regulator protein CheY-p, which a previous *in vivo* measurement shows $D_{cheY} \simeq 4.6\,\mu\mathrm{m}^2/\mathrm{s}$ in RP437 [28]. For a typical bacterium of size $L \simeq 3\,\mu\mathrm{m}$, the diffusion time, estimated according to $\tau = (L/2)^2/2D_{CheY}$, is about $250\,\mathrm{ms}$ and is order-of-magnitude consistent with our observation.

2.3.1 Discussion

These experiments show that the self-trapping phenomenon can be used as a simple, yet effective, assay for studying the tactic behavior of *E. coli*. We will use this assay in two of the following chapters: in Ch. 3 to quantify the chemotactic behavior in response to low doses of serine and temperature, and in Ch. 6 to examine the switching statistics at the whole-cell level. Despite the successes we have demonstrated with this technique, we posit that the main strength of our technique may be used to study microorganisms for which the standard methods, e.g. using antibodies, are unavailable or too costly to develop. Since it is a hydrodynamic effect assisted by the planar symmetry of the boundary, we believe that bacterial self trapping should be a general phenomenon. Indeed spinning giant bacteria *T. majus* were observed to form two-dimensional crystals on a glass surface [50] and *V. alginolyticus* were found to exhibit localized surface spinning motion [51].

To this end, we attempted to find self-trapped cells using *Bacillus subtilis*, a peritrichously fllaggelated, rod shaped, gram positive bacteria [52]. Because of the similarities in shape and flagellation, we hoped that these cells would readily trap at the surface in a similar manner to *E. coli*. Despite good mobility in the cultures tested and numerous cells swimming in curved paths at the surface, we found no self-trapped cells (see A.1 for culture details). We hypothesize that the difference may be due to the fact that bacillus has many flagella (~ 20 per cell, compared to ~ 5 for *E. coli*) arranged in a grid-like pattern [53]. We were unable to carry out additional experiments to test our hypothesis, however we believe that

understanding the difference between these bacteria would provide important clues about how the spacial organization of flagella effects motility near surfaces.

2.4   FIGURES
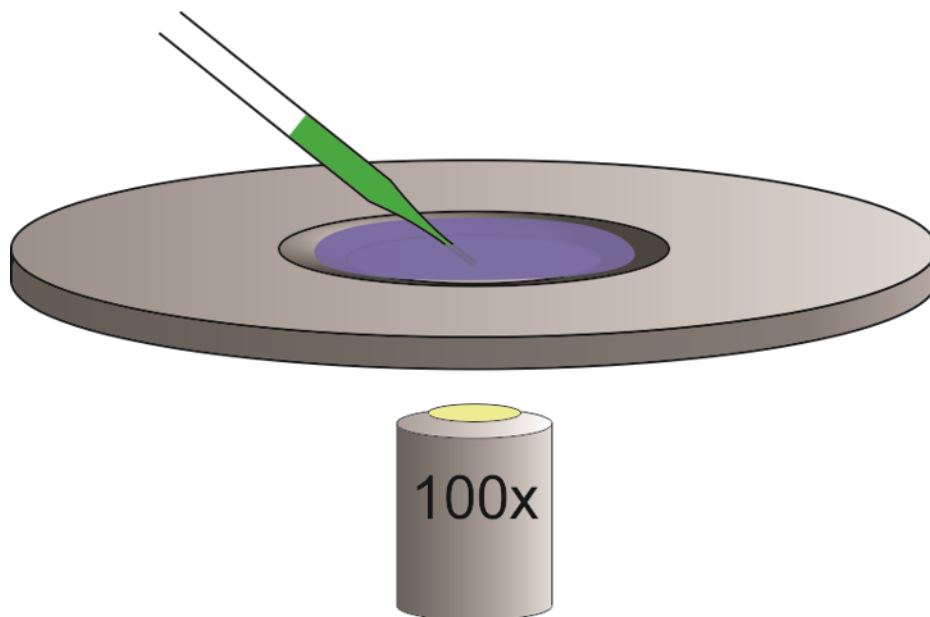
Figure 5: The Observation Chamber. The chamber fits into the standard stage of the microscope, and is viewed here in place over the microscope objective and a micropipette in place. The coverglass, 25 mm in diameter, serves as the "floor" of the chamber, and seals against a gasket to make the chamber water-tight. The gasket is held against the glass by a delrin ring. This chamber was machined by Matt Shtrahman for use in his dissertation work [54].
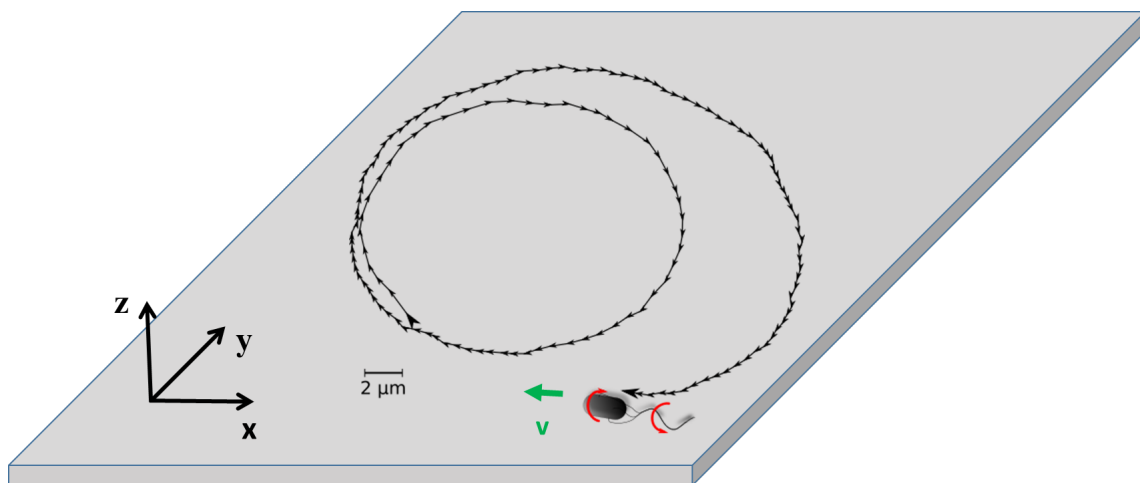
Figure 6: An Example of a Bacterial Trajectory Near a Planar Surface. An *E. coli* cell swims near the glass surface of our observation chamber. Arrows in the trajectory indicate the position at 30 ms intervals and the direction of motion. A depiction of the cell is shown at the end of the trajectory with red arrows showing the direction of rotation of the cell body and flagella bundle.
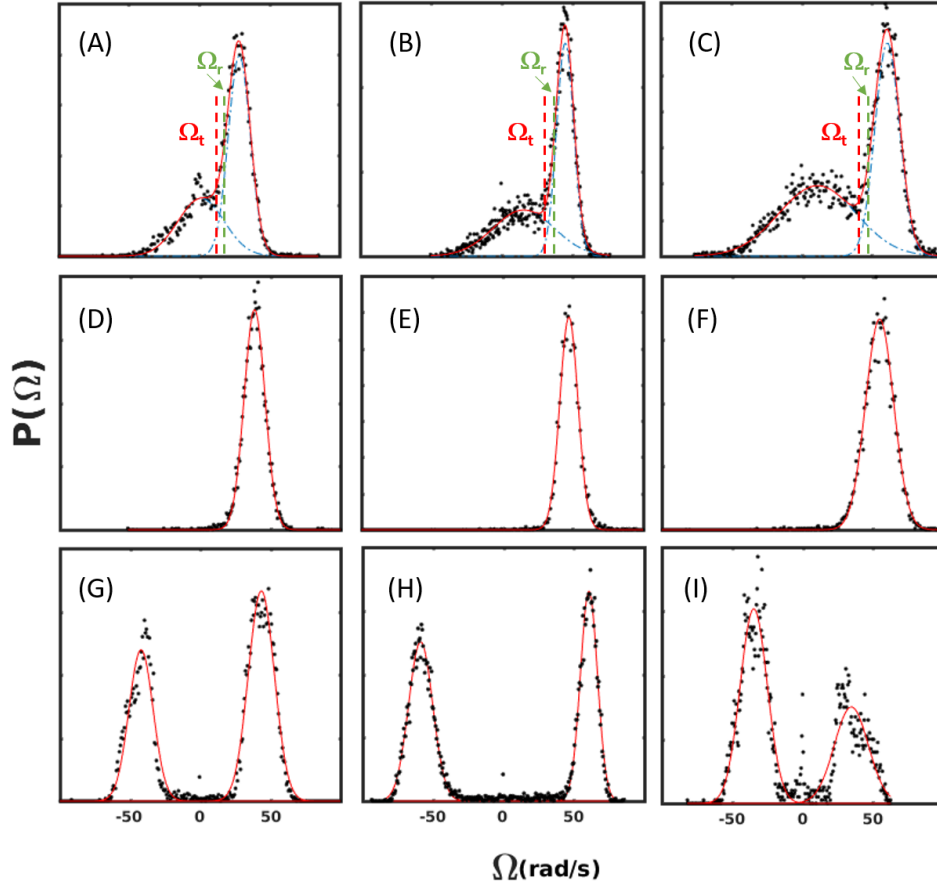
Figure 7: Examples of Typical Rotation Speed PDFs. In all figures, black dots are normalized histograms of the rotational speed of the body of a single surface-rotating bacterium, and red lines are fits. The details of cell recording and PDF construction are presented in appendix A.4. (A-C) Wild-type trapped cells have speed distributions that are well fit by a sum of two Gaussian distributions. The thresholds for the run and tumble states are marked by Ω_r and Ω_t, respectively, and are explained in section 2.2 . (D-F) Trapped ΔCheY (smooth-swimming) bacteria only rotate CW, and with PDFs that are well fit by a single Gaussian (red lines). (G-I) Cells that are tethered via a single motor show two well separated rotation states, that are both Gaussian distributed in speed (red lines). In all cases, we define CW to be positive rotation.
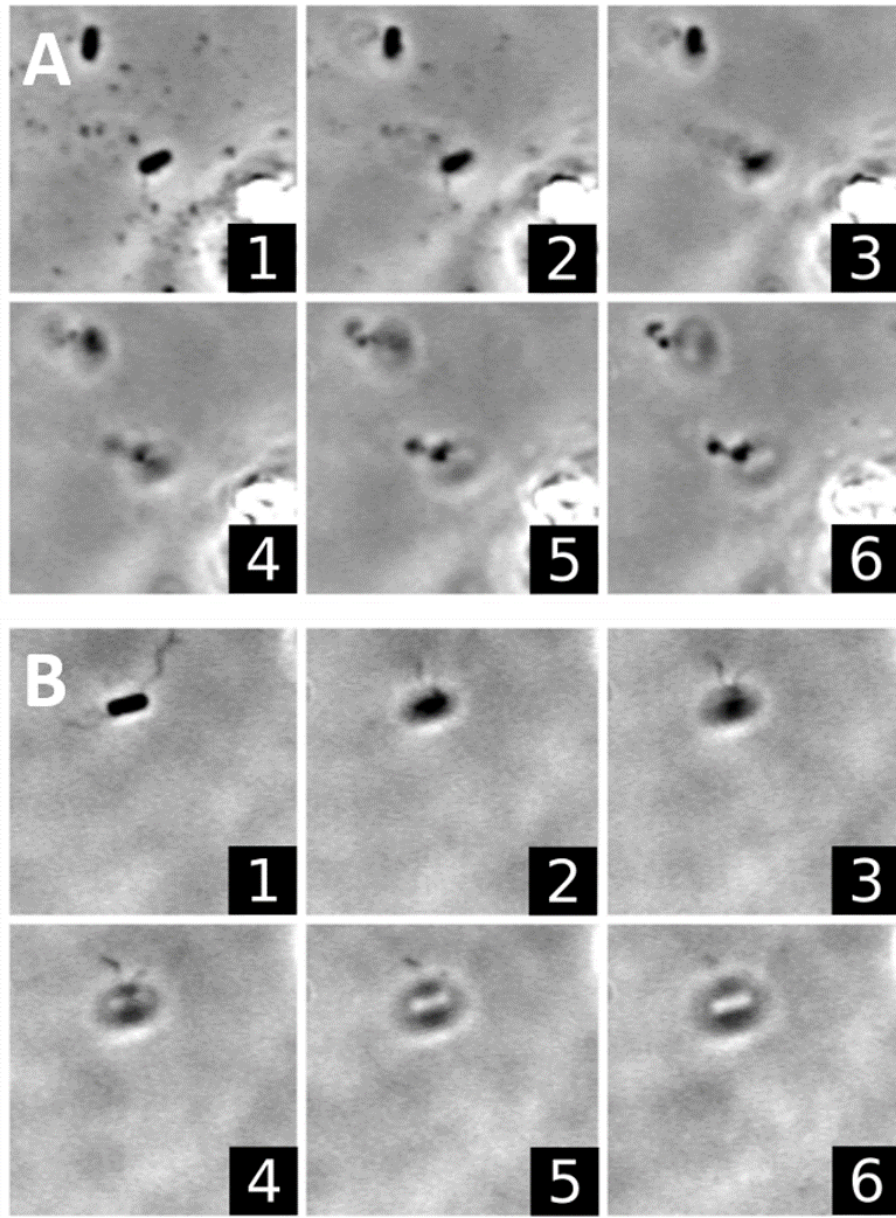
Figure 8: Images of Flagellar Staining. Previously trapped, rotating bacteria were stained. Numbers indicate successive images as the focus is increased in the vertical direction. A) shows two typical RP5232 Δ CheY after staining. Both cells were rotating in the clockwise direction before being immobilized, and appear to have a single flagellum or single flagella bundle. B) An analogous sequence of images for a wild-type RP437 trapped cell. This particular cell showed bi-directional rotation before staining and has multiple long flagella.
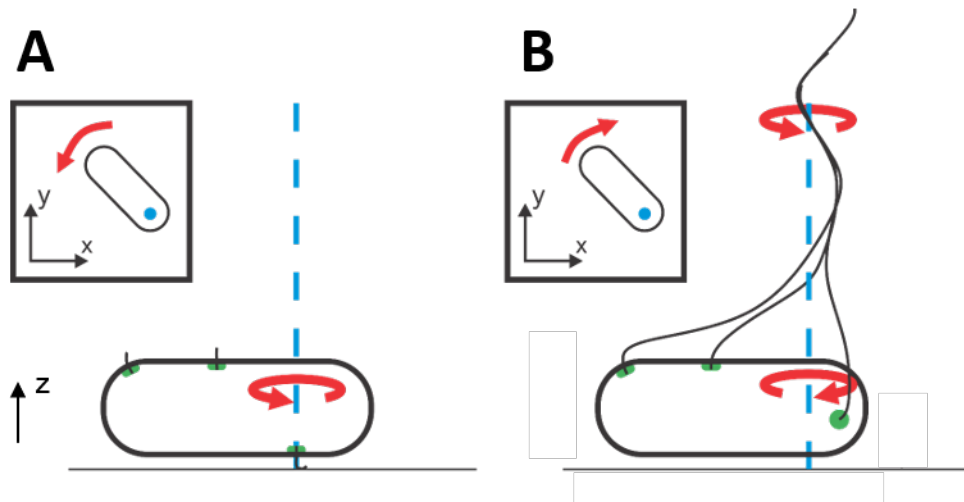
Figure 9: *E. coli* Can Rotate About a Fixed Axis at a Planar Surface in Two Distinct Ways. A) A tethered cell has a single flagellar motor adhered to the surface. When viewed from above (inset), the cell body will rotate in the same direction as the motor, *i.e.* a CCW rotating motor will produce a CCW rotating cell body. The blue dashed line (dot in inset) indicates the rotation axis, and the red arrows indicate the direction of rotation in a "run" state. B) A cell in a trapped state has a flagellar bundle that forms perpendicular to the cell body. A run caused by a CCW rotating bundle will produce a CW counter-rotating cell body.
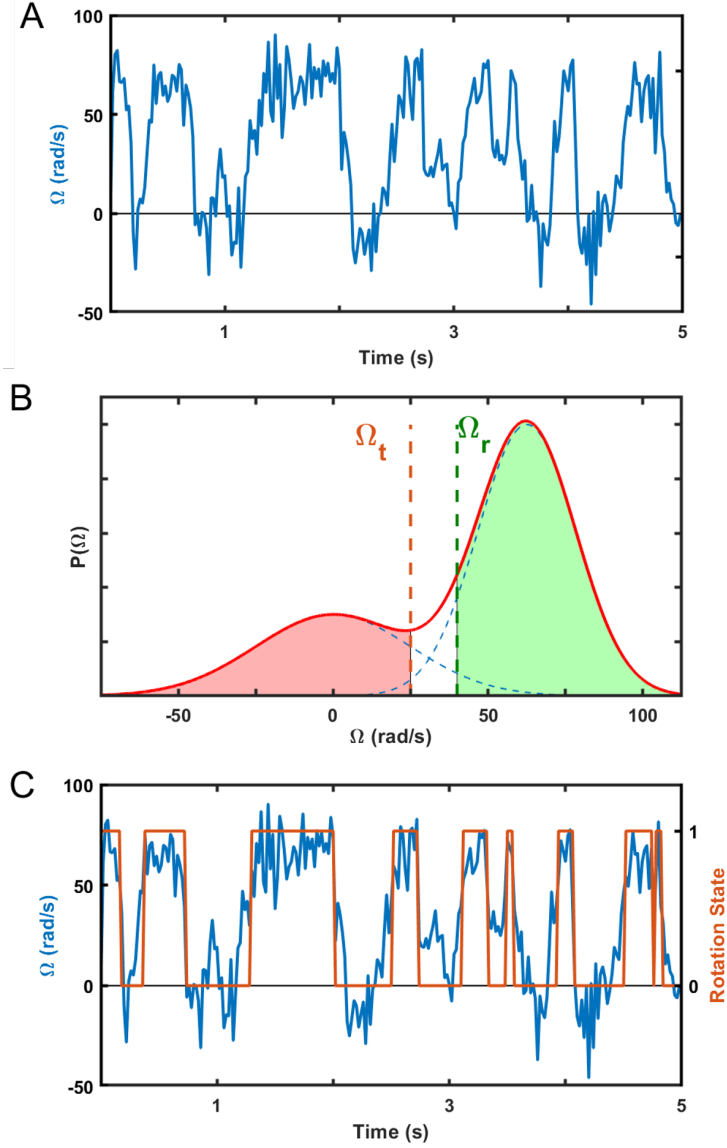
Figure 10: Creating a Rotation State Trace from an Angular Velocity Trace. A) A portion of the angular velocity, $\Omega(t)$, of a typical trapped cell. B) The probability density, $P(\Omega) = P_t(\Omega) + P_r(\Omega)$, is denoted in red, with the individual Gaussian functions, $P_t(\Omega)$ and $P_r(\Omega)$, denoted by blue dashed lines. Any point in the velocity trace that lies in the green (red) region will be assigned to "run" ("tumble"). Points that lie in the center region are assigned to whichever state was assigned to the last point prior. The boundaries of these regions are determined by the cutoff frequencies, Ω_t and Ω_r. C) The resulting rotation state (orange) superimposed over the angular velocity.
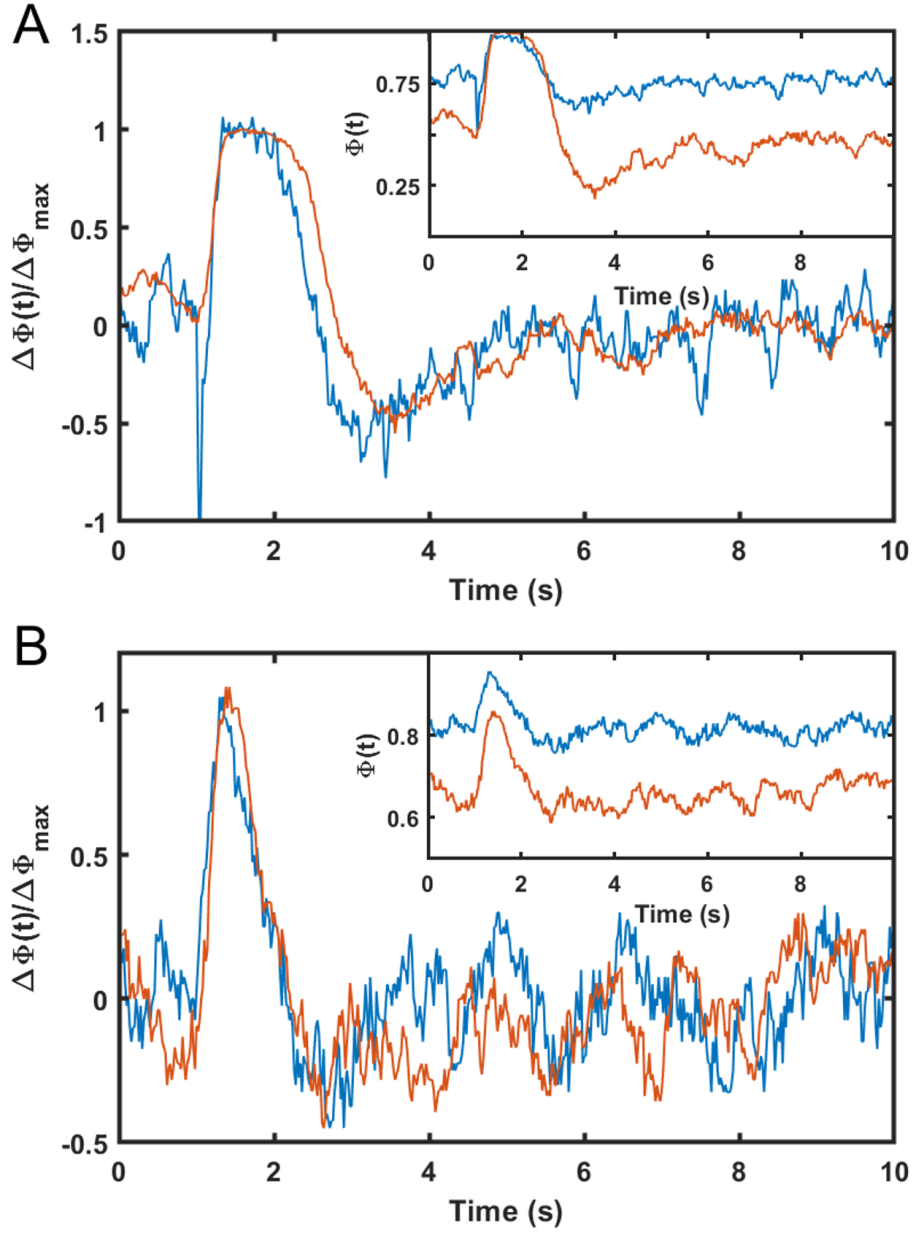
Figure 11: A Comparison Between the Tethering and Trapping Assays. A) The main figure shows the scaled, population averaged change in CCW bias, $\Delta\Phi(t)/\Delta\Phi_{max}$ for trapped cells (blue curve) and tethered cells (red curve) in response to a 25ms pulse from a micropipette containing $5\,\mu M$ serine, delivered at $t = 1s$. The flow induced by the pulse perturbs the trapped cells' flagella creating a sharp dip in the bias of the blue curve. The inset shows the same data without normalization. Colors denote the same information as in the main figure. B) The analogous figure as part A, but with a $\sim 8^oC$ temperature pulse instead of serine.

25

3.0   ON THE CHEMOTACTIC AND THERMOTACTIC RESPONSE OF
Escherichia coli

In this chapter we report new findings of bacterial response to impulsive chemical and thermal stimuli. We adopt the simple view that the bacterial chemotaxis network is a central signal processing unit with multiple inputs and a single output. One question of practical importance is the relative strength of the chemical and thermal signals reaching the processing unit. Also, if given two different stimuli of the same (equivalent) strength, are the signals being processed in the same way? In order to address these questions, we studied *E. coli's* response to serine and temperature stimulation at a physiological level by measuring the rotation bias of a cell body. This allowed us to establish an equivalent dosage of the two stimuli. We also studied *E. coli*'s response at a molecular level by measuring the interaction between the regulator protein CheY-p and its phosphatase CheZ using a fluorescent energy transfer (FRET) technique.

The FRET system we used was constructed by Sourjik and Berg[22] and has since been used in various studies [17, 55, 56]. Briefly, yellow fluorescent protein (YFP) and cyan fluorescent protein (CFP) are fused, via a flexible linker of 5 glycines, to the N-terminal of CheY and CheZ, respectively. These protein fusions are encoded on a single plasmid under a lac operon promoter [17]. Since the emission spectrum of CFP significantly overlaps with the excitation spectum of YFP, there is energy transfer from CFP to YFP when these molecules are close (within ~ 10 nm) [57, 58]. When energy transfer occurs from CFP to YFP, emission of cyan decreases and emission of yellow increases. Because of the very short interaction distance, there is almost no energy transfer when the chemotaxis proteins CheY and CheZ are not interacting. Thus the interaction between the proteins CheY and CheZ may be monitored via the changes in intensity of the fluorescent labels.

Our impulsive stimulation technique reveals subtle features of phosphatase activity that were not observed when a step-wise stimulation protocol was implemented [56]. Specifically, we found that both the physiological response and the FRET response are sigmoidal as a function of serine concentration C_p. However, the inflection points of the two curves differ

by more than a decade in concentration. In other words, the maximum bacterial behavioral response to serine stimulation is more than ten times lower than the maximum FRET response. Most interestingly, over the physiologically permissible range, $\Delta T <\sim 22\,^\circ\mathrm{C}$, temperature stimulation elicits no FRET response. Taken together we conclude that there are two biochemical pathways for phosphatase activity in *E. coli*, one passive and one active. The passive pathway dephosphorylates CheY-p constitutively. The active pathway, on the other hand, is regulated by the chemoreceptor clusters, which upon stimulation by a chemoattractant, but not by temperature, causes a significant number of CheY to dissociate from the cluster. This finding modifies the conventional belief that CheZ is a passive component in the chemotaxis network, and it also explains why CheZ is closely associated with chemoreceptors.

3.1 RESULTS

In order to understand how different input signals are integrated by the *E. coli* sensory system, we first attempted to establish a quantitative relationship between the responses due to stimulation by heat and by a chemoattractant. Specifically, we questioned whether there exists an equivalent dosage of heat for a given chemical stimulus, and if so, what will be its numerical value. For this purpose we conducted a comparative study by monitoring the change in CCW bias $\Delta\Phi$ when a known amount of the chemoattractant serine is impulsively delivered to individual *E. coli* cells. The measurements were then repeated using impulsive temperature stimulation by laser heating. The pulse widths in both measurements were kept fixed and the amplitudes of the pulses were changed systematically. Fig. 12 displays the data, where the red and blue filled circles are for temperature and chemical stimulation, respectively. It is seen that after a proper normalization, $\Delta\Phi/\Delta\Phi_0$, C_p/C^* and $\Delta T/\Delta T^*$, the two sets of data follow the same trend with the threshold values being $C^* = 7\,\mathrm{nM}$ and $\Delta T^* = 0.26\,^0C$, where $\Delta\Phi_0 \equiv 1 - \Phi_0$ and Φ_0 is the mean CCW bias in the absence of stimulation. Here, ΔT is the peak temperature change from the background of 23^oC and C_p denotes the peak serine concentration with zero background.

27

Our measurement shows that it is indeed feasible to compare in quantitative terms two very different types of stimuli, and the threshold values can serve as natural scales for different stimulation intensities employed in an experiment. We also note that the very low threshold value for serine, $C^* = 7\,\mathrm{nM}$, or ~ 10 serine molecules in the volume of a bacterium suggests that *E. coli* may be capable of single molecule detection.

Fig. 12 shows that when stimulated weakly, $\Delta\Phi/\Delta\Phi_0$ vs. C_p/C^* and $\Delta T/\Delta T^*$ are linear when plotted on the linear-log graph, which is typical for a sensory system obeying the Weber-Fechner law. This linear regime spans about one decade in concentration or temperature before the signal saturates at $\Delta\Phi/\Delta\Phi_0 \simeq 1$.

To investigate how the bacterial flagellar motor switch is regulated by the receptor cluster, we carried out molecular FRET measurements. Bacteria that display a bright puncta at a pole were selected and stimulated impulsively, as in the rotation assay. Fig. 13 shows typical FRET measurements using serine at different concentrations C_0 ranging from 1 to $100\,\mu\mathrm{M}$. The curves are relative cyan fluorescence intensity changes, $\Delta I(t)/I_0$, of receptor arrays where CheZ-CFP proteins are localized. Here I_0 is the steady-state value. Since the measurement is focused at individual receptor arrays, the time-dependent intensity directly reports the degree of dissociation at the molecular complexes of phospho-CheY-YFP and CheZ-CFP after a stimulation pulse, which is delivered at $t = 1.8\,\mathrm{s}$.

The FRET response curves in Fig. 13 display a systematic dose dependence, showing (i) an increase in amplitude and (ii) broadening in response as the dosage increases. As a function of time the response curves also display a consistent trend, i.e., after the stimulation pulse, the fluorescence intensity increases rapidly in a short time, reaches a peak value, and then decays monotonically to the pre-stimulation level. Unlike CheY-p concentration in a cell that shows a biphasic response, the FRET signals display no under-shoot in long times before returning to the pre-stimulation level. We noticed that while the initial rate of intensity increase is independent of the stimulation level C_p, the decay phase strongly depends on it. From the data, the short rising time was determined to be $t_s \simeq 0.24\,\mathrm{s}$, which is more-or-less constant throughout the concentration range tested, and the long relaxation times t_l, measured by the half-width-at-half-height of the FRET response, are concentration dependent as displayed in the inset of Fig. 14. In theoretical models, such as Ref. [23],

it is assumed that dephosphorylation rate t_p^{-1} is constant, and our observation of constant t_s lends support to such an assertion. The long relaxation time t_l in our measurement can be associated with the adaptation time t_m of the chemotaxis network and is governed by methylation kinetics. In addition, our measurement shows that t_l is a linear function of the stimulation level C_p. This point is discussed further in section 3.2.3.

A quantity of considerable interest to this experiment is how the amplitude of the FRET signal changes as the serine concentration C_p is varied. This allows one to see the connection between molecular events that take place at the receptor level and motor bias that underpins the chemotaxis behavior of a cell. In Fig. 12, the peak FRET signal $\Delta I / \Delta I_{max}$ vs. C_p/C^* is plotted along side the behavior (rotational bias) data. This signal also has a sigmoid form similar to the $\Delta \Phi / \Delta \Phi_0$ vs. C_p/C^*, but the inflection point in this case is shifted to a much larger value, i.e., $C_I \simeq 1\,\mu M$ versus $30\,nM$ for the behavioral data. We note the inflection point in our FRET measurement is about a factor of three lower than that reported in Ref. [17], where stimulation was stepwise instead of impulsive, raising the interesting possibility that this value may depend on how bacteria are stimulated.

We next proceed to investigate the FRET response to impulsive heating over a broad range of temperature increments, $6 < \Delta T / \Delta T^* \leq 80$. Despite the large physiological responses seen in this temperature range, or even lower, we were very surprised to find that there is no detectable change in cyan fluorescent intensity, which is delineated in Fig. 13 (B) by the open red circles. Hence there is a sharp contrast in the FRET signals when the temperature stimulation data is plotted along side the chemical stimulation data as in the figure. One observes in Fig. 12 that over the reduced concentration range $10 < C_p/C^* < 10^3$ where FRET displays a significant increase, the physiologically equivalent temperature "dosage" over the same range elicits no FRET signal at all. We therefore conclude that unlike chemical stimulation, modulation of CCW bias in a temperature perturbation is not a result of a change in dephosphorylation activity of chemoreceptors. In other words, phosphatase activity of CheZ is passive for temperature stimulation but is active for chemical stimulation.

3.2 DISCUSSION

3.2.1 One- and Two-Stage Signal Amplification

A conspicuous feature of the data in Fig. 12 is that the sigmoidal curve for the FRET measurement is shifted, compared to the bias measurement, to a much higher serine concentration. We interpret the two sigmoidal curves as a result of two-stage amplification of bacterial chemotaxis network. The first stage of amplification is at the receptor level. For our impulsive chemical stimulation with zero background, the operating point or the maximum sensitivity of the receptor is set at about $1 \, \mu M$, which is the inflection point of the FRET curve. The second stage of amplification occurs at the motor level and its maximum response, for the zero background measurement, occurs at about 40 nM in serine concentration. The sharp S-shaped curve indicates that only a small change in ligand concentration is sufficient to saturate the motor bias, even though this has little effect on the FRET signal. The large dislocation of the two curves in Fig. 13 therefore implies a large signal amplification, $\Delta Y/C_p$, of the receptor cluster, giving rise to the high sensitivity of *E. coli* to its chemical environment.

We also notice that a discernible FRET signal is detected only when the motor bias is close to saturation $\Delta\Phi/\Delta\Phi_0 \simeq 1$. This indicates that regulation by adaption is not fully engaged until the motor is saturated. However, it is unclear whether the status of the motor is actively fed back to the receptors or the chemotaxis network is "hardwired" in this fashion.

3.2.2 Bacterial Thermo- and Chemo-tactic Responses

It is a remarkable fact that impulsive stimulation by serine induces a readily observable FRET signal whereas a similar stimulation by temperature has no effect. If the FRET signal reports only the kinase activity of the receptor cluster via a change in CheY-p concentration, as suggested previously [22], one expects to see a FRET signal regardless of the stimulation type. However, this is not the case in our experiment. In Fig. 14 we present the behavioral bias of bacteria when stimulated impulsively by temperature (red curve) and by serine (blue curve). We note that after the data is normalized and averaged, the two different stimuli

elicit nearly an identical response, showing a large positive peak followed by a small negative lobe. The behaviors are therefore biphasic in both cases.

While the biphasic response due to a chemical stimulation is well documented and appears to agree with theoretical models [59], the temperature stimulation is more subtle. Herein we attempt to explain our data in Fig. 14 using the theory put forth by Jiang et al. [60] and by Paulick et al. [56]. The basic idea is that the activity a of the receptor cluster obeys an equation that is akin to the Fermi-Dirac function given by,

$$a = \frac{1}{1 + \exp\left(N(f_m + f_L)\right)}, \tag{3.1}$$

where N is the number of receptors in an active cluster, f_m and f_L are respectively the free energies of methylation and ligand binding per receptor. This result is obtained using the Monod-Wyman-Changeux (MWC) approximation for receptors with four different states [61, 23]. When a bacterium is subject to a step-wise stimulus and assuming there is only one relaxation time t_m, the change in activity relaxes according to,

$$\Delta a(t) = \Delta a_0 \, e^{-\frac{t}{t_m}}, \tag{3.2}$$

where Δa_0 is the change in activity immediately after the stimulus. For temperature stimulation, f_L is constant and Δa_0 depends on a change in the methylation free energy Δf_m with the result $\Delta a_0 = -N a_0 (1 - a_0) \Delta f_m$. On the other hand, for chemical stimulation, f_m remains constant immediately after the stimulus, and Δa_0 depends on a change in the binding free energy $\Delta f_L = \ln\left((1 + C_p/k_I)/(1 + C_p/k_A)\right)$ resulting in $\Delta a_0 = -N a_0 (1 - a_0) \Delta f_L$. In the above a_0 is the steady-state activity, and k_I and k_A are dissociation constants of an inactive and active receptor, respectively.

The CheY-p concentration in a cell obeys the equation,

$$\frac{dY}{dt} = k_a a - \frac{Y}{t_z}, \tag{3.3}$$

where k_a is the rate of phosphorylation and t_z^{-1} is the rate of dephosphorylation. The steady-state of CheY-p concentration is given by $Y_0 = k_a t_z a_0$ whereas its time dependence after the step-wise stimulation can be solved using Eqs. 3.2 and 3.3 with the result,

$$\Delta Y(t) \equiv Y(t) - Y_0 = k_a \Delta a_0 \frac{t_z t_m}{t_m - t_z} \left(e^{-\frac{t}{t_m}} - e^{-\frac{t}{t_z}}\right). \tag{3.4}$$

31

It follows that for an impulsive stimulation, the CheY-p concentration change is the time derivative of the above expression,

$$\frac{\partial \Delta Y(t)}{\partial t} = -k_a \Delta a_0 \frac{t_z t_m}{t_m - t_z} \left(\frac{1}{t_m} e^{-\frac{t}{t_m}} - \frac{1}{t_z} e^{-\frac{t}{t_z}} \right). \tag{3.5}$$

Equation 3.5 shows that the temporal profile of CheY-p concentration in a cell is biphasic and is independent of the type of stimulation. These predictions are consistent with our measurements displayed in Fig. 14 if the change in bias $\Delta \Phi(t)$ is proportional to $\Delta Y(t)$. There is however an important quantitative difference between the model and our measurements. Namely, the model predicts a perfect adaptation, constrained by $\int_0^\infty \Delta Y(t) dt = 0$. However our measurements in Fig. 14 indicate that the positive part of the motor response is significantly greater than the negative part. Such difference may be explained by the fact that CheY and CheZ in our bacteria are modified by conjugation with YFP and CFP, respectively. Clearly more study is needed for a quantitative comparison between theory and experiment.

The fact that the theoretical models in their current form can qualitatively account for the motor response for both chemical and temperature perturbation is remarkable, suggesting that the theory has captured essential features of bacterial chemotaxis network. On the other hand, it also deepens the mystery found in this experiment, i.e., if actively releasing CheY from the receptor cluster after an impulsive chemical stimulation plays no discernible role at the motor level, why is such a biochemical step present in a cell? We will address this issue in the Summary.

3.2.3   Additivity of Methylation Time Applies to Impulsive Stimulation

For stimulation using stepwise increments, it is experimentally established that the relaxation time $t_m(C)$ due to a single step of size C is a linear sum of two steps $t_m(C_1)$ and $t_m(C_2)$ with $C = C_1 + C_2$ [62, 46]. This is known as the additive rule and it implies that t_m is a linear function of ligand concentration C. Such an effect was explained as a result of the change in the methylation level being proportional to time t with the proportional constant being the maximum rate of methylation [23].

For impulsive stimulation, it is not possible to maintain a constant methylation rate, not to mention being at its maximum value. In our experiment, it is expected that the methylation rate is initially positive and then becomes negative in a longer time before returning to zero. Nevertheless, our measurement shown in the inset of Fig. 13 displays a linear behavior similar to what was observed in stepwise stimulation and thus is also consistent with the additive rule. We believe that the adaptation time t_m being a linear function of ligand concentration could be a general property of bacterial chemotaxis, independent of how a cell is stimulated. However, how this is achieved in a cell remains to be understood.

3.3 SUMMARY

We have performed a comparative study of two different stimuli, chemical (serine) and temperature, impulsively applied to individual *E. coli* bacteria. At the behavioral level, by measuring the CCW bias Φ, we found that the responses determined by $\Delta\Phi/\Delta\Phi_0$ vs. $\log(C_p/C^*)$ in one case, and $\Delta\Phi/\Delta\Phi_0$ vs. $\log(\Delta T/\Delta T^*)$ in the other case, are able to be superimposed, suggesting (i) the bacteria use fold-change detection to process both types of extracellular information, and (ii) a change $\Delta T^* \simeq 0.26\,^oC$ is equivalent to a change $C^* \simeq 7\,\text{nM}$ in serine concentration. Surprisingly, however, at the molecular level, by measuring phosphatase activity of receptor bound CheY-YFP and CheZ-CFP pairs, the two extracellular signals elicit very different responses: For the chemical stimulation, a dose-dependent change in cyan emission is readily observed but no FRET response is seen throughout the entire physiologically permissible temperatures, $1.6 < \Delta T < 22^o\,C$. This observation allows us to draw an important conclusion about the activity of CheZ, i.e., contrary to the conventional wisdom, our measurement shows that phosphatase CheZ is actively regulated by the receptor cluster when stimulated by chemoattractants but not by impulsive heating. Since temperature stimulation induces a response on the motor is similar to chemical stimulation, a reduction in CheY-p concentration must be due to a temporary shutdown of its production in a cell. It implies that when chemically stimulated, a bacterium will not only shutdown CheY-p production, but also boost the activity of CheZ to actively release CheY.

This finding resolves a long-standing puzzle concerning the peculiar fact that in *E. coli*, and perhaps other bacteria as well, the source and sink of CheY-p are in the same location at a cell pole [63, 64, 19]. It has been suggested that such an arrangement allows a more precise control of the overall concentration of CheY-p inside a cell [64]. Sequestering of CheZ on receptor clusters is also consistent with an enhanced phosphatase activity by oligomerization of CheZ found by Blat et al. [65]. Here we show that such organization is necessary for the function of CheZ, i.e., similar to CheY that is phosphorylated by the long form of CheA (CheA$_L$), a large pool of CheZ sequestered at a cell pole is actively regulated by the short form of CheA (CheA$_S$) [15]. In Ref. [15], it is shown that at a cell pole, components of the chemotaxis signaling complex are organized in stoichiometric fashion with CheA$_L$ and CheA$_S$ being dimerized to form a functional unit.

The big puzzle of this study is the fact that despite different behaviors of CheZ seen in our FRET measurements, the motor responses to impulsive temperature and serine stimuli are nearly identical, indicating that active releasing of CheY from the receptor cluster has only a marginal effect on motor switch if at all. This biochemistry step is therefore subtle at the behavioral level and perhaps is the reason it has been overlooked in previous studies. We note however that active release of CheY molecules by the receptor clusters takes place only when the serine level is high, i.e., about an order of magnitude greater than that required for observing a motor response (see Fig. 13). This suggests that this regulation step may be reserved for situations when the external chemical signal is large and motor bias is saturated. By actively releasing CheY from receptor clusters, a pool of substrates for CheA$_L$ is effectively increased, making it possible to replenish the CheY-p concentration during the recovery phase of a chemoresponse. Thus, the mysterious biochemical step may be important for shaping the temporal CheY-p concentration profile in a cell. For implusive temperature stimulation, since the dynamic range required for response is quite narrow compared to chemical stimulation, this biochemical may be omitted. FRET signals have been observed when bacteria are stimulated by a stepwise temperature change [56]. In such a case, the bacterium has ample time to react and the behavior corresponds to a long-time response. Taken together, it suggests that activation of CheA$_S$ requires a minimal time and this time dependence could be an interesting subject for future studies.

We observed that the threshold of temperature sensing for *E. coli* is about $\Delta T^* \simeq 0.26\,^oC$ administrated in a time interval of $\sim 50\,\text{ms}$. This translates to a very large temperature gradient if bacterial temperature sensing is by temporal comparison similar to chemical sensing [66]. This raises the interesting question about its relevance to environments where *E. coli* resides. For a swimming speed of $v_s \simeq 20\,\mu\text{m/s}$ with a mean run interval of $\Delta t \simeq 1\,\text{s}$, this amounts to a spatial gradient of $dT/dx(\geq \Delta T^*/v_s\Delta t) \simeq 100\,^\circ\text{C/cm}$. Such a large gradient is impossible in a bulk fluid. Also due to the large thermal diffusivity of water, which is orders of magnitude greater than diffusivity of small molecules, a bacterium could not outrun thermal diffusion unless its swimming speed is 50 times faster. such a high swimming speed is impossible for flagellated bacteria. It appears, therefore, bacterial thermotaxis must be restricted to special micro environments, such as on animal skins or cavities covered with a thin layer of fluid or mucus. In this case a buffer zone of a stable temperature gradient may be possible, and it can provide cues for taxis. The gradient produced by $\Delta T \simeq 10\,^\circ C$ over a small thickness $\delta = 100\,\mu\text{m}$ or less would be sufficient to trigger a thermotactic response. Alternatively, in order to sense a smaller temperature gradient, say $10\,^\circ\text{C/cm}$, a bacterium may lower its threshold ΔT^* by integrating the temperature signal over a longer time. This interesting possibility again remains to be tested in future experiments.

Many interesting issues remain unanswered and call for further investigation. Aside from a few discussed above, we would also include the following: (i) How are the phosphoryl source and sink regulated for the signaling protein CheY, e.g. their relative phase, strength, and duration in response to impulsive stimulation. (ii) What is the role of sink-source relationship in shaping CheY-p concentration profile inside a cell? It seems that if one treats cell cytosol as a diffusion channel, the CheY-p concentration profile cannot be arbitrary, but optimized for fidelity of signal propagation.

3.4   FIGURES
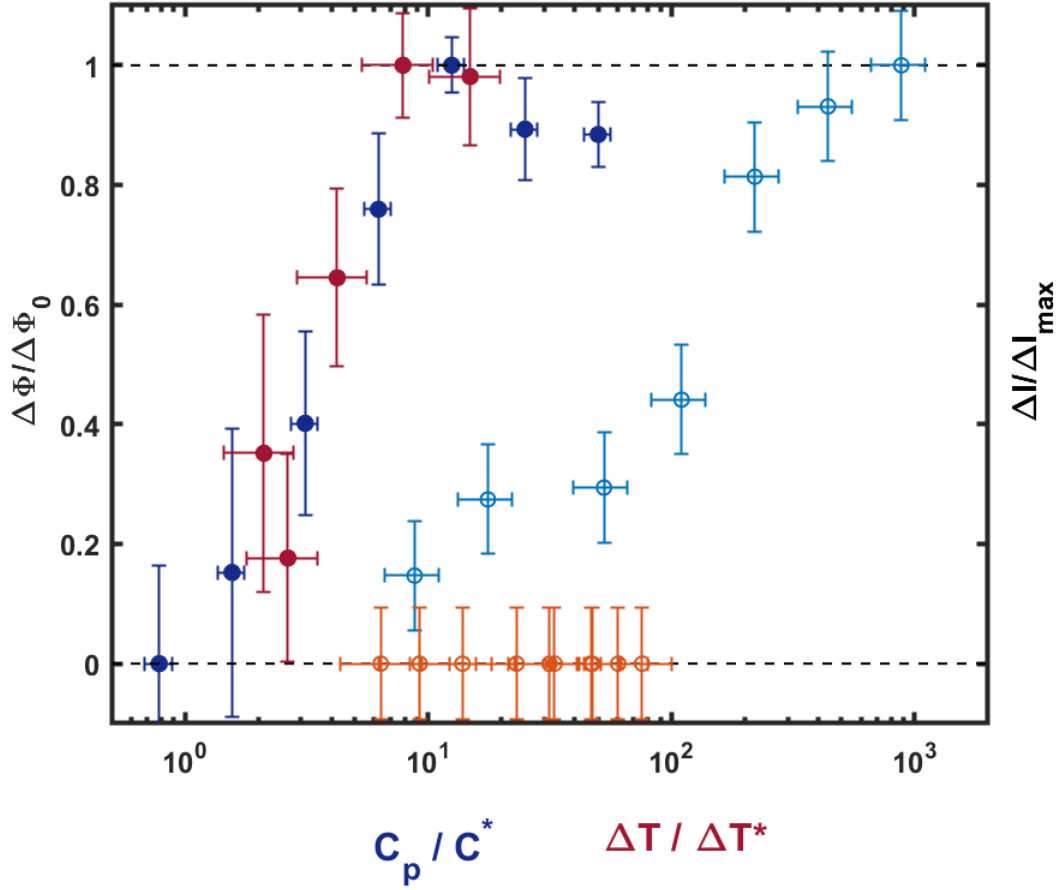
Figure 12: Comparison of Cell's Behavioral Response with the Response at the Molecular Level by FRET. The red and blue symbols in the figure are for temperature and serine stimuli, respectively. The solid symbols are for the behavioral (or CCW bias) measurements and the open symbols are for the FRET measurements. On this linear-log plot, the behavioral data collapses when C_p and ΔT are normalized by their corresponding threshold values $C^* \simeq 7\,\mathrm{nM}$ and $\Delta T^* \simeq 0.26\,^o\mathrm{C}$. However, the FRET response for the two stimuli are considerably different: Whereas the chemical stimulation elicits an expected FRET response as shown by the open blue circles, no FRET signal was observed throughout the entire tested temperature range $6 < \Delta T/\Delta T^* \leq 80$ (or $1.6 < \Delta T < 21\,^o C$), which is indicated by the open red circles. The number of cells used for the rotation measurements is 14 per data point, and the number of cells used for the FRET measurements is about 150 per data point. The uncertainties (the standard error) are shown as the vertical bars for each data points. All curves have been normalized so the maximum value is 1.
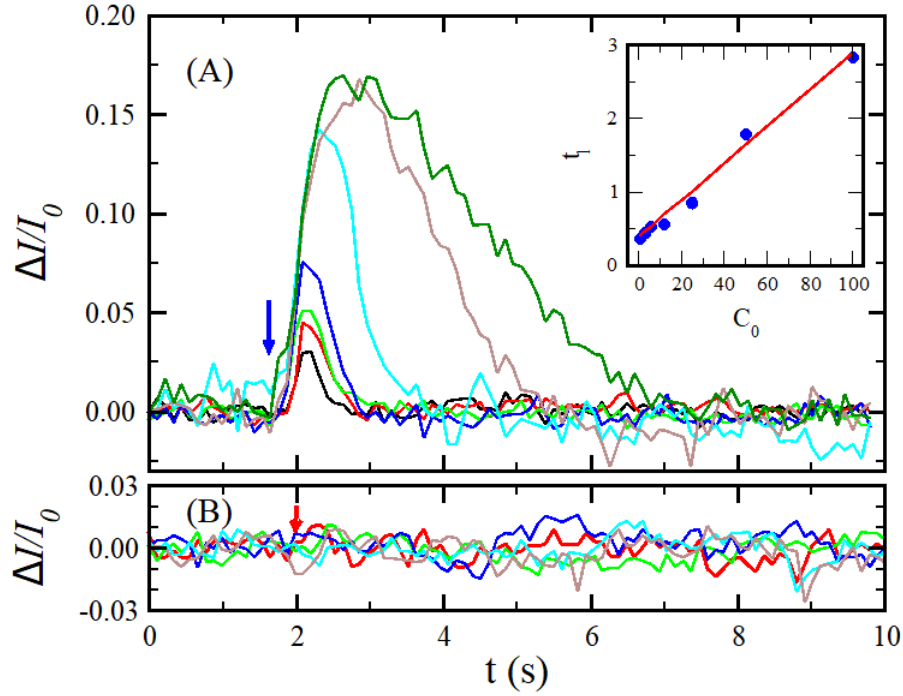
Figure 13: FRET Signals Induced by Serine and Temperature Stimulation. (A) Impulses of different serine concentrations in the micropipette $C_0 = 1$ (black), 3 (red), 6 (light green), 12 (blue), 25 (cyan), 50 (brown), and 100 μM (dark green) were applied at $t = 1.8$ s as indicated by the blue arrow. The concentration change C_p experienced by the bacteria is a factor of 14 smaller. The pulse width is fixed at $\Delta t = 25$ ms. The change in cyan fluorescence intensity $\Delta I(t)$ as a function of time t is normalized by the intensity before the stimulation I_0 and corrected for photobleaching by fitting the beginning and end of the curves with an exponential function. Each curve in the plot represents an average over ~ 200 bacteria. It is seen that after the pulse of serine, the cyan fluorescence intensity increases, reaches a peak, and then declines. We also noticed that both the FRET amplitude and the long-time relaxation time are functions of C_p. The latter, to a very good approximation, has a linear dependence as shown in the inset. (B) Stimulation by different temperature pulses: $\Delta T = 1.7$ (red), 2.4 (light green), 3.6 (blue), 6.0 (cyan), and 8.2 °C (brown), applied at $t = 2.0$ s as indicated by the red arrow. While stimuli of these magnitudes are sufficient to elicit the motor response as delineated in Fig. 12, no FRET signal can be detected in sharp contrast to chemical stimulation.

37
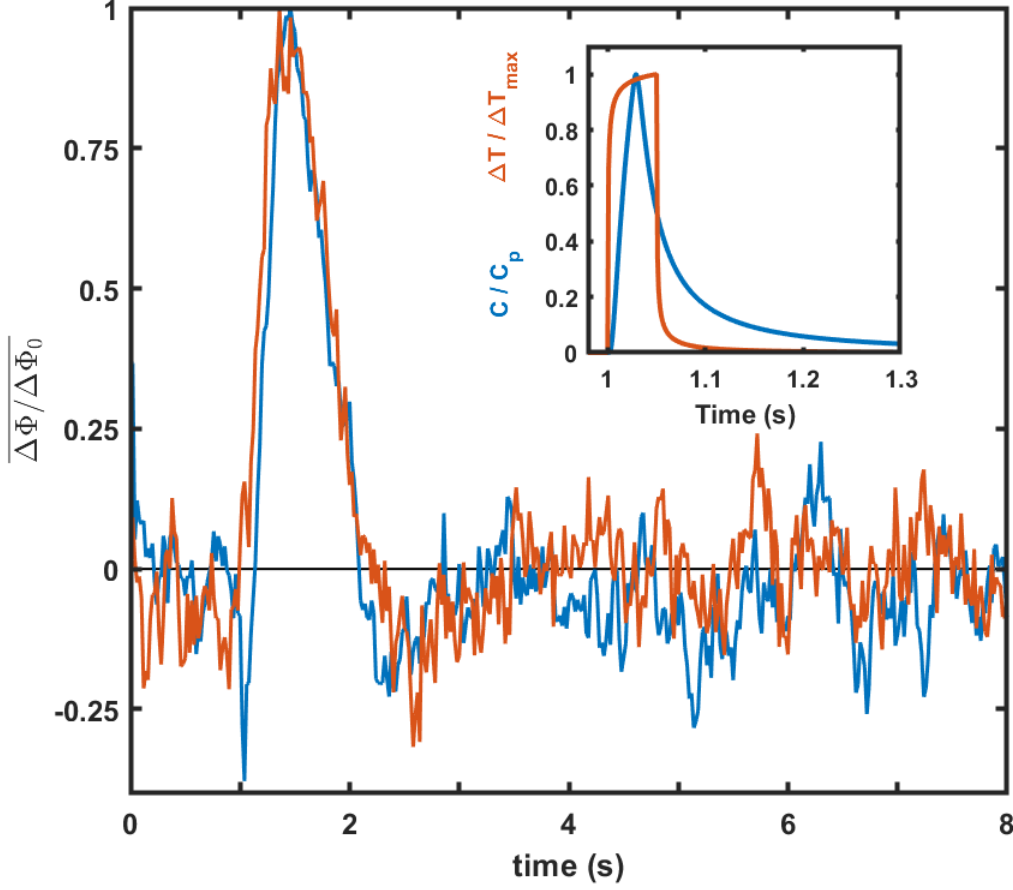
Figure 14: Behavioral Response Curves for Temperature and Serine Stimulation. The population-averaged response $\overline{\Delta\Phi/\Delta\Phi_0}$ for serine (blue) and heat (red) are displayed. Both curves are the results of averages of several stimulation levels, i.e., normalized CCW bias $\Delta\Phi/\Delta\Phi_0$ from individual stimulation levels were rescaled and then averaged. The average curves represent four serine measurements (793 pulses on 55 cells) and five temperature measurements (1640 pulses on 164 cells). The serine stimulation curve shows a sharp but brief decrease in the bias at $t = 1\,\mathrm{s}$ indicating that there was a small perturbation to cell rotation caused by a flow from the micropipette. The inset shows the temporal profiles of temperature (red) and serine (blue) stimuli experienced by a bacterium. Note the pulse width of $\sim 50\,\mathrm{ms}$ is significantly shorter than the bacterial response time ($\sim 1\,\mathrm{s}$) in the main figure and the stimulation can be qualified as impulsive.

4.0   THE THRESHOLD OF DETECTION OF AMINO ACIDS BY
Escherichia coli

The threshold of sensing has long been a topic of interest in biophysical studies. The most studied area has been the threshold of photon detection. The first measurement of the visual threshold in humans was performed by Langley in 1889 [67]. Numerous studies were made of the human visual thresholds during the 20th century, most notably by Hecht, Shlaer, and Pirenne, who discovered that a human can detect as few as 5 photons absorbed by the retina [68]. More recently, it was experiment discovered that humans can detect a single photon incident on the cornea of the eye [69]. Bacteria have also been found to be sensitive to single photons [70].

The limits of chemical detection by microorganisms has not received as much experimental attention, likely due to the relative experimental difficulty compared with light. Chemotaxis in *Escherichia coli* is one of the most studied topics in biophysics, however the lower threshold of chemical sensing is not well characterized. The earliest systematic study of the threshold of detection of amino acids by *E. coli* was carried out by Mesibov and Adler, in which bacteria accumulated in capillary tubes containing attractants [10]. This pioneering work showed which amino acids were attractive to *E. coli* and gave an order of magnitude estimate of the minimum concentration required to produce an accumulation: 60 nM for aspartate and 300 nM for serine. The resolution of this experiment was limited both because of the long duration (45 minutes) which gave bacteria time to metabolize the attractant, and the poor characterization of the concentration profile. Later studies only indirectly characterized the threshold for chemotactic detection in bacteria. Mao et. al. created a novel microfluidic device that again measured the accumulation of swimming cells [71]. The experiment found a behavioral response as low as 3.2 nM aspartate. Interestingly, despite finding a much lower threshold for aspartate, the measurement also found a higher limit for serine, at $\sim 1 \, \mu$M. Sourjik and Berg used the FRET system described in Ch. 3 to generate dose response curves of *E coli* to step stimuli [22]. The resolution of the experiment was enough to show a response to 300 nM aspartate. However, this should be considered

a conservative estimate since the measurement is made at the receptor level, and does not include the gain from the motors.

The issue of limits to sensitivity in chemotaxis has been address theoretically by Berg and Purcell [21], who treated the bacterium as a molecule counting device. The work found that diffusion places a fundamental limit on the signal to noise ratio of molecule counting. Their results have been extended to the relevant case of detectors built from cooperative molecules [72] and refined further by considering binding intervals at a single receptor [73]. It is still unclear, however, how Berg and Purcell's results may be applied to the case of zero background concentration.

Our interest in this chapter is on the sensing of chemoattractants by bacteria in a distinctive stimulation region satisfying two conditions: 1) small in magnitude and 2) of short duration. By limiting the measurement in this way we significantly eliminate the possibility of metabolism altering our results. In addition, because our measurement does not rely on the migration of bacteria, there is no possibility of cell to cell signaling interfering with the chemotaxis due to the attractant signal. Finally, for very short measurements the adaptation network does not have time to fully engage to reduce the sensitivity of the receptors. To our knowledge, this is the first study to examine the impulsive stimulation regime in a systematic and dose-dependent manner.

The main barrier to operating under these conditions is the experimental difficulty of producing precise pulses of chemoeffectors. Bacteria exist on the micron scale, where the main factor in chemical delivery is diffusion rather than mixing by fluid flow. In this diffusive regime, sharp gradients are quickly destroyed, making short time measurements difficult. One method to stimulate with very sharp steps is to use caged molecules [74, 75]. However, delivery of chemicals to a small region is important since large clouds of diffusible molecules are slow to disperse. Also caged molecules present additional experimental challenges, both in creating the molecule and constructing the optics. Another method is to use iontophoretic pipettes, such as in the study by Block, Segall, and Berg that discovered the biphasic response of *E. coli* [76]. This method presents problems in the low concentration regime since iontophoretic pipettes require a retaining current to prevent attractant leakage, which causes depletion near the open end of the pipette [77].

Here we present a new technique for creating short, well-defined, and reproducible pulses of chemoeffectors using a micron-scale valve. We then use this technique to quantify the chemotactic response of *E. coli* to small concentrations of amino acids by using the tethered cell assay. Finally, by using statistical methods, we find evidence that single cells respond to small numbers of individual ligand bindings.

4.1   THE CONSTRUCTION AND APPLICATION OF A MICRON-SCALE VALVE

We have chosen to use glass micro-electrode holders as a micropipette, as shown in Fig 15 A. Glass capillary tubes were heated and pulled to form a very narrow opening, typically 1 to 2 μm in diameter (see appendices A.2 for construction details). The micropipette is filled with an attractant solution and the tip is placed near a bacterium. To eject the contents of the pipette, we used short (25 ms), low pressure pulses (Fig 15 B).

In conducting preliminary experiments, we found it very difficult to reproduce results in the concentration region where the bacterial response is weak. We discovered that the open tip was a problem for quantitative measurements. Fig. 15 C shows that the fill height, h, is important at the microscopic level, and small variances in this parameter cause identical pressure pulses to release different doses of attractant. This is because the equilibrium fill height, h_o, depends on the depth of motility buffer (MB) in the observation chamber (Fig. 5), the osmotic pressure due to the concentration of the attractant, and the history of the pipette tip. All of these factors vary from day to day and we found that even under strict control for evaporation of MB during an experiment, the ejected attractant varies by as much as a factor of 3 over the course of a 2-hour measurement. More important is the variation due to the dilution of attractant solution at the tip: dilution is caused by the inflow of MB due to under-filling of the tip, which is necessary to prevent attractant leakage. The average number of attractant molecules ejected depends directly on the extent of the depletion, and thus also on the amount of time elapsed since the previous pulse.

Our solution was to block the tip with a check-valve to eliminate flows in the absence

of applied pressure. As shown in Fig 15 D, we use a $2\,\mu$m diameter polystyrene micro-sphere (bead) to temporarily block the tip. By under-filling the tip, $h \sim h_o/2$, the bead is held in place by the pressure difference between the interior of the tip and the external bath. Because of a low-Reynolds number[1], fluid flow is reversible for velocities, $u < \nu/L \sim 10^5(\mu\text{m}^2/s)/2\mu\text{m}= 5 \times 10^4\,\mu m/$s. Thus, when a short pressure pulse is applied, the bead is pushed out a distance before returning with the inflow to re-seal the tip, as shown in Fig 16. The result is a system that delivers reproducible pulses that may be easily calibrated by adjusting the applied pressure. The results of 30 pulses, with inter-pulse durations ranging from 5 to 30 seconds, are shown in Fig 19 A. The pulse height was found to vary with a standard deviation of 7%, and importantly, it does not depend on the time since the prior pulse so long as the valve has been closed for ~ 1 s. In addition, the method is simple to implement: a few micro-liters of micro-sphere solution was added to the sample before observation, and beads would migrate to the glass surface over time, making them easy to locate and use to block the tip. The loss rate for beads was roughly 1/100, in other words 100 pulses could be delivered on average before the bead was lost and would need to be replaced.

This system worked well for stimulating bacteria using our self-trapping assay, and yielded the chemical stimulation results presented in chapter 3. However the bead often became lost when stimulating cells in the classical tethering assay. This is because flagellar fragments in the MB would build up on the sphere, eventually causing it to stick to the glass surface, or eject at a large angles and not return. Additionally, microspheres that were not perfectly spherical were lost at a higher rate.

In light of these problems, we modified our method by adding a hinge to the bead. A small amount of poly-lysine was added to the end of the micropipette tip after filling with attractant solution. The poly-lysine then acted as a hinge, preventing the bead from being lost, and greatly reducing the "dead time" of the valve (see appendix A.2.2 for details on how to create the hinge). An example of this method is shown in Fig. 17. The performance of

---

[1]The Reynolds number is a measure of the relative strengths of inertial forces to viscous forces in a fluid: Re$= \frac{uL}{\nu}$, where u is the velocity of the fluid, L is a characteristic length, and ν is the kinematic viscosity. A Reynolds number less than unity indicates that viscous forces are larger than inertial forces. For swimming bacteria, Re$\sim 10^{-4}$.

the hinged valve was the same as before, and degradation of the poly-lysine was not observed under normal experimental conditions in which a hinge was typically subjected to 200-300 pulses.

4.1.1 Calibration and Numerical Fitting of the Concentration Profile

In order to calibrate the attractant concentration in the stimulation, an excitation laser was focused into a diffraction limited point at the location of measurement, marked with a red "x" in Fig.18. The laser would excite fluorescein that was added to the attractant solution, and the emitted light would be collected by a single-photon counting module (SPCM), as shown in the appendix (Fig. 30 A). As Fig. 18 shows, the distance from the mouth of the tip to the laser spot is $r \sim 9\,\mu$m. Despite the velocity of the outflow, it was found that a point source approximation for the concentration at the location of the cell works quite well. Let the origin be placed on the glass surface directly under the tip and let x be the distance from the origin to the calibration spot, then

$$C(x,t) = A \int_0^t \frac{2\,e^{-\frac{x^2+a^2}{4D(t-t')}}}{(4\pi D(t-t'))^{3/2}}\,H(\Delta t - t')dt'$$

(4.1)

$$= \begin{cases} \frac{A}{2\pi D\sqrt{a^2+x^2}}\left(1 - \mathrm{erf}\left(\sqrt{\frac{a^2+x^2}{4Dt}}\right)\right) & \text{for } t \leq \Delta t \\ \frac{A}{2\pi D\sqrt{a^2+x^2}}\left(\mathrm{erf}\left(\sqrt{\frac{a^2+x^2}{4D(t-\Delta t)}}\right) - \mathrm{erf}\left(\sqrt{\frac{a^2+x^2}{4Dt}}\right)\right) & \text{for } \Delta t < t \end{cases}$$

where $H(t)$ is the Heaviside function, D is the diffusion coefficient of the dye or chemoattractant, a is the vertical distance from the surface to the source, $\mathrm{erf}(x)$ is the error function, Δt is the duration of the pressure pulse, and A is a scale parameter that has dimension of number per time. The factor of 2 in the integral expression is due to the image source required by the reflecting boundary condition at the glass surface. We found Eq. 4.1 to be a good approximation of the concentration of fluorescein ($D_f \sim 600\,\mu$m^2/s [78]), as delineated by the green line in Fig 19 A. The calculation using D_s, the diffusion coefficient for serine,

shows that the half-height full-width of the serine pulse at the cell is ~ 60 ms. Our calibrations also showed that the peak concentration at the rotation axis of the cell was $\sim 8\%$ of the concentration in the micropipette, C_0 (see appendix A.2.3).

The above calculation indicates that the peak concentration experienced by the cell, C_p, strongly varies with distance from the source, however this variation did not effect our measurement. This may be explained by the fact that the rotation of the bacteria averages the concentration experienced by the cell. At 10 Hz, a typical rotation rate for this experiment, a cell will rotate through an angle of 180° during the half-height width of the attractant curve in Fig. 19 A. For the analysis of this issue using the collected data/, see appendix A.2.4.

Finally, we were able to estimate the volume ejected, V, by a single pulse from our pipette using strobe lighting. We found that a tip of diameter $2d = 1.5$ μm ejected fluid at $v \sim 400$ $\mu m/s$. Thus the total volume ejected is

$$V = v\pi d^2 \Delta t \approx 18 \ \mu m^3 = 18 \ \text{fl} \ . \tag{4.2}$$

Further details of this estimation, along with an example of the images obtained from the high speed strobe lighting are provided in appendix A.2.3.

4.2   RESULTS

Using the new method explained above, we impulsively stimulated tethered wild-type strain RP437 using a range of concentrations of either serine or aspartate. Single cells were recorded for multiple trials, each lasting 10 s, during which a single pulse of chemoattractant was administered at $t = 1s$. Recordings of cell-body rotation were converted to binary rotation states as a function of time using Eq. 2.3 as described in Fig. 19 B, then averaged over many cells to yield a population average measurement for each concentration. The examples of stimulation using different concentrations in Fig. 19 B show a clear decline of the response of the CCW bias, $\Phi(t)$, to decreasing serine concentrations. To quantify the threshold, we conducted extensive measurements in the region $3 \leq C_p \leq 2300$ nM serine,

44

as shown in the inset of Fig. 20 and in Appendix Fig. 39. For each concentration, between 10 and 15 bacteria were used, with each contributing at least 10, but typically 20 trials.

In order to compare the bias curves of varying background bias, Φ_0, we subtract the background and re-scale the data to obtain the normalized bias:

$$\frac{\Delta\Phi}{\Delta\Phi_0} \equiv \frac{\Phi(t) - \Phi_0}{1 - \Phi_0} \ . \tag{4.3}$$

This quantity is preferable to the bias itself because it ranges from 0 to 1 for attractant stimulation. The maximum value of this quantity, plotted in the inset of Fig. 20, serves as measure of the response to a given attractant concentration. We found that the behavior of the cells saturated for serine concentrations $C_p > 100$ nM and aspartate concentrations $C_p > 1.6\,\mu$M. Interestingly, the curves that show a response, but are not saturated, were found to collapse when scaled by their maximum value. The result of averaging over all of the measurements scaled in this way yields the "impulse response" plotted in Fig. 20. The threshold of detection was found by using the method previously used by Adler [10]: plot the response against concentration on a log-log plot, and extrapolate to the "noise floor" set by our measurement. The log-log plots are shown in the methods (Fig. 39), and give a value of $C^* = 7$ nM for serine and $C^* = 15$ nM for aspartate.

The absolute threshold concentrations of detection C^* are likely dependent on the growth condition, since these conditions affect the ratio of chemoreceptor types [79, 80, 81] and total receptor number [15] in *E. coli*. This may explain the discrepancy among past measurements of the thresholds. The threshold concentrations found here are remarkably low, corresponding to ~ 8 and ~ 17 molecules of serine and aspartate, respectively, per typical cell volume. This fact motivated an investigation into whether the threshold could be quantified in terms of numbers of individual molecular bindings rather than a concentration.

4.3 SMALL NUMBERS OF BOUND RECEPTORS ELICIT A DETECTABLE RESPONSE

Based on the threshold found above, we should not expect the response of an individual cell to low concentrations to be deterministic; rather the response is subject to large fluctuations. First we will make an estimate of the average number of attractant molecules that reach the receptors of a bacterium in our experiment. Then we present a statistical method to determine the threshold number of molecules to cause a behavioral change. Finally we apply this method to our experimental data.

4.3.1 An Estimate of the Number of Molecules That Reach the Receptors

Here we use arguments from Berg and Purcell [21]. Because of the low Péclet number, we will ignore the velocity of the fluid in our estimates.

For simplicity, assume that we have a spherical cell of radius a that is a distance r from the pipette tip. The probability, P_a, that a molecule released from the tip reaches the surface of the cell is

$$P_a = \frac{a}{r}$$

[21]. This exact result is independent of the diffusivity of the attractant molecules and is true even in the presence of the glass boundary present in our setup. Now a molecule that has reached the surface of the cell will necessarily bounce around in the neighborhood of the surface before escaping to infinity. If we assume that the cell has a single receptor patch of radius s ($s \ll a$), the probability, P_s, that the molecule near the surface hits the receptor patch at least once before disappearing is

$$P_s \approx \frac{s}{s + 4a}$$

[21]. Therefore the probability of a molecule that is released from the pipette tip hits the receptor patch at least once is

$$P = P_a P_s \approx \frac{as}{r(s + 4a)} \ . \tag{4.4}$$

In our experiment, $r \approx 9.4$ μm, $a \approx 1$ μm, and $s \approx 0.1$ μm [18], giving a value of $P \approx 2.6 \times 10^{-3}$. In other words, just under 3 of every 1000 molecules released from the pipette hit the receptor patch at least once. We assume this is an upper bound for two reasons: the first is the fact that passive diffusion through the outer membrane can only reduce the number of molecules reaching a receptor, and the above result neglected the possibility of the molecule being absorbed by the cell. Given that the tip is filled with concentration C_0, and the volume ejected from a pulse is V, Eq 4.2, this estimate yields the average number of molecules that reach the receptor patch per pulse: $\overline{N} = C_0 V P$. This estimate for the concentrations used in this experiment is summarized in Fig. 21. We find that at the maximum response $\Delta\Phi/\Delta\Phi_0 = 1$, $C_0 = 1\,250$ nM serine, which corresponds to only $\overline{N} \sim 35$ molecules on average reaching the receptor array. In addition, the threshold of serine detection corresponds to ~ 2.5 serine molecules reaching the receptor array. We assert that this implies that the reduction in amplitude of $\Delta\Phi_{max}/\Delta\Phi_0$ for decreasing attractant concentration is due to a decreasing fraction of responses, rather than decrease in the individual response for a cell.

4.3.2 Determination of the Threshold Values

To quantify our measurement, we employ a statistical method first used to investigate the threshold of human vision by Hecht et. al. [68], and later to discover that photo-tactic halobacteria are capable of single photon detection [70]. We first present this method, then the results of this analysis applied to our data are presented and discussed.

Suppose there exists a threshold number of bindings, n^*, that trigger a response. In this context, a "response" means a detectable change in behavior defined in detail below. For any given attractant concentration, C_0, there will be an average number of bindings per pulse, $\alpha\overline{N}$, that occur over many trials. We expect that the actual number bound for any single trial to obey a Poisson distribution. Given these assumptions, the probability that the cell responds to a pulse is the probability that at least n^* molecules have bound and is given by

$$\hat{P} = \sum_{n=n^*}^{\infty} \frac{(\alpha\overline{N})^n e^{-\alpha\overline{N}}}{n!} = 1 - \sum_{n=0}^{n^*-1} \frac{(\alpha\overline{N})^n e^{-\alpha\overline{N}}}{n!} \ . \tag{4.5}$$

This probability is plotted for $n^* = 1, ..., 5$ in the inset of Fig. 21. When plotted on a log-linear plot, the slope at $\hat{P} = 0.5$ monotonically increases with n^*. Also note that $\alpha\overline{N}$

is proportional to C_0, i.e., $\alpha \overline{N} = \alpha P_r V C_0$, where α is an "efficiency factor" related to the number and type of receptors and the chemical kinetics of binding. Therefore if the experimentally determined probability of response is plotted against $\log(C_0)$, the threshold, n^*, is found by matching the slope to one of the curves in Fig. 21, and α is determined by a shift of the curve in the horizontal direction.

To calculate $\hat{P}$, trials were scored either positive or negative for a response. A trial was marked positive if the time average of the rotation state over a window immediately after the pulse was greater than Φ_0, and negative otherwise. The center of the averaging window is $t = 0.46$ s after the pulse, which is the time of the peak of the bias curves in Fig. 20. The duration of the window is adjusted for each cell to have a length based on the autocorrelation time of the rotation trace. This adjustment was performed because the background switching rate for cells varies significantly. Details about how this window was calculated are left to appendix B.1.

There is a significant probability of the algorithm marking a false positive, however the rate of false positive response can be estimated. In the absence of stimulation the probability that the mean over the window is greater than Φ_0 is roughly equal to the probability that the center frame is 1, which is just Φ_0 by definition (see appendix B.1 for further details). For a sufficient number of trials, N_t, the number of positive trials, m, should approach the expected number:

$$m \approx N_t \left((1 - \hat{P})\Phi_0 + \hat{P} \right)$$
$$\text{or } \hat{P} \approx \frac{\frac{m}{N_t} - \Phi_0}{1 - \Phi_0} \tag{4.6}$$

This quantity is plotted in Fig. 21 for both amino acids tested. Interestingly, although the threshold concentration is higher for aspartate, the best fit for this attractant is $n^* = 1$, which should be compared to 2 bindings required for serine.

4.4 DISCUSSION

Receptors couple together in an extended Ising-like array, which increases the gain of chemotractic signals [17, 18, 13]. However the details of the array are not clear. One model of the array groups receptors together in fixed-size clusters which function as independent MWC macro-molecules [23]. This model is attractive because, although simple, it qualitatively explains a number of observed chemotactic behaviors. Another model allows the size of the MWC clusters to vary [24], incorporating the experimental observation that cooperativity among receptors increases with methylation [55]. An attractive feature of the adjustable cluster size model is that methylation is receptor specific, i.e., a cell adapted to aspartate retains sensitivity to serine, which agrees with experiment [82]. In both models, the essential features of the array remain: the coupling between receptors provides gain to the system, and methylation allows a cell to adapts to background concentrations.

The principle observation of our measurement is that many, in fact most, attractant molecules that reach the receptor cluster elicit no behavior response. The factor α in Eq. 4.5 determines the "efficiency" of a chemoattractant molecule in our experiment, and is bounded between 0 and 1. An efficiency factor of 1 indicates that every molecule that at the receptor array binds, and causes a detectable behavioral change. We find $\alpha \approx 0.11$ for serine and $\alpha \approx 0.015$ for aspartate. In other words, only $\sim 11\%$ of serine molecules, and $\sim 1.5\%$ of aspartate molecules that reach the receptors cause the cell behavior to change. This inefficiency can arise from several sources: the number of receptors, the binding affinity of the receptors to the ligands, and the activity of the receptors.

The total area of the receptor cluster used in Eq. 4.4 is only partially covered by binding sites for the specific amino acid used. Aspartate sensing Tar and serine sensing Tsr are the most abundant receptors, making up $\sim 90\%$ of the total. It is not immediately clear what the "effective area" of a specific ligand binding site is. Under the assumption that the effective binding area is smaller than the total size of the receptor patch, it is not likely that the number ratio of Tsr to Tar receptors can explain the discrepancy between the efficiency of the two attractants. This is because previous immunoblotting measurements showed that the numbers are roughly equal [15] or even that Tar can outnumber Tsr by a factor of 3 in

our growth conditions [80]. The activity of the receptors would further affect the effective area, since the binding affinity of a ligand to the inactive conformation of a receptor is much less in the MWC model. Furthermore, ligand binding to an inactive receptor causes little change in the phosphorylation activity of the cell.

The most likely explanation of the differing efficiency is the different sensitivities between the two receptors. The question of how the receptor methylation state alters the sensitivity is still an open one: a 2000 study suggests that methylation directly reduces the binding affinity of the receptor to the ligand [83]. This disagrees, however, with previous experiments that found that the binding affinity is unaffected, indicating that the sensitivity reduction is decoupled from the binding energy [84]. Our experiment is not able to determine, nor are our conclusions affected by, how the methylation decreases the sensitivity, so we assume reduced affinity. Our data and analysis shows that Tar is less sensitive to aspartate, than Tsr is to serine by at least a factor of 7, which assumes the same effective area for both receptors. However, Tar receptors effect the behavior more strongly, requiring only one binding to alter the probability. Thus the gain of the receptor array is greater for asparate signals than it is for serine signals. This can happen if Tar receptors are more strongly coupled with nearest neighboring receptors than are Tsr. In other words, our data shows that under our experimental conditions the average correlation length of receptor conformation in the array is greater for Tar than it is for Tsr, or more precisely, the average correlation length for Tar is roughly twice that of Tsr.

The data presented in [55] shows that the correlation length for Tar is roughly 6 receptors for cells unadapted to attractants. Their measurement, however, was performed on cells expressing only Tar rather than the mixed receptor clusters of the wild type cells as in our experiment. If the strains are comparable, our data implies that the correlation length for Tsr is only 3 on average. If so, then the connectivity of the receptor array must be very heterogeneous, and there are a small number of extensively connected "hot spots" that are sensitive to serine in our experiment. If this were not the case, then only inactivating two would not produce a significant change in the CheYp concentration of the cell. Alternatively, the average correlation length in our cells may be much larger than that seen in the experiment in ref [55].

Reducing the methylation of Tar receptors, perhaps by lowering the ambient temperature or introducing a repellent chemical to the medium would be a test as to weather n^* could be changed. Receptor modified by genetic engineering would not work for this purpose since experiments reveal that even the least "methylated" engineered receptors have a lower sensitivity to attractants than do the wild type [22]. This experiment could reduce C^*, but potential would simultaneously increase n^*, reflecting a sensitivity-accuracy trade off. Namely, as sensitivity to chemoeffector molecules increases, the gain may decrease to fight against noise.
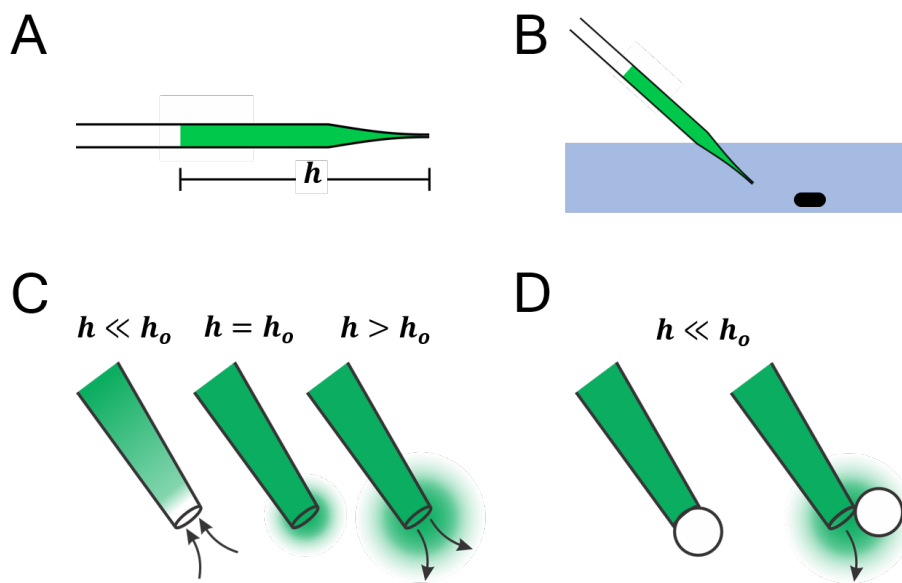
Figure 15: Problems and Solutions for Using a Micropipette. A) A micropipette is filled to a height h with attractant solution. B) The tip is submerged near a bacteria to deliver the attractant, and the other end is connected to a pneumatic line. C) There exists an equilibrium height, h_o, such that there is no volume flux at the mouth of the tip. If $h \ll h_o$ then the flow into the tip will be great enough to create a region of dilution near the mouth. If $h > h_o$, there will be an outward flux creating a chemical gradient in the region surrounding the tip. There is a diffusive flux out of the tip even if $h = h_o$. D) The solution is to create a check-valve at the end of the tip. When no pressure is applied to the pipette, under-filling will cause a microsphere to block the tip. When a positive pressure is applied, the bead is pushed out of the way. Once the pressure returns to normal, the inflow will pull the sphere back in place, resetting the system for the next pulse.
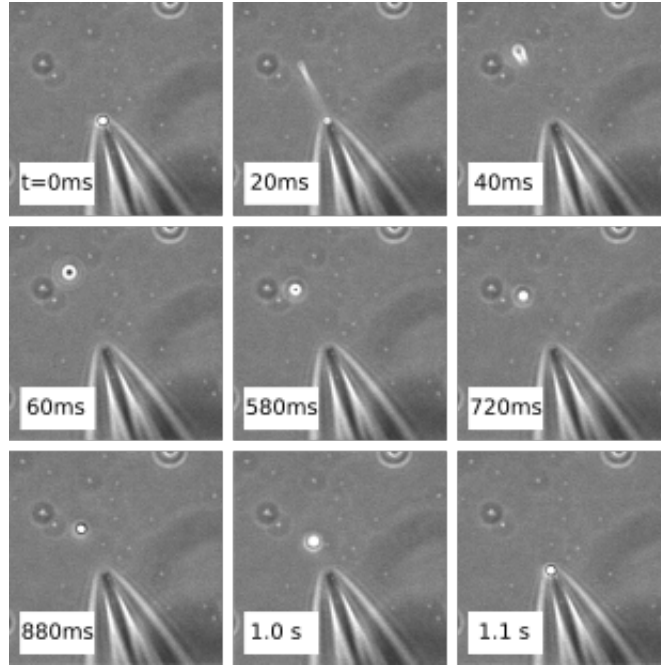
Figure 16: Image Sequence of a Microsphere Used as a Check-Valve. Initially a bead is blocking the opening of the micropipette. A 25ms pressure pulse causes a rapid ejection, followed by a slow return of the bead to the tip. Note that the time between frames is not uniform.
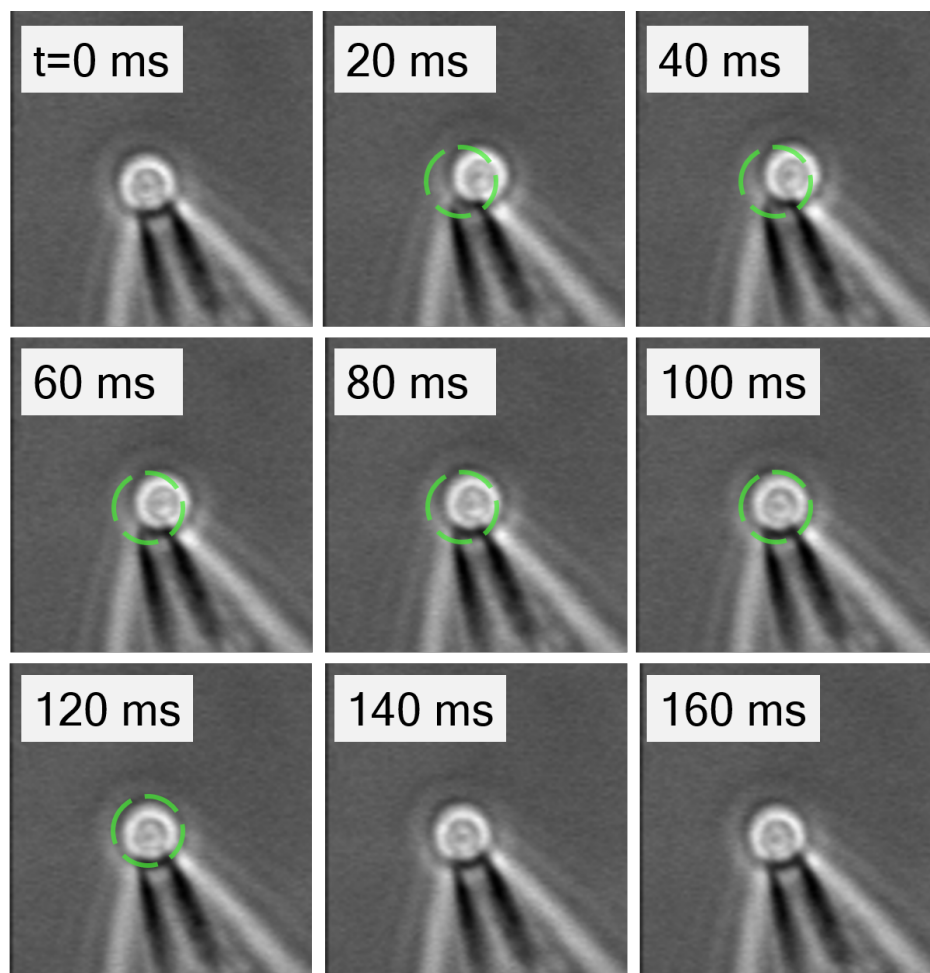
Figure 17: Image Sequence of a Hinged Check-Valve. Initially a bead is blocking the opening of the micropipette. An unseen poly-lysine linker binds the right side of the bead to the glass tip. A 25 ms pressure pulse pushes the bead out of the way before the following inflow pulls the bead back into place. Green dashed lines are shown in some images to indicate the initial position of the bead. The actuation of a hinged valve is much more rapid than the unhinged version.
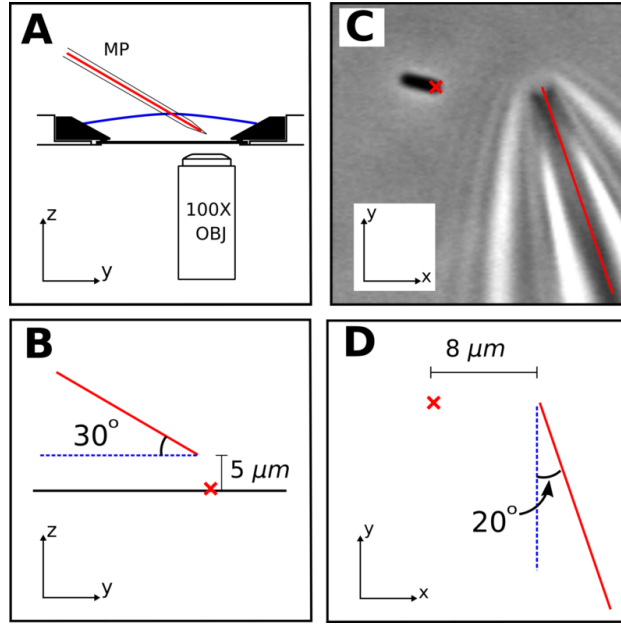
Figure 18: The Geometry of Our Measurements. The red line denotes the axis of the micropipette tip in all panes. A) A side-view of the micropipette tip (MP) in position in the observation chamber. B) A zoomed-in version of A. The red "x" denotes the location of a rotating bacterium and laser spot for calibration. C) A micrograph showing a rotating bacterium in a measurement. The red "x" denotes the rotation axis. D) A schematic version of panel C.
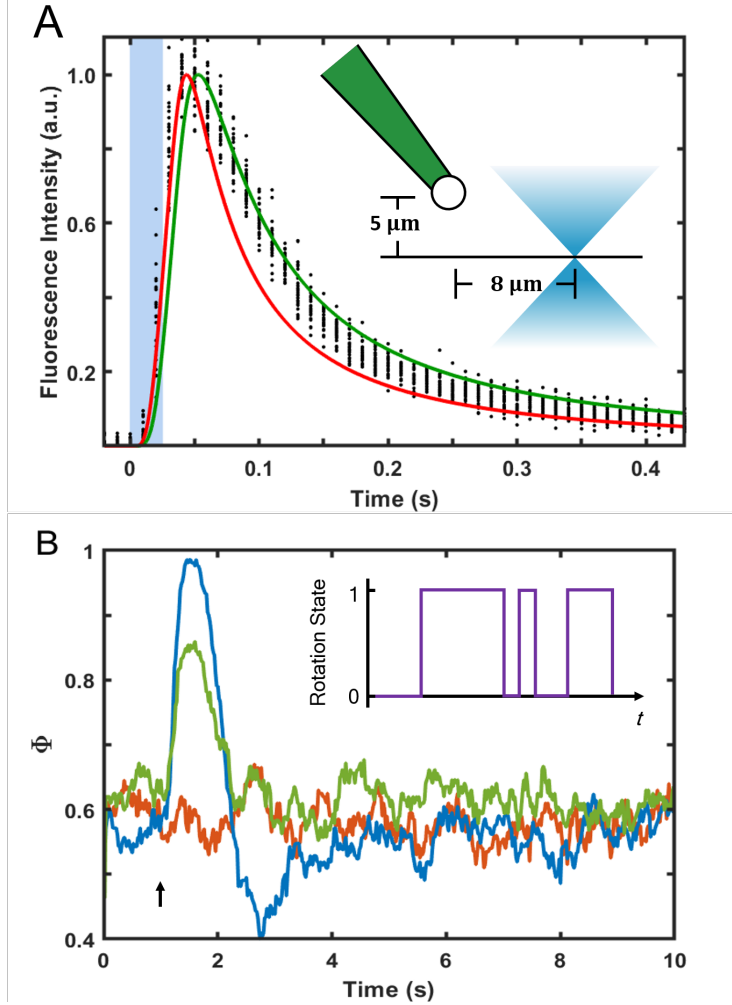
Figure 19: Temporal Profile of Chemo-attractant Pulses and Bacterial Population Average Responses. A) Scatter plots of 30 pulses are displayed as solid dots. The data was taken by exciting fluorescein in the attractant solution using a diffraction limited laser spot, as shown in the inset. The green line shows that the profile can be fit adequately by assuming the attractant solution is released from a point source at a constant rate during the interval, $25 < t < 50$ ms, which is shows as a shaded region. The temporal profile for serine $(D_s = 900 \ \mu^2/s$, red line) is narrower than that of fluorescein $(D_f = 600 \ \mu^2/s)$, and has a full duration at half maximum of 60 ms, compared to 100 ms. B) The population-averaged counter-clock-wise bias $\Phi(t)$ of $E.\ coli$ to pulses of different serine concentrations, $C_p = 12$ nM (red), 40 nM (green), and 96 nM (blue). The pulse, indicated by the arrow, is delivered at $t = 1$ s. The inset shows an example of the binary rotation state trace for a single cell in which CCW (CW) motor rotation was assigned 1 (0).
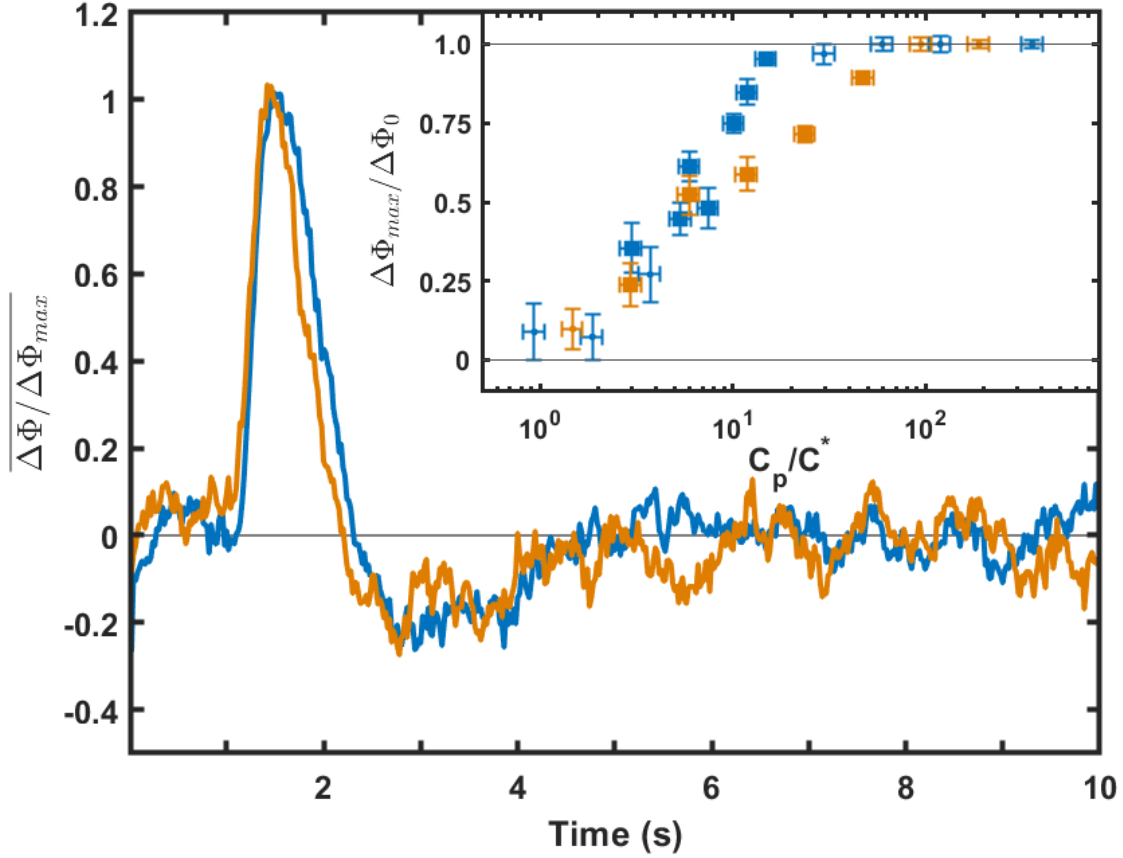
Figure 20: The Response of *E coli* to Amino Acids. The main figure shows the average scaled bias for 1362 pulses of serine (blue) or 958 pulses of aspartate (orange) administered at $t = 1$ s. These curves were created by averaging collapsible bias data from different concentrations as explained in the text. The inset shows the peak response, $\Delta\Phi_{max}/\Delta\Phi_0$, for each concentration used, with colors denoting the same information as the main figure. The measurements that were used to create the main figure are plotted as solid squares, and measurements that could not be collapsed have only error bars and no symbol. Vertical error bars denote the error in calculating the response from the data collected, the horizontal error is the uncertainty in the peak concentration experienced by the cell.
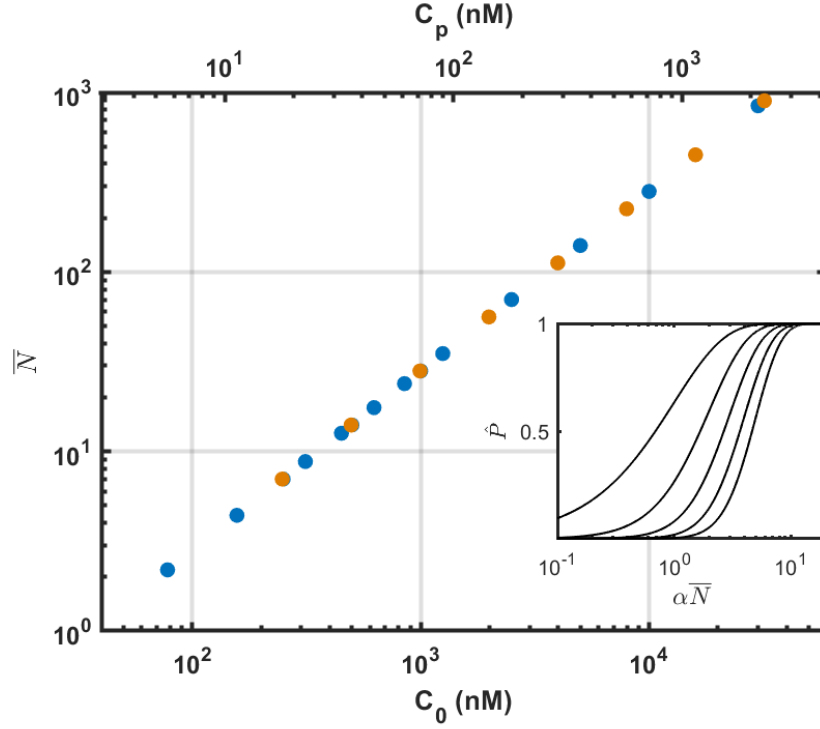
Figure 21: A Summary of Our Measurements. The main figure shows a dot at each pipette concentration, C_0, tested in this experiment. Blue dots denote serine and orange dots denote aspartate. The top axis shows the peak concentration experienced by the cell: $C_p = C_0/14$ as explained in Sec. 4.1.1. The vertical axis shows the estimated average number of molecules, $\overline{N}$, that hit the receptor patch (see Eqs. 4.2 and 4.4). The inset shows the probability of detection, Eq. 4.5. The lines are for $n^* = 1, 2, ..., 5$, in order of increasing slope at the inflection point.
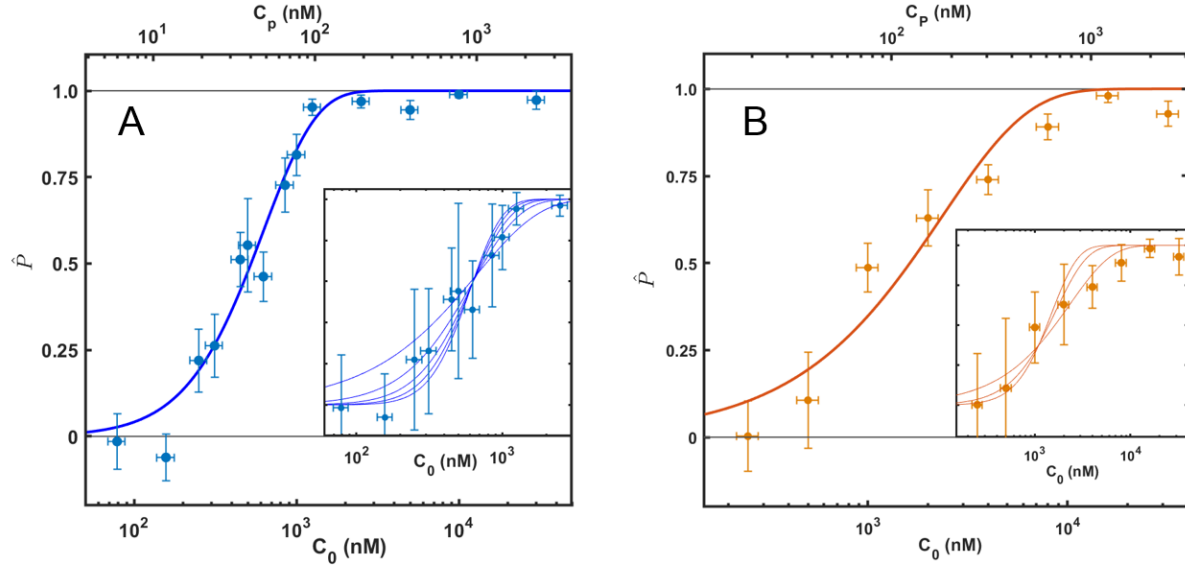
Figure 22: Threshold of Amino Acid Detection in *E coli*. Figure A is for serine stimulation and figure B is for aspartate stimulation. The probability of response is plotted against the concentration in the micropipette C_o (the bottom axis) and the concentration experienced by the cell $C_p = C_o/14$ (the top axis). Vertical error bars are the standard deviation of the mean of the population and horizontal error bars are the uncertainty in C_p. The best fit lines with $n^* = 2$ for serine, and $n^* = 1$ for aspartate are plotted in the main figures. The horizontal solid lines are drawn at $\hat{p} = 0$ and 1 as an aid to the eye. Inset: The same data as in the main figure with error bars instead showing the standard deviation of the population. This data is included to show that although the population mean response probability has relatively small error, the population has a large variance, i.e., the population is very heterogeneous. The lines shown, in order of increasing slope, are for $m = 1, 2, 3, 4,$ and 5 for serine, and $m = 1, 2,$ and 3 for aspartate. The main conclusion from these results in that single cells respond to a small number of discrete bindings.

5.0   A COMPARISON WITH AN EXISTING MODEL

The large amount of well-controlled data collected in the previous chapter allows a comparison with a frequently referenced model of the chemotactic network [23]. This model, proposed by Tu, Shimizu and Berg (TSB), predicts the change in CheY-P concentration, $\Delta Y(t)$, given a time-varying attractant ligand concentration, $C(t)$. The model assumes a uniform concentration of CheY-p in the cell, however this is at odds with the fact that the source and sink of CheY-p are localized at the cell poles. Any change in CheY-p concentration produced must diffuse through the cytoplasm before it can effect the motors. Here we take the approach that the receptor array obeys the TSB model and accordingly generates predictable changes in the CheY-p concentration at the cell pole. This "signal" will then propagate through the cell before eliciting a change in bias at the motors.

In this chapter, we will first estimate $\Delta Y(t)$ from our data, then present the model along with a modification inspired by this work, and finally discuss the effect of diffusion on the signal.

5.1   INDUCED AND SPONTANEOUS CHEY-P CONCENTRATION FLUCTUATIONS

The changes in CCW bias, $\Phi(t)$, induced by chemoattractant stimulation displayed in Figs. 23 (A, B) are distinctively different from spontaneous fluctuations of the motor bias. This is delineated in the inset of Fig 23 A where many spontaneous CCW rotation intervals are collected, aligned by their starting point, and averaged. In this case, we found that the decay of this average is faster than exponential, and importantly the width of the decay is much shorter than measured in the stimulated case.

In order to gain information about signal transmission inside a bacterium, we used the bacterial motor response function to convert $\Phi(t)$ to CheY-p concentration fluctuations at the motor site. Previous studies showed that the flagellar motor switch is strongly allosteric,

displaying a sigmoidal response to CheY-p binding with a large Hill coefficient, $h \simeq 10$ [28]. In appendix B.2 we show that the Hill function used in their study is equivalent to a hyperbolic tangent function,

$$\Phi = \Phi_0 + \Delta\Phi_0 \tanh\left[\frac{\Delta Y}{Y'}\right] \ ,$$

which is easier for us to invert. Here $\Delta Y = Y - Y_0$, Y_0 is the steady-state CheY-p concentration at the motor site, Φ_0 is the steady-state bias, $\Delta\Phi_0 = 1 - \Phi_0$, and $Y' \simeq 0.64\,\mu\mathrm{M}$. If this relationship holds for each instant of time, it follows that

$$\Delta Y(t) = Y' \tanh^{-1}\left[\frac{\Delta\Phi(t)}{\Delta\Phi_0}\right] \ . \tag{5.1}$$

This transformation is linear only when $\Delta\Phi(t) \ll \Delta\Phi_0$.

Figure 24 displays $\Delta Y(t)$ vs. t for stimulation using serine (A) and aspartate (B). For large amplitudes, the shape of the curves are quite different from those in Fig. 23; the truncation of the response peaks is a result of nonlinearity in Eq. 5.1. It is expected that the functional form of the response of a linear system to an impulsive stimulus should be independent of the strength of stimulation. In developing a theory for bacterial chemotaxis, linearity is often assumed for weak signals but its validity has not been solidly established. As with the bias curves in Fig. 20, we rescaled the amplitude of the response curves in Fig. 24 with the aim of collapsing the data on top of one another. We chose the response to $C_p = 66\,\mathrm{nM}$ and $C_p = 616\,\mathrm{nM}$ as our reference curves for serine and aspartate, respectively, and adjusted the amplitudes of individual curves until they aligned with the references. The result of this procedure is displayed in the insets of Fig. 24 (A, B), where we found that over about a decade of concentrations, $12 \leq C_p \leq 96\,\mathrm{nM}$ for serine and $19 \leq C_p \leq 616\,\mathrm{nM}$ for aspartate, the rescaled data are indeed collapsible. Thus within this range of concentrations the response of E. coli chemotaxis network can be characterized by a single mathematical form. For concentrations below this range, the responses are too small for us to reliably collapse the data, and for concentrations greater than this range, broadening and clipping of the response peaks are observed, indicating that the network response is no longer linear.

For a quantitative analysis of our measurements, we average all curves that fall within the linear-response range and plot them in Fig. 25 (A, B). As can be seen, the two chemicals

elicit responses that are very similar, i.e., when stimulated at $t = 1\,\text{s}$ with a short pulse, the relative CheY-p deviation decreases rapidly and remains below zero for much longer than the duration of the stimulation. The half-height-half-width of the negative response is about $\Delta_{1/2} \simeq 1\,\text{s}$ and is followed by a positive response that lasts for a few seconds. The similarity in the responses for both chemicals re-enforces the biophysical picture that the receptor complex is made of a mixture of different types of chemoreceptors, and they respond collectively to a stimulus.

5.2   A THEORETICAL MODEL of CHEMOTAXIS

The goal of the TSB model is to provide a relation between the external ligand concentration, $C(t)$, and the resulting change in the internal CheY-p concentration, $\Delta y(t)$, where lower case denotes the concentration at the receptor array. This model takes into account the cooperativity of chemoreceptors by grouping two trimers of homo-dimers (for a total of $N = 6$ binding sites) to form an effective functional unit with precise adaptation. For simplicity, we assumed that such a functional unit is composed of either Tsr or Tar. Each unit can either be in an active state or an inactive state with the time average given by the "activity" $a(t)$. A unit that is in the active state will phosphorylate CheY to form CheY-p, while an inactive state does not. CheZ is assumed to be constitutively active. Finally the model assumes that the concentration of CheY-p is homogenous, and does not take into account the spacial organization of the cell beyond the idea that there are many groups of N receptors.

A derivation of the model is given in the appendix B.3 with the principle result that $\Delta y(t)$ is given by

$$\Delta y(t) = \int_0^t G_Y\left(t - t'\right) f_L\left(C(t')\right) dt'. \tag{5.2}$$

where $f_L(C(t))$ is the free energy change of the receptors at a concentration $C(t)$, and $G_Y(t)$ is the impulse response:

$$G_Y(t) = k_a N a_0 (1 - a_0) \frac{t_z t_m}{t_m - t_z} \left(\frac{1}{t_m} e^{-\frac{t}{t_m}} - \frac{1}{t_z} e^{-\frac{t}{t_z}} \right). \tag{5.3}$$

Here t_z and t_m are the dephosphorylation and methylation timescales, respectively, k_a is the phosphorylation rate, and a_0 is the average steady state activity of the receptors. The free energy change, f_L, is given by the MWC model as

$$f_L = \ln \left[\frac{1 + C/k_I}{1 + C/k_A} \right] \ , \tag{5.4}$$

where k_I and k_A are the dissociation constants of the inactive and active form of the receptors, respectively.

The amplitude of the CheY-p decrease is proportional to the free energy change during the impulse, which is the only factor that differs between the various stimulation strengths used in our experiment. This amplitude is plotted in the insets of Fig. 25 A for serine and B for aspartate. The red lines are fits with Eq. 5.4 and yield values for k_I and k_A that are considerably lower than values in the literature: $k_I = 300$ nM and $k_A = 8$ μM for aspartate and $k_I = 70$ nM and $k_A = 500$ nM for serine. A 2002 work by Sourjik and Berg found that for aspartate $k_I \sim 5$ μM and $k_A \sim 100$ μM using FRET [22]. The reason for the discrepancy between our measurement and their work may be attributable to the fact that our measurement is at a behavioral level, rather than relying on the interaction between CheY and CheZ. Our work in chapter 3 sheds doubt on the interpretation that the FRET signal in their experiment is proportional to the concentration of CheY-p alone. In addition, their measurement used long step stimuli, which allows the methylation network to act. A later study by Kalinin et. al. using migration of wild-type cells found similar values for aspartate of $k_I \sim 18$ μM and $k_A \sim 3$ mM, and also they measured $k_I \sim 6$ μM and $k_A \sim 30$ μM for serine. The reason for this discrepancy is not immediately clear, but may also be due to the fact that the exposure of bacteria to stimuli is much longer.

Although this model fits the amplitude of the CheY-p waveform as a function of stimulation strength C_p, the temporal profile does not agree with our measurement. Given that the width of the stimulation in Fig. 19 is much shorter than the timescales, t_m and t_z, of the model, the calculated temporal concentration profile, $\Delta Y(t)$, should not be sensitive to the shape of the input. Therefore we simply use a square pulse with a width of 60 ms for the input concentration. The output of Eq. 5.2 using this input is shown as green lines in the insets of Fig. 26. The model captures the essential aspects of the *E. coli* response to a

brief stimulation: the CheY-p concentration decays rapidly and recovers within ~ 1 s and overshoots before a slow relaxation back to pre-stimulation level. The next section discuses the effect diffusion has on the temporal profile.

5.3 DIFFUSIVE SIGNAL PROPAGATION INSIDE THE CELL

The curves in the insets of Fig. 26 capture the qualitative features of the data in Fig. 25, but quantitatively there are some differences. First, there is a delay of 250 ms from the time of the stimulation to the response of the bacteria that is not explained by Eq. 5.2 and second, the predicted decrease in CheY-p is much sharper than our measured data. Both of these discrepancies point to diffusion of the CheY-p concentration through the cell. To model this process, we assume that the receptors form a complex at a cell pole, which is indicated by many studies [85, 19, 17, 18]. It is also known that CheY-p spontaneously decays to CheY at a rate of ~ 0.1 s^{-1} [86]. We assume the problem to be 1-dimensional, thus the appropriate diffusion equation for the CheY-p concentration is

$$\frac{\partial Y(x,t)}{\partial t} = D\frac{\partial^2 Y(x,t)}{\partial x^2} - \lambda Y(x,t) \tag{5.5}$$
$$Y(0,t) = y_0 + \Delta y(t)$$
$$\left.\frac{\partial P}{\partial x}\right|_{x=L} = 0$$
$$Y(x,0) = Y_0(x)$$

where $D = 7$ μ^2/s is the diffusion coefficient of CheY-P in the cytoplasm, $L = 3$ μM is the length of the cell, and $Y_0(x)$ is the steady state profile of CheY-p over the length of the bacterium. The concentration at $x = 0$ is specified by the constant y_0 that fixes the steady state concentration plus the time dependent term $\Delta y(t)$ which is the result of Eq. 5.2. The steady state concentration is constrained by requiring that the average CheY-p concentration is 3 μM [28]. The details of the solution are given in appendix B.5 with the result plotted in Fig. 26. As can be seen, the combination of the TSB model with the diffusion equation

yields a good fit to the negative portion of the response and is shown as the green curves in Fig. 26. The overshoot of the response, however, is consistently too small to be fit with the model. This overshoot is the result of the Green's function, Eq. 5.3, having equal area above and below the curve.

Our previous work using a FRET measurement in chapter 3 suggests a modification to the TSB model to incorporate the idea that CheZ is not passive but actively regulated by the receptors. The results of that experiment imply that CheZ is made briefly more effective by ligand binding. As an approximation, we add an additional term to the model that further decreases the activity while ligand is bound, as detailed in appendix B.4. The result is a factor that modifies the dephosphorylation term in Eq: 5.3:

$$G_Y(t) = k_a N a_0 (1 - a_0) \frac{t_z t_m}{t_m - t_z} \left(\frac{1}{t_m} e^{-\frac{t}{t_m}} - \frac{1}{t_z} \left(1 + \gamma \frac{t_m - t_z}{t_m t_z} \right) e^{-\frac{t}{t_z}} \right), \qquad (5.6)$$

where the additional timescale $\gamma \geq 0$ s and the term $\gamma(t_m - t_z)/(t_m t_z)$ gives the relative strength of active vs. passive dephosphorylation rate at the receptor cluster. The fits using the modified model are presented as red curves in Fig. 26, and the fitting parameters used are summarized in table 1.

We find that inclusion of this additional factor in the fitting procedure drives the two intrinsic timescales t_z and t_m very close together, and that the active component of CheZ only needs to add less than 1% to the area of the negative portion of the Green's function to provide a remarkably close fit to the data. The serine data requires a larger time constant than does the aspartate data with the result $\gamma = 0.53$ s and 0.07 s, respectively. The passive dephosphorylation time is $0.3 \leq t_z \leq 0.52$ s for all fits, which is in close agreement with previous measurements [86]. The methylation rate, t_m, is less than expected for both $\gamma = 0$ and $\gamma \neq 0$. Tu, Shimizu, and Berg estimated $t_m \sim 3$ s [59] based on the shape of the bias curves from the classic measurements of Ref. [76, 14], giving a ratio of $t_m/t_z = 6$. As shown in table 1 we find that a much higher methylation rate is required to fit the data when diffusion is considered.

5.4   FIGURES AND TABLES

Serine			Aspartate		
$\frac{t_m}{t_z}$	γ (s)	$1 + \gamma \frac{t_m - t_z}{t_m T_z}$	$\frac{t_m}{t_z}$	γ (s)	$1 + \gamma \frac{t_m - t_z}{t_m T_z}$
2.4	0	1	1.7	0	1
1.008	0.53	1.001	1.022	0.07	1.004

Table 1: Parameters for Fitting the Temporal Profile of CheY-p Concentration. The timescales t_m and t_z are from the TSB model. The constant γ is the additional CheY-p dephosphorylation proposed in this work. The top row has is the best fit using $\gamma = 0$, whereas the bottom row is the best fit including γ.
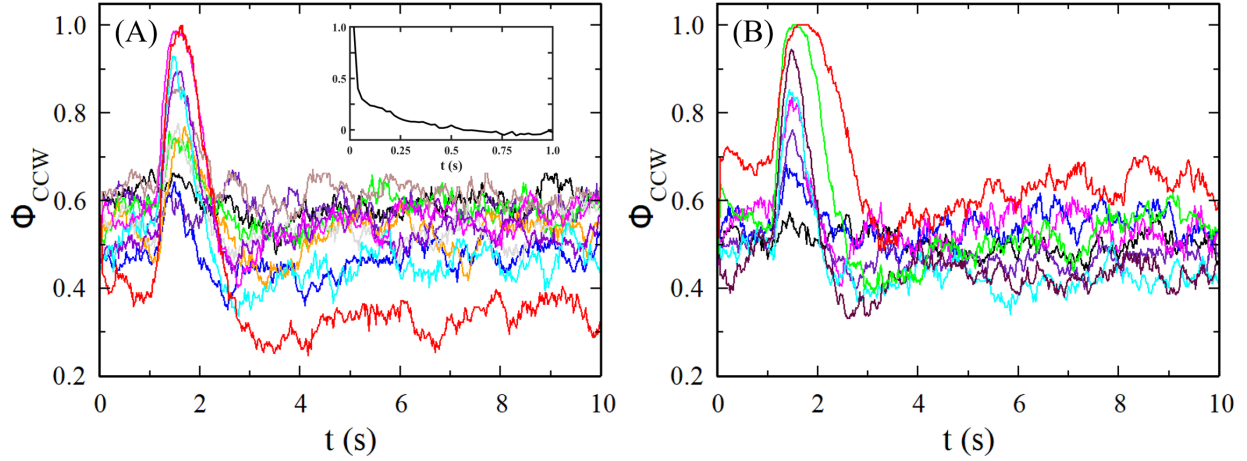
Figure 23: The Behavioral Response to Impulsive Stimulation. (A) *E. coli* RP437 bacteria are stimulated by serine of increasing concentrations, $C_p = 6$ (black), 12 (indigo), 19 (green), 24 (blue), 35 (orange), 39 (brown), 48 (gray), 66 (violet), 77 (cyan), 96 (magenta), and 193 nM (red). The inset shows the result of aligning, and averaging segments of the rotation traces of un-stimulated bacteria. Each segment starts at the beginning of a run and lasts for 1 second. Roughly 1000 events were averaged. (B) The same experiment as (A) but the stimulant in this case is aspartate, $C_p = 19$ (black), 38 (blue), 77 (indigo), 154 (magenta), 308 (cyan), 616 (maroon), 1230 (green), and 2460 nM (red).
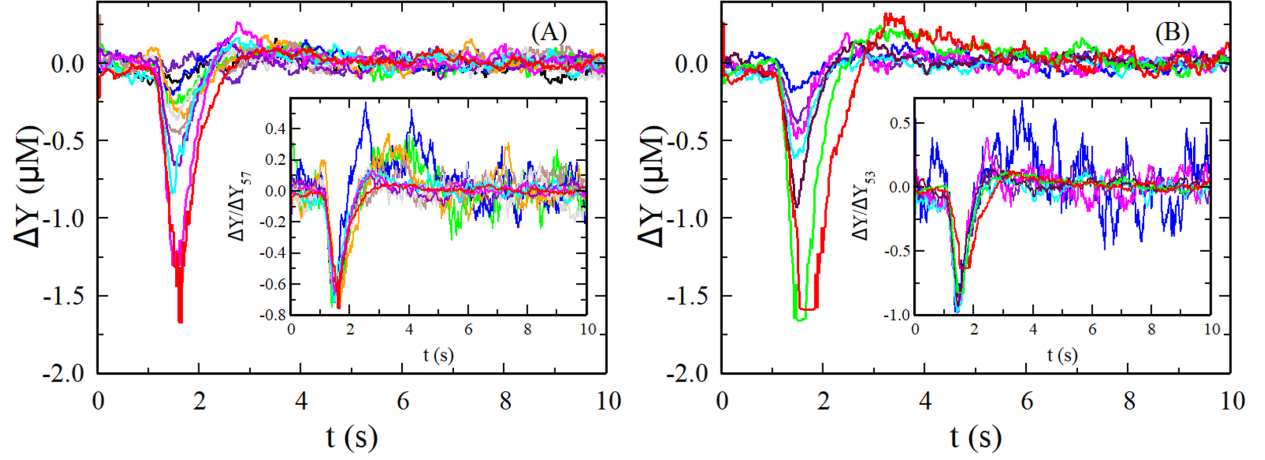
Figure 24: Temporal CheY-p Concentration Profiles Vs Time t. Here we assume that the motor response function in our system is the same as that determined in Ref. [28]. The measured motor bias curves in Fig. 23 are converted to the change in CheY-p concentration as a function of time t. Panel (A) and (B) correspond to serine and aspartate stimulation, respectively. The color code for each concentration is the same as that used in Fig. 23. As in Fig. 20, there is a range of concentrations, $12 \le C_p \le 96 \, \text{nM}$, for which the temporal profiles can be collapsed by re-scaling the data by their maximum values ΔY_{max}. The re-scaled (collapsed) data are displayed in the inset of (A). Likewise for aspartate, the range of concentrations over which the data may be collapsed is $19 \le C_p \le 616 \, \text{nM}$, and the result is displayed in the inset of (B).
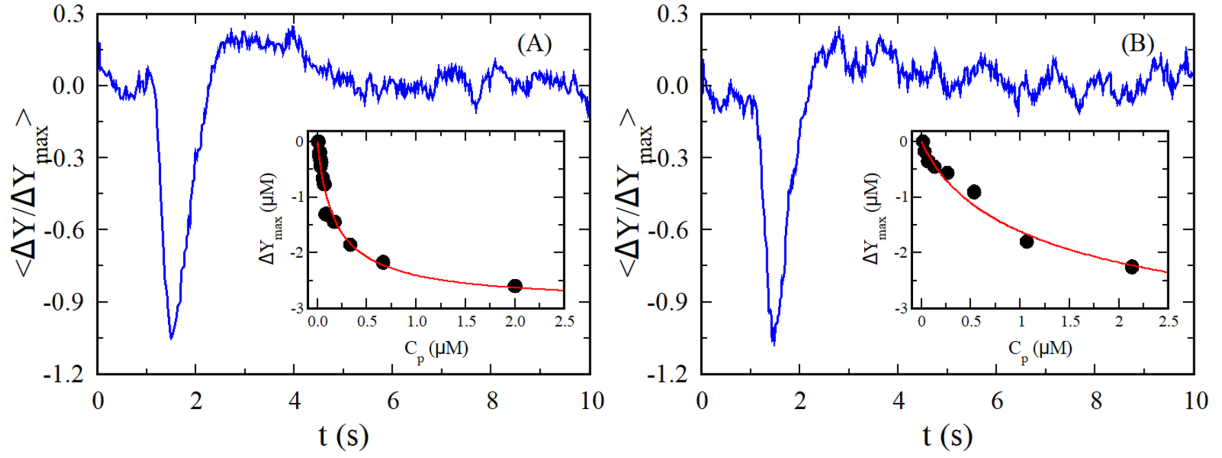
Figure 25: Average Temporal Fluctuation in CheY-p Concentration. The average of the collapsed CheY-p curves $\langle \Delta Y / \Delta Y_{max} \rangle$ from Fig. 24 is shown for serine stimulation (A) and aspartate stimulation (B). The insets show the peak change ΔY_{max} for each concentration tested. The red curves are a fit using the expected amplitude from the TSB model. The fits yield values of $k_I = 70$ nM and $k_A = 500$ nM for serine and $k_I = 300$ nM and $k_A = 8$ μM for aspartate.
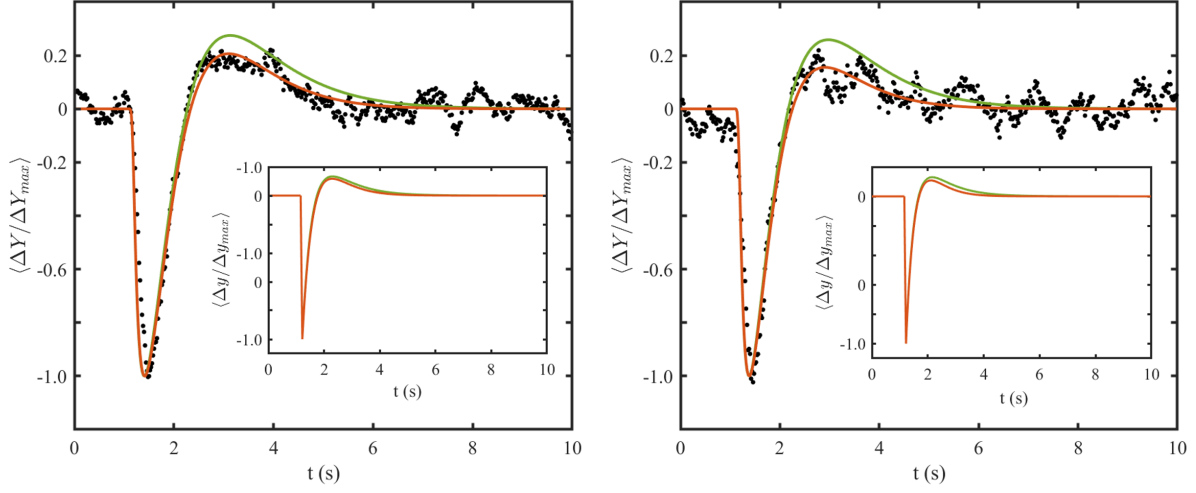
Figure 26: Fitting the Temporal Profile of CheY-p Fluctuations. The collapsed and normalized curves from Fig. 25 are fit using the TSB model with diffusion. For all cases, the concentration at one cell pole is fixed using the TSB model. Panel (A) is the serine stimulation data, and panel (B) is the aspartate stimulation data. The green curves in the main figure (inset) are the normalized CheY-p concentration change at the motor (receptor array). The red curves are fits obtained using our modification that invokes active regulation of CheZ. The concentration is evaluated at $L/2$, reflecting the fact that the receptor array may be at either end of the cell with respect to the motor.

6.0   THE FLAGELLAR BUNDLE of *Escherichia coli*

Peritrichously flagellated bacteria, such as *Escherichia coli* (*E. coli*), perform chemotaxis by modulating the state of flagellar motor rotation: when all the motors are in counter-clockwise (CCW) direction, the flagellar filaments form a coherent bundle that pushes the cell body forward and when one or a few motors is in clock-wise (CW) direction, the bundle falls apart and the cell body twiddles. The former is called a run and the latter a tumble. When swimming in a favored direction, run intervals are extended and tumbling intervals get shorter. The result is a biased random walk that leads the bacterium towards the source of attractant and away from repellent sources. The switching statistics of single motors have been extensively studied. Specifically, it is observed that the distribution of event durations, Δ, for both CCW and CW events are monotonically decreasing functions of Δ and heavily skewed [87]. It is also known that motors adjust the transition rate based on mechanical feedback from the filament [33]. However it is not well understood how, or to what degree, flagellar motors correlate their switching events to make transitions between swimming states of the cell.

In an attempt to address this question we take advantage of a newly discovered effect of bacterial self-trapping near solid surfaces described in Ch. 2 [88]. Briefly, we found that a freely swimming *E. coli* bacterium can be trapped by its own swimming force due to a counter flow that the motion generates near the surface. A trapped cell has its flagella perpendicular to the long axis of the cell body and is aligned with the normal of the surface. The body of a cell in a run state will rotate steadily in the CW direction, whereas a tumble state produces little angular velocity.

The phenomenon of cell-body rotation observed in self-trapped bacteria is akin to the classical rotation assay [26], where a small fragment of a flagellar filament is physically attached to a surface by anti-flagellum antibodies. One significant difference between our method and the classical rotation assay is that the sense of cell-body rotation direction is opposite: a cell in a run state produces CW rotation of the cell body of self-trapped cell, but the same state produces CCW rotation of tethered cells [88]. The other major difference

71

is that the cell body is driven by un-altered flagella, whereas a tethered cell is rotated by only a single motor. Since self-trapped bacteria have intact flagella that can form a coherent bundle, they provide a unique experimental opportunity for studying dynamic fluctuations of flagellar bundles. In this study we consider the rotation of self trapped bacteria unexposed to a chemotactic stimulus. These results are compared with an analogous measurement on the rotation of single motors. For the single motor experiment, we use XLWU100, a strain that produces mutant "sticky" flagella that readily adhere to the glass surface.

6.1   RESULTS

Individual cells rotating on the glass surface were found and recorded for several 12 second intervals. Each cell contributed an average of 17 trials (200 s), for a total recording time of 3120 s for RP437 (wt) and 2916 s for XLWU100 (sticky filaments). Custom scripts written in matlab extracted the angular velocity, Ω, from the recordings and converted the velocity into rotation state, $\omega(t)$. For XLWU100, ω is set to 1 when the cell is turning CCW and 0 otherwise. For RP437, ω is the state of the behavior of the cell rather than simply the rotation direction of any single motor. The method used here was presented in detail in chapter 2 and we assign 1 to the run state and 0 to the tumble state by using Eq. 2.2. From the resulting binary traces, we extracted the durations (dwell times) of all CCW (1) and CW (0) events. Events that bordered a recording boundary were excluded. Note that even though the "run" state for trapped cells produces a CW cell body rotation, we refer to these intervals as "CCW" due to the motor rotation direction.

Fig. 27 displays our measurement of the dwell-time PDFs $P_\Delta(\Delta)$ for both strains. For tethered cells (XLWU100, panel (A)), $P_\Delta(\Delta)$ decays monotonically for both CCW and CW intervals, and $P_\Delta(\Delta)$ is strongly non-exponential for short Δ. However, the long-duration decay does appear to follow a straight line on the semi-log plot, indicting that asymptotically $P_\Delta(\Delta)$ may be approximated by an exponential function. We also noticed that the magnitudes of PDFs for the two intervals are nearly identical, which indicates that the motor bias is about 50%. This is significantly lower than the run-bias typically seen in free-swimming

cells which is about 80% or higher [36]. Such a large difference may be explained by the fact that the rate of motor switching is strongly influenced by the load. As shown by Fahrner et al. [33], the average switching rates from CCW to CW (k^+) and vice versa (k^-) decrease with the load, and this load-dependence is much stronger for k^- than for k^+. For XLWU100, cell-body rotation is driven by a single motor that significantly increases CW interval length, making the bias close 50%. This is consistent with Ref. [33].

The switching behavior of RP437 is quite different than that of XLWU100 as shown in Fig. 27(B). Although CCW and CW dwell-time PDFs appear to follow each other in short times, their long-time trend is strikingly different, e.g., whereas the PDF for the CCW intervals is approximately exponential in long times, the PDF for CW intervals decays much more rapidly and can be mimicked approximately by a Gaussian function, as delineated by the green line. The varied behaviors between RP437 and XLWU100 are interesting, informing us how the presence of a flagellar bundle affects run and tumble of a swimming bacterium.

While the above observation is interesting, the presentation using $P_\Delta(\Delta)$ is neither informative nor useful for analyzing and understanding the mechanism underlying transitions from a run to a tumble and vice versa. In our opinion the quantity of biophysical significance is the transition rate k, and how this rate changes with external conditions. The dwell-time distribution is related to this transition rate but in a complicated way. An important clue of our data is that motor switching kinetics clearly involve multiple time scales. The phenomenon therefore should be treated as an non-stationary Poisson process characterized by a time-dependent rate $k(t)$. In such a process, the survival probability $P(t)$ has a simpler mathematical form than the dwell time PDF: $P(t) = \exp(-I(t))$ for the former and $P_\Delta(\Delta) = k(\Delta)\exp(-I(\Delta))$ for the later, where $I(t)$ is the integrated transition rate given by $I(t) \equiv \int_0^t k(t')dt'$. Given the transition rate $k(t)$, $P(t)$ and $P_\Delta(\Delta)$ are related by a time derivative, $P_\Delta(\Delta) = -\partial P(t)/\partial t|_\Delta$. In light of this observation we seek to present our data using the survival probability $P(t)$ instead. To do so we numerically integrate the measured $P_\Delta(\Delta)$ to obtain $P(t)$ and the results are plotted in the insets of Fig. 27. An added benefit of converting to the survival probability is that $P(t)$ appears much smoother than the original data.

To gain more information about the switching mechanism we next proceed to extract

the integrated transition rate $I(t)$ from the survival probability using $I(t) = -\ln P(t)$. This quantity is related to $k(t)$ by an integration and it therefore can tell us how $k(t)$ behaves as a function of time t. The results are plotted in Fig. 28 for the two bacterial strains. For a stationary Poisson process, $I(t)$ is linear in time, but none of the curves in Fig. 28 (A) or (B) behave in this way. The general trend is that $k(t)$, which is proportional to the slope of $I(t)$, is quite large for small times before decreasing and finally reaching some constant value for large times. Moreover, for both bacteria, CW transition rates (orange and green squares) are higher than the CCW rates (red and blue circles), which is consistent with normal swimming behavior of *E. coli* cells. Finally, whereas the CW and CCW integrated switching rates of tethered cells in (A) are similar for the two motor directions, both in their functional forms and in magnitudes, the $I(t)$ for wt bacteria (B) are considerably different for the two directions. Specifically, $I(t)$, or for that matter $k(t)$, for CW (or tumble) state is significantly higher than its counterpart for CCW (or run) state, suggesting that switching dynamics for cell-body rotation driven by a single motor and by a flagellar bundle are quite different. We investigate this discrepancy further in the discussion.

6.2 DISCUSSION

Based on the above qualitative analysis, we conjectured the following time-dependent switching rate, $k(t) = k_0(1 + t_0/t)$. This function has a singularity as $t \to 0^+$ and becomes a constant in long times $t \gg t_0$, where t_0 is a crossover time. This gives the integrated switching rate,

$$I(t) \equiv \int_{\delta t}^{t} k(t')dt' = k_0 \left((t - \delta t) + t_0 \ln \left(\frac{t}{\delta t} \right) \right), \tag{6.1}$$

where δt is a cutoff time that regulates the singularity at $t = 0$. As shown by the solid lines in Figs. 28, this simple mathematical form mimics our experimental data reasonably well particularly with both states for tethered cells (A) and for CCW rotation of wt cells (B). In those cases, the typical long-time transition rate k_0 is about 0.5 s^{-1} and the cross-over time t_0 is about a second. In all these cases, the cutoff δt is small, i.e., comparable to the inverse video frame rate, which is to be expected. This simple mathematical form however

only provides a marginally acceptable fit to CW rotation of wt cells as shown by the green curve in Fig. 28 B. As we shall discuss below, the reason for this is because a tumbling for wt cells is a mixture of different states governed by additional biophysical processes. For convenience, the numerical values for k_0, t_0 and δt are tabulated in Table 2. Aside from CW state of wt cells, the reasonably good agreement between the proposed transition rate $k(t)$ and the observation suggests that an incipient state is more likely to "fail" in early times than in late times. This provides a useful clue about how flagellar motor switch may operate, and it should also serve as a touchstone for any mathematical model that attempts to describe the *E. coli* flagellar motor switch.

We next compare in Fig. 29 the integrated switching rates $I(t)$ between the two bacteria. For CCW intervals, we found surprisingly that $I(t)$ is nearly identical for RP437 and XLWU100, indicating that the transition rate $k(t)$ of the bundle is nearly identical to that of a single motor. We posit that this can happen if in the CCW state or a run, the flagellar bundle is a highly coherent object driven by a single dominant filament. Perhaps due to its special location on a cell body, this dominant flagellum determines the cell body rotation, which in turn enforces the cohesiveness of the bundle. Furthermore, the torque on the cell body generated by the bundle is largely unchanged by the occasional switching of a non-dominant flagellum. Since the switching rate k is a function of the load [33], it follows that the load on the dominant flagellum must be similar to that of a single tethered motor.

The situation is different for the CW (tumble) state where we found that whereas $I(t)$ is smaller for the wt cells than XLWU100 in short times ($t < 0.5\,\mathrm{s}$), $I(t)$ is significantly greater than that of XLWU100 in long times ($t > 0.5\,\mathrm{s}$). Inspection of data (green squares) in Fig. 29 reveals two different tumbling behaviors for wt cells; one that occurs in short times and the other in long times. For short times $t < 0.3\,\mathrm{s}$, $I(t)$ for both bacteria has the same functional form but a different amplitude. This is demonstrated in the inset by a re-scaling of the curve for RP437 that makes the two curves collapse. This strongly suggests that very brief (<0.3 s) CW events of the dominant filament only slightly perturb the flagella bundle such that the torque is reduced, but quickly regained upon resuming CCW rotation. Such a perturbation, which we call a mini-tumble, is short lived and seems to only effect the speed of the cell body when it occurs in the dominant flagella. Our measurement also shows that

the magnitude of the switching rate in this episode is suppressed compared to a tethered motor, suggesting that the load on this single flagellum is higher than that of a tethered motor [33]. This is plausible since a motor reversal motor would turn the filament CW, i.e., against the direction of the rest of the flagella in the bundle. It should be mentioned that a short tumble due to only a single motor switch from CCW to CW has been previously proposed and observed using a novel fluorescence labeling technique [1, 3]. Our finding adds more evidence that a single motor reversal may cause a tumble, and we also provides a means to quantify such a behavior.

Let's turn now our attention to the long-time behavior of the CW state for wt cells. Different from the minis, a long tumble state has a greater transition rate. We posit that this state is characterized by a greater "disorder" in the flagellar bundle; in the extreme case one may assume that all motors are in the CW direction. To make a transition to form a coherent bundle, various scenarios are feasible. (i) Suppose that the transition is a serial process, i.e., one flagellum after another makes a transition from CW to CCW, which could be the case that each motor is triggered by a CheY-p concentration wave inside a cell observed in Ref. [89]. In such a case, the rate of transition to a coherent bundle is dictated by the motor with the slowest transition rate and one expects the overall transition rate will be even lower. But this is what is not observed in our experiment. Alternatively, (ii) suppose that the transition only occurs after the dominant motor has switched to CCW and has rotated through a large enough angle to organize the bundle. Under this assumption, a short CCW event that succeeds a sufficiently long CW event is "filtered out", because such short events only partially organize the bundle and thus do not provide enough torque to significantly accelerate the cell. This second scheme explains the brief decrease in the transition rate near $t = 0.2$s, as the dwell time PDFs show most CCW single motor events are very short. Suppose that the flagalla of the cell are in a completely disordered state, and that to transition to an ordered state the dominant flagellum must drive cell body rotation over a critical angular displacement, say θ_C. The mean transition time is then given by $\bar{t} = \theta_C/\dot{\theta}$, where $\dot{\theta}$ is the mean angular speed. Due to noise in rotation, the mean transition time is expected to be smeared over a range of time, say Δt. Thus the transition time t has a distribution that peaks at $\bar{t}$. For simplicity, we assume such a distribution to be given

76

by $p(t) \propto \mathrm{sech}(\frac{t-\bar{t}}{\Delta t})$, which is peaked at $\bar{t}$ and decays exponentially for large times. Using $k(t) = k_1 p(t)$, where k_1 sets an overall scale of the transition rate, we found that the long-time behavior of the CW interval of RP437 can be well described by this form. A fitting procedure yields, $k_1 = 4.1\,\mathrm{s}^{-1}$, $\bar{t} = 0.34\,\mathrm{s}$ and $\Delta t = 0.76\,\mathrm{s}$. The result of this combination of short time and long time behaviors is displayed by the blue curve in the Fig. 29. The fit is good, demonstrating that this simple phenomenological model captures the essential features of the transitions between states.

A better understanding of the underlying mechanism of the motor switch itself is highly desirable. There has been some theoretical work on modeling the allosteric nature of the switch, most notably in Ref. [90]. In this model, the coupling between protomers on the motor switch ring provides the high gain observed in [28]. However it is unclear whether such a model will provide the switching rate consistent with our observation: $k(t) = k_0(1 + t_0/t)$. Unfortunately this part of the analysis is beyond the scope of our current work.

strains	XLWU100			RP437		
parameters	k_0 (s^{-1})	t_0 (s)	δt (s)	k_0 (s^{-1})	t_0 (s)	δt (s)
CCW	0.54	0.93	0.037	0.40	1.73	0.06
CW	0.58	1.01	0.02	2.29	0.24	0.05

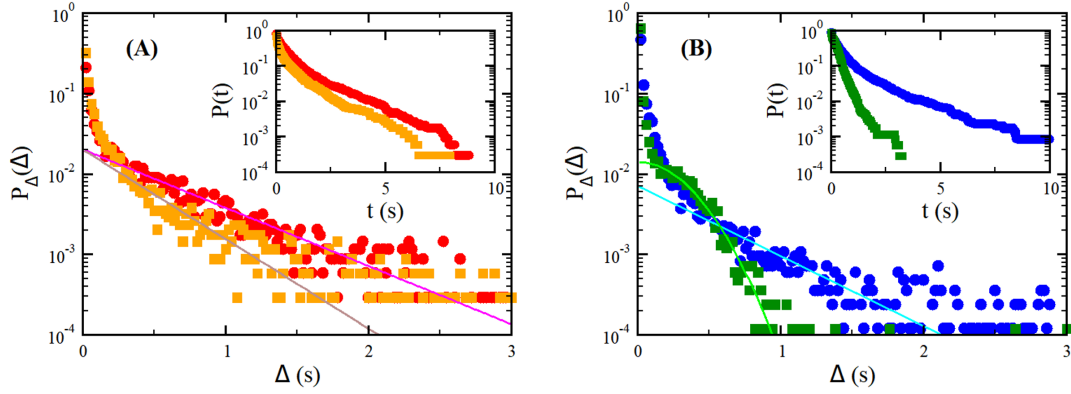Table 2: Fitting Parameters for the Integrated Switching Rates.

Figure 27: Dwell-Time PDFs for *E. coli* XLWU100 and RP437. (A) For tethered bacteria (XLWU100), the dwell-time PDFs $P_\Delta(\Delta)$ are similar for the CCW (red circles) and CW (orange squares). Both PDFs decay rapidly for small time intervals and have a broad tail, which is approximately exponential as delineated by the straight lines on the semi-log plot. A total of 14 tethered cells were recorded. (B) For self-trapped bacteria (RP437) that have an intact flagellar bundle, there is a distinct difference in the PDFs for CCW (blue circles) and CW (green squares) intervals. Whereas for the CCW intervals, the PDF appears similar to the tethered cells in (A), the PDF for the CW intervals has a very different functional form particularly for large time intervals. As delineated by the green solid line, this regime is not exponential but can be approximately mimicked by a Gaussian. A total of 13 tethered cells were used. The insets of (A) and (B) are the survival probability for XLWU100 and RP437, respectively. In both cases $P(t)$ decays more slowly than $P_\Delta(\Delta)$, indicating that they have a different time dependence.
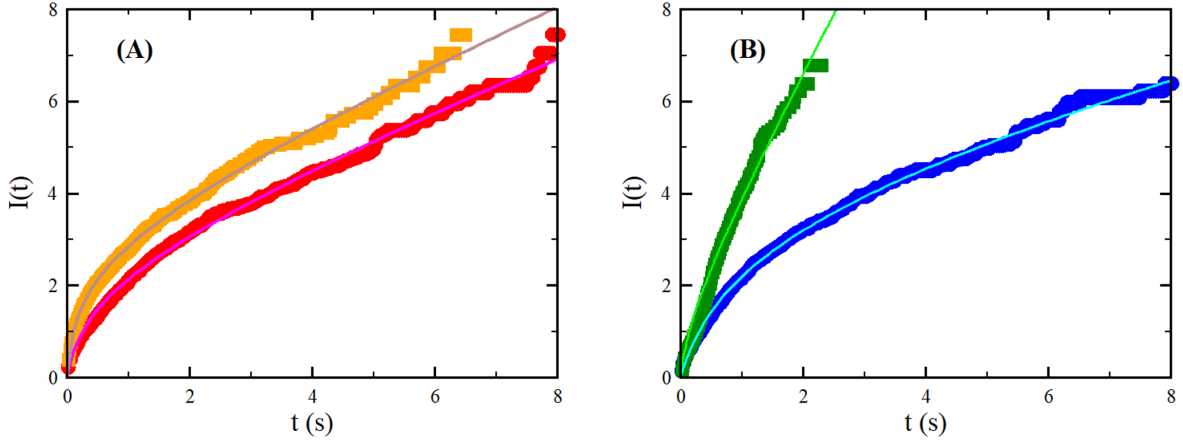
Figure 28: Integrated Switching Rates $I(t)$ for *E. coli* XLWU100 (A) and RP437 (B). All measurements show that the integrated switching rates $I(t)$ is not linear in time, suggesting that flagellar motor switch is not a stationary Poisson process. Moreover, since $I(t) = \int_{\delta t}^{t} k(t')dt'$, it is expected that the CW switching rates (orange and green squares) in general are higher than the CCW switching rate (red and blue circles). For tethered bacteria (XLWU100) for which the cell-body is driven by a single motor, $I(t)$ for both CCW and CW have a similar concave form, indicating that the transition rate $k(t)$ is high in short time and becomes smaller in long times. The same can be also said about the more complicated case of RP437 for which cell-body rotation is driven by the flagellar bundle. The difference between the CCW and CW in this case is more pronounced as the CW switching rate is considerably higher than the CCW rate, particularly for large times. The solid lines in the figure are fits using $k(t) = k_0(1 + t_0/t)$ with k_0 and t_0 being the adjustable parameters (see discussion in the main text).
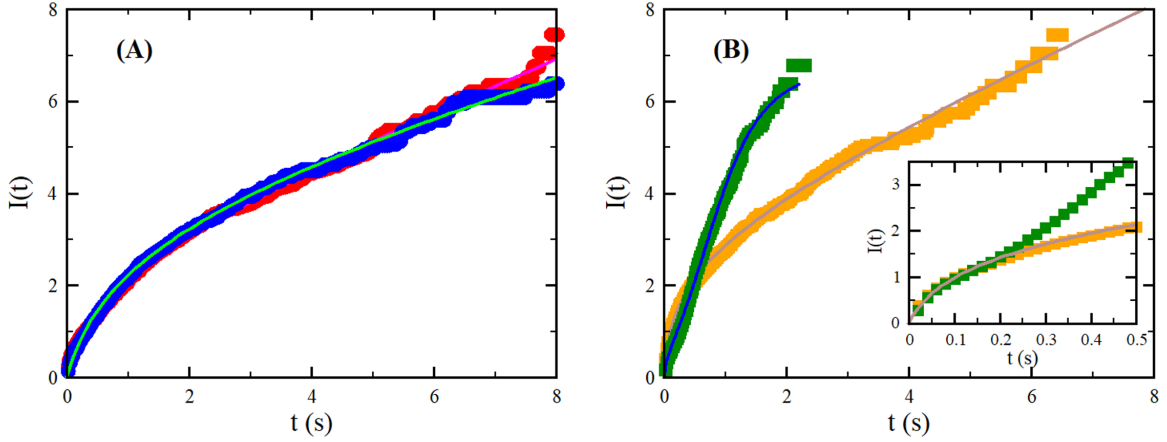
Figure 29: Comparisons Between XLWU100 and RP437. For the CCW (run) intervals (A), the integrated switching rates $I(t)$ for a single motor and for the flagellar bundle are found to be surprisingly close, suggesting that for this interval the switching of a dominant motor is required to end the interval. On the other hand, for the CW (tumble) intervals (B), the integrated switching rate $I(t)$ for the bundle (green squares) is very different. In short times, $I(t)$ is lower than that of a single motor (orange squares) but for $t \geq 0.5\,\text{s}$, $I(t)$ rises sharply. The short time tumbling behavior, which we call mini-tumbles, involves a single flagellum in the bundle. But the long-time tumbling behavior involves multiple flagella, and it takes more time to organize into a coherent bundle. The inset depicts the short-time behavior of RP437 (green squares) and RP437 (orange squares); here, $I(t)$ for RP437 has been multiplied by a factor of 1.7 to make the two curves overlap as they approach $t = 0^+$. The similar functional forms of the two curves in this region suggest the underlying physics are the same, i.e., the transition is govern by the single motor statistics.

APPENDIX A MATERIALS AND METHODS

A.1 BACTERIA, PLASMIDS AND GROWTH

E. coli RP437 is considered as wild-type (wt) in this experiment and other strains were derived from it. For rotation measurements, two additional strains were used: the ΔCheY mutant RP5232 [91], and the ΔFliC mutant XLWU100 [88]. XLWU100 was transformed with the plasmid pFD313 [92], which confers a "sticky" mutant FliC and provides an easy method of single motor tethering. For the FRET measurements, strains RP437 and its derivative VS104 were used. VS104 is a double-deletion (*cheY and cheZ*) mutant and is supplemented with the plasmid pVS88, which encodes chimeric proteins CheY-YFP and CheZ-CFP. The construction of VS104 and pVS88 and their biophysical properties are documented in Ref. [64].

Bacillus subtilis strain 3610 was used as a wild-type. We also tested strain DK3451 (ΔswrA, ΔslrA), which produces fewer flagella on average per cell. DK3451 was constructed by Daniel Kearns (Dept. of Biology, Indiana University), but the construction at the time of this writing is unpublished.

A.1.1 Bacterial Growth

All growth for measurement using *E. coli* was carried out at 33°C using tryptone broth (TB: 1% tryptone powder, 0.5% NaCl). Single colonies were picked from a plate and grown overnight in tubes containing 3 ml TB. Overnight cultures were diluted 1:100 into 10 ml fresh TB in a a 125 ml flask, and grown for 4 hours. Antibiotics were supplied at all stages of growth when appropriate, and inducer (25 μM isopropyl β-D thiogalactoside) was added to flasks for VS104 w/ pVS88. *Bacillus subtilis* was grown using the same procedure except the growth medium used was Luria Broth (LB: 10g/L NaCl, 10g/L tryptone powder, 5 g/L yeast extract) and the growth temperature was 37°C.

The bacteria were harvested and washed twice in a motility buffer (MB: 10 mM KPO$_4$,

0.1 mM EDTA, 1 μM L-methionine, 67 mM NaCl, 10 mM sodium lactate) by centrifugation at 4×10^3 rpm for 3 s. Cells to be tethered were subjected to flagella shearing: the freshly grown bacteria were passed repeatedly through two 21 gauge syringe needles connected by a Tygon tube $\sim$ 5 cm long [76] and were washed once more before continuing.

For good motility, we found that it was helpful to incubate the washed bacteria on a shaker with gentle swirling at room temperature for at least 30 minutes. For FRET measurements, glass surface was treated with poly-L-lysine (0.01%, 150k-300k, Sigma-Aldrich) and allowed to dry overnight. The surface was washed once with clean MB and then 500 μl of cell suspension was left to sit on the cover-glass of the observation chamber for 2 minutes. The observation chamber was then gently rinsed several times with MB to remove any cells that did not adhere to the surface.

For rotation measurements, the same procedure was followed except without treating the glass surface with poly-L-lysine. Rinsing of the chamber with fresh MB does little to remove cells that are near the glass surface but greatly reduces the swimming cells that would otherwise aggregate near the surface over the course of measurement.

A.1.2 Bacterial Growth for Microbiology

All growth for plasmid transformation and P1 transduction was carried out at 37°C in LB.

A.2 THE CONSTRUCTION AND USE OF MICROPIPETTES

Micropipettes were pulled from borosilicate glass capillary tubes 1.5-1.8mm ID. Capillaries were first "fire polished" by briefly holding the ends in a flame to smooth the sharp edges. The capillaries were then washed using 0.02 μm filtered 95% ethanol, allowed to dry overnight, and stored for later use in a clean container. A fresh micropipette was pulled for each measurement using a micro-electrode puller (Narishige PP-830) set such that the small end of the pulled pipette was $\sim$ 1.5 μm in diameter. Finished micropipettes were filled using

a nonmetalic syringe needle (MicroFil, World Precision Instruments). After filling, the tip would be placed into the micropipette holder which created an air-tight seal so the interior of the capillary could be pressurized (see Fig. 30 B). Pressure was controlled by an adjustable low pressure regulator and an electromechanical valve (Parker Instruments, picospritzer III) with timing controlled by custom code written in LabVIEW (National Instruments). The micropipette was translated by a 3-axis micro-manipulator (Siskiyou, Grant Pass, OR) with an accuracy of $\sim 0.5\,\mu$m.

A.2.1 Flagellar Staining

In order to visualize the flagella of a bacterium, a new real-time staining technique was implemented. In this technique, a micropipette, similar to the one used for chemical stimulation, was filled with Ryu Flagella Stain (Remel/Fisher Scientific, Pittsburgh, PA) and positioned several microns away from a surface-bound bacterium that rotated in a specific direction. The chemical was then gently released by applying a small positive pressure. To prevent clogging of the micropipette tip, Ryu Flagella Stain was first diluted by a factor of 10 using distilled and deionized water and then filtered through a $0.2\,\mu$m syringe filter.

A.2.2 Use of a Micro-Valve

A new technique developed in this work is the use of a 2 μm diameter polystyrene microsphere, referred to as a "bead", as a check-valve to create precise and small injections of chemicals. The end of the pipette is submerged, as in Fig. 18, to a depth of ~ 5 to 8 mm. The equilibrium fill height for this setup was found to be ~ 3 cm, and micropipettes were always filled to between 1.3 and 1.6 cm. These parameters ensured that the inflow was rapid in the absence of a bead.

Microspheres used to create the valve were added to the sample before the bacteria: 2 μl of 0.025 % (V/V) micropheres in water were placed directly on the glass, and spread around. It was easy to find spheres on the surface, even after adding bacteria and rinsing several times to remove excess cells. Once a microsphere was found, the pipette tip would be submerged and quickly moved near the sphere. The syringe connected to the setup (see

Fig. 30) was then used to create a sharp drop in pressure that would pull the bead onto the tip. Subsequent short pulses would eject the bead along with the solution, and the bead would return to reseal the tip. High speed recordings showed that beads ejected from the tip took roughly $400ms$ to return.

In many occasions, it was found to be advantageous to create a hinge so the bead would be pushed out of the way rather than ejected from the tip. To create a hinge, the very end of a filled and ready to use micropipette would be submerged in 4^oC poly-lysine solution for $\leq 5\ s$ before continuing as normal. Once a bead was pulled onto the tip, it was typically adhered over the entire opening. The pressure syringe was then used to slowly apply increasing pressure until the seal would break, and the bead would hinge out of the way. The broken bonds would only rarely reform.

In both cases, i.e., with poly-lysine or without, we found that beads stuck to the micropipette could be removed by a pass of the tip through the surface of the liquid in the sample. This was necessary if the seal could not be broken due to excess poly-lysine, and such action would reduce the amount adhered to the tip.

A.2.3   Pipette Calibration

Fluorescein at a concentration of 64 μM was always present in the solution used to fill the tip. Calibration of the pulse was accomplished by observing fluorescence at the location where a rotating cell would be placed during a measurement and then adjusting the pressure regulator. The optics for this calibration are shown in Fig. 30 A and the pneumatics are shown in Fig. 30 B. A 442 nM laser was focused into a diffraction limited spot at the location where the rotation axis of a tethered or trapped cell would be placed. This light would then excite the dye ejected by a pulse, and the emission light was collected by a single photon counting module (SPCM) operating at 100 Hz. The pulse volume was standardized day to day by using fluorescent microspheres (yellow, 400 nM diameter, Polyscience) as a reference intensity. The pulse volume would drift with room temperature and evaporation of the sample, so the calibration would be re-checked every $\sim$ 30 minutes during measurements.

By comparing the intensity from a calibrated pulse, to the intensity read from a sample

of uniform fluorescein, the peak concentration at the measurement location was found to be 7% of the concentration in the tip, C_0, resulting in a dilution factor of $C_0/C_p \approx 14$.

To estimate the volume ejected by the pulse, high speed strobe lighting was combined with long exposure imaging. By lighting in this way, successive exposures were overlaid on the same image. The distance between each image of the bead was multiplied by the chopping rate to obtain the average speed over each interval. Fig. 31 shows the result of several measurements performed in this way.

A.2.4 Spacial Variation of Concentration

A typical *E. coli* bacterium is ~ 3 μm in length, so the tip of a rotating cell in our behavioral assays traces out roughly a circle 6 μm in diameter. The approximate solution, Eq. 4.1, is plotted in Fig. 32 for several distances from the tip and is shown to strongly vary over the diameter of a cell body rotation trajectory. If this variation was important, we should expect cells exposed to a non-saturating concentration to respond more often if they were closer to the pipette during the pulse. The histograms presented in Fig. 33 show that probability of behavior response is not a function of the position of the cell body at the time of the pulse.

To compare the concentration exposed to a single cell in our rotation assay to the concentration experienced by a group of cells in our FRET measurement, we must consider the variation of the chemoattractant in both space and time. The insets in Fig. 32 plot the time of the peak concentration, denoted t_p, as well as the peak concentration as functions of distance from the origin. The time of the peak is ~ 20 ms later for the furthest cells, which is much smaller than the 100 ms time resolution of the FRET measurements. To account for the spatial variation, we average the peak concentration experienced by the cells in the field. Let x denote the distance from the origin. The origin is placed at the glass surface directly under the opening of the pipette. Denote the peak concentration by $C_p(x)$, and the average peak concentration by $\overline{[s]}$, and note that $C_p(x = 8 \ \mu\text{m}) \equiv C_p$ as used throughout the text. Then,

$$\overline{[s]} = \frac{2}{R^2} \int_0^R C_p(x) \, x \, dx \ . \tag{A.1}$$

In the FRET measurement, the bacteria within a radius $R = 12\,\mu$m were imaged by the CCD camera. The average peak serine concentration $\overline{[s]}$ in this region is found to be very close to the peak concentration C_p experienced by a single cell at a radius of $8\,\mu$m, or more precisely $\overline{[s]} \simeq 1.1 C_p$. This value of $\overline{[s]}$ was used to plot the FRET measurement in Fig. 12.

A.3   RAPID SAMPLE HEATING VIA IR LASER

Our temperature measurements were carried out using the setup depicted in Fig. 35 D, i.e., a cleanly cleaved optical fiber was submerged near a bacterium. Even though the laser beam (1440 nm) was strongly divergent, this simple setup was more efficient in heating the fluid than refocusing the beam by a lens. To calibrate temperature as a function of laser power and duration, we use fluorescein at a concentration of $50\,\mu$M, and the result is displayed in Fig. 34. We found that fluorescent intensity of this dye changes with temperature and can be readily measured using a CCD camera. The fluorescein derivative BCECF has been used to calibrate temperature perturbations in previous studies [93, 94]. Here we found that fluorescein works similarly to BCECF.

A.4   DATA COLLECTION

All experiments were carried out at $\sim 24^o$C on an inverted microscope (Nikon, TE2000). Images and video were captured using a back-thinned CCD camera (Hamamatsu, C9100), with camera timing controlled by custom codes written in LabVIEW, and relayed through a PCI board (National Instruments, PCI 6600). The chemical and heat pulse durations of 25 ms and 50 ms, respectively, was kept consistent for all experiments.

A.4.1 Rotation Measurements

For all rotation measurements, an overlay over the live video feed ensured consistency with the schematic of Fig. 35. All experiments used a frame rate of 50 ms, with a 5 ms exposure time per frame.

A.4.2 FRET Measurements

Instead of measuring light emission from the entire cell, we focused on light intensity in puncta at poles of each bacteria where receptors formed a cluster. Upon stimulation by serine above some threshold value, light emission from YFP decreases but light emission from CFP increases, which is consistent with Ref. [64]. We interpret this effect as dissociation of CheY-CheZ pairs on chemoreceptor clusters. Since CFP was more resistant to photobleaching and had a larger signal-to-noise ratio, all of our measurements were performed using the cyan channel.

In a measurement, the micropipette is positioned 5 μm above the surface of the glass in the center of a small image frame roughly 12 μm in radius. Our recording rate was limited to 10 fps due to the low intensity of the emission, and only a single pulse on each field was collected due to rapid photobleaching. The light intensity from each punctum was normalized and averaged together to yield a population average $I(t)$. This signal was then corrected for photobleaching by fitting, excluding 4 seconds immediately following the stimulation, with an exponential. The resulting curve is the population average of the relative cyan intensity.

A.5 IMAGE ANALYSIS

All image analysis was performed using custom codes written in MATLAB (Math-Works).

A.5.1 Rotation Measurements

Videos were collected using phase-contrast microscopy so that cell bodies have a lower intensity in the image than the background, as in the example of Fig. 37. These videos were cropped and processed for analysis following the steps explained by Fig. 36.

Let $I(i, j)$ be the intensity of pixel (i, j), and (X, Y) denote the coordinate of the center of intensity:

$$
\begin{bmatrix} X \\ Y \end{bmatrix} = \frac{1}{\sum I(i,j)} \begin{bmatrix} \sum i I(i,j) \\ \sum j I(i,j) \end{bmatrix} , \tag{A.2}
$$

where the sums range over all pixels of the cropped image. The cell body for each frame was determined by finding the eigenvectors of a moment tensor, $\mathbf{T}$ defined by

$$
\mathbf{T} = \begin{bmatrix} t_{ii} & t_{ij} \\ t_{ji} & t_{jj} \end{bmatrix} \tag{A.3}
$$

where

$$
t_{ii} = \sum_{ij} (X - i)^2 I(i,j) , \quad t_{ij} = \sum_{ij} (X - i)(Y - j) I(i,j) \text{ etc.}
$$

The eigenvector that corresponds to the largest eigenvalue will point in the direction of the long axis of the cell. Note that this method requires an asymmetric cell body. The sign of the vector is chosen based off the center of intensity of the frame, with respect to the average center of intensity over all frames. Fig. 37 shows this method applied over several frames. Care was taken during data collection to avoid cells that were rotating near or above the Nyquist frequency, however only rarely were cells encountered that rotated at such a high speed.

The result of this code applied to a video is a vector that rotates in the plane from which the angular velocity is be determined.

A.5.2 FRET Measurements

Puncta of individual stationary cells were picked by hand from the first frame of each FRET video. In each frame, a 3×3 region around each selected point was cropped and searched for the brightest pixel, as shown in 38. An estimate of the background was made

89

by averaging the 10 dimmest pixels from the first 10 frames, and subtracted from the bright pixels selected. The time trace of each bright pixel was then normalized to the initial value, corrected by photo bleaching, then averaged together to form an intensity trace for the video.
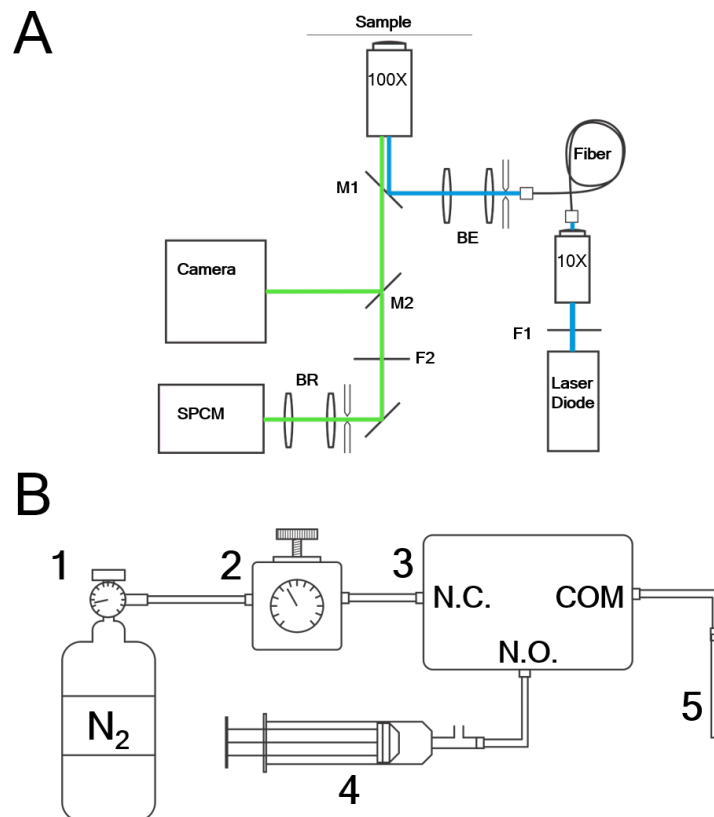
A.6   FIGURES

Figure 30: Experimental Setup for Valved Micropipettes. A) The optics for calibration: light from a 445 nm laser is passed through a neutral density filter (F1) before being coupled into a single-mode optical fiber by a 10X microscope objective. After the optical fiber the beam is expanded by a pair of lenses (BE) before being deflected into the sample by a 515 nm dichroic mirror (M1). The light from the sample can be diverted either into the camera by a movable mirror (M2) or continue on through a beam reducer (BR) and into the single photon counting module (SPCM). An additional band-pass filter (F2) was placed before the SPCM. B) The pneumatic setup: 1) The pressure source was a compressed nitrogen cylinder. 2) A low pressure regulator was used to change the pressure setting. 3) An electro-mechanical valve switched between the pressure source and the atmosphere. 4) A 60 ml syringe was connected using a three-way adapter. Normally the adapter was left open to atmosphere but could be closed whenever positive or negative pressure supplied by the syringe was needed. 5) The micropipette holder.
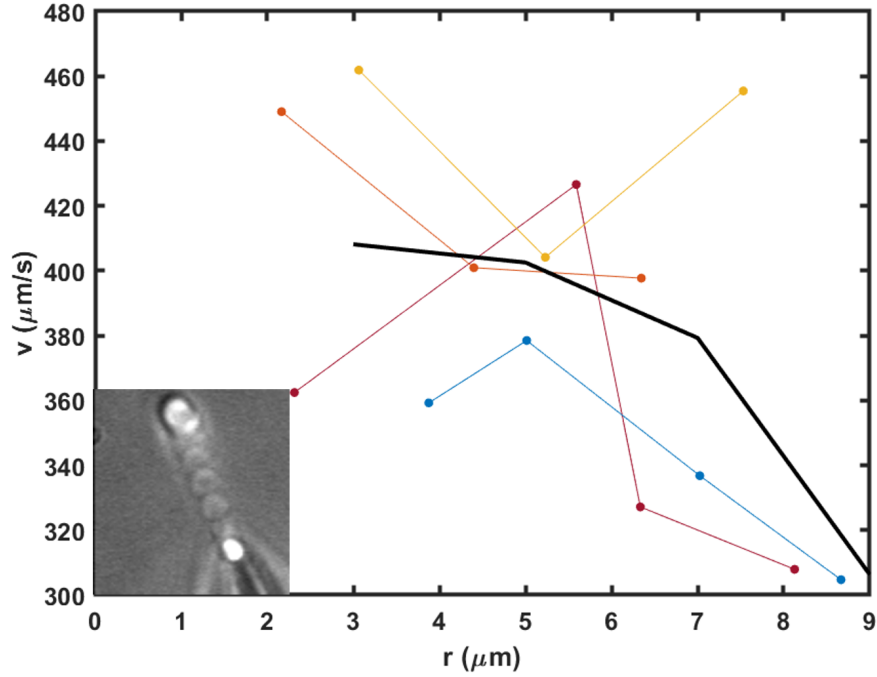
Figure 31: The Velocity as a Function of Distance From the Pipette Tip. The main plot shows the velocity as a function of distance from the pipette tip, r, calculated for four strobe images (colored lines with dots). The first interval included time when the bead was stationary and was excluded. The heavy black curve is the average of the individual measurements, and shows that the velocity approaches the opening with no slope. The strobe lighting was accomplished by chopping the illumination at 167 Hz. An example of one of the images, with an exposure duration of 75 ms, is shown at the lower left corner.
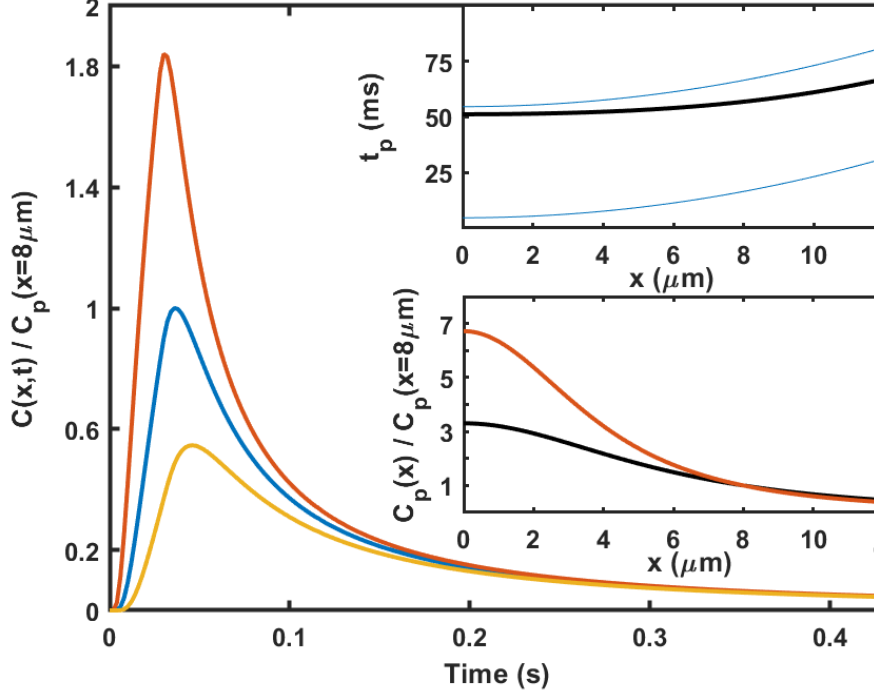
Figure 32: The Spacial and Temporal Variation of The Concentration From a Micropipette Tip. The main figure shows the concentration normalized by the peak at $x = 8$ μm, $C_p(x = 8$ μm, for $x = 5$ μm (red), $r = 8$ μm (blue), and $r = 11$ μm, (yellow). Top Inset: the heavy black curve shows the time of the peak concentration, t_p, as a function of distance from the origin. t_p is made more spatially uniform by the finite pulse width. The thin blue lines show the peak time from infinitesimal sources at $t = 0$ and $t = \Delta t$. Both of these show more variance as a function of x. The bottom inset shows the normalized peak concentration, $C_p(x)/C_p(x = 8$ $\mu m)$ for the pulse of width $\Delta t = 25$ ms (black) and an infinitesimal source (red). The width of the pulse reduces the variation over both space and time for cells in the FRET measurements.
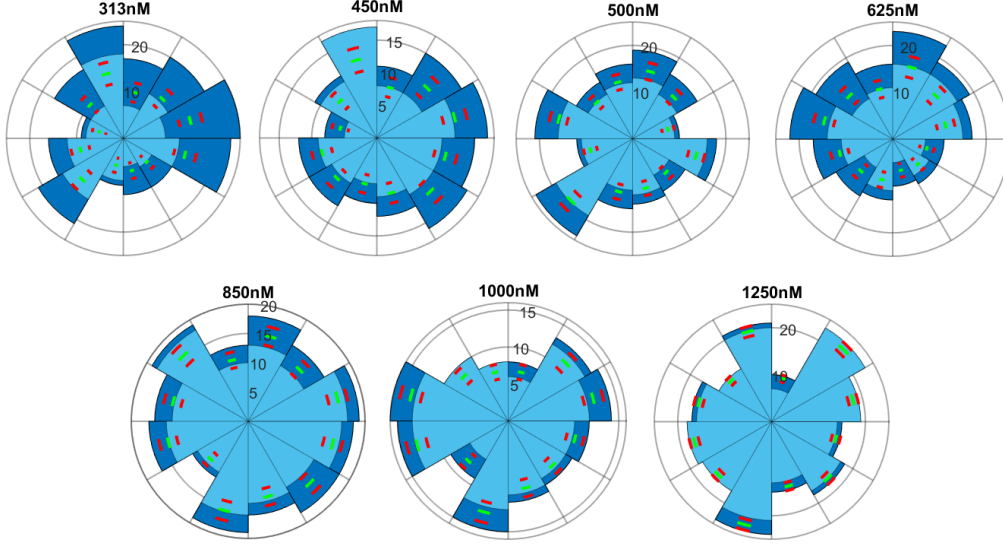
93

Figure 33: Rotational Histograms for Impulsive Serine Stimulated Tethered Cells. The data used to create these histograms was presented in chapter 4. Each histogram shows the angular location of cells at the time of peak concentration at the rotation axis. Dark blue indicates the location for all trails for each concentration and light blue indicates the trials marked as "positive" for a response according to the algorithm described in 4.3.2. The green dashes indicate the expected number of positive trials based on random binning with red dashes indicating one standard deviation. The histograms show that cell do not respond more often when they are closer to the pipette, which is closest to the bin with boundaries at 2 and 3 o'clock. Each histogram is labeled at the top by C_0, which is the serine concentration in the micropipette.
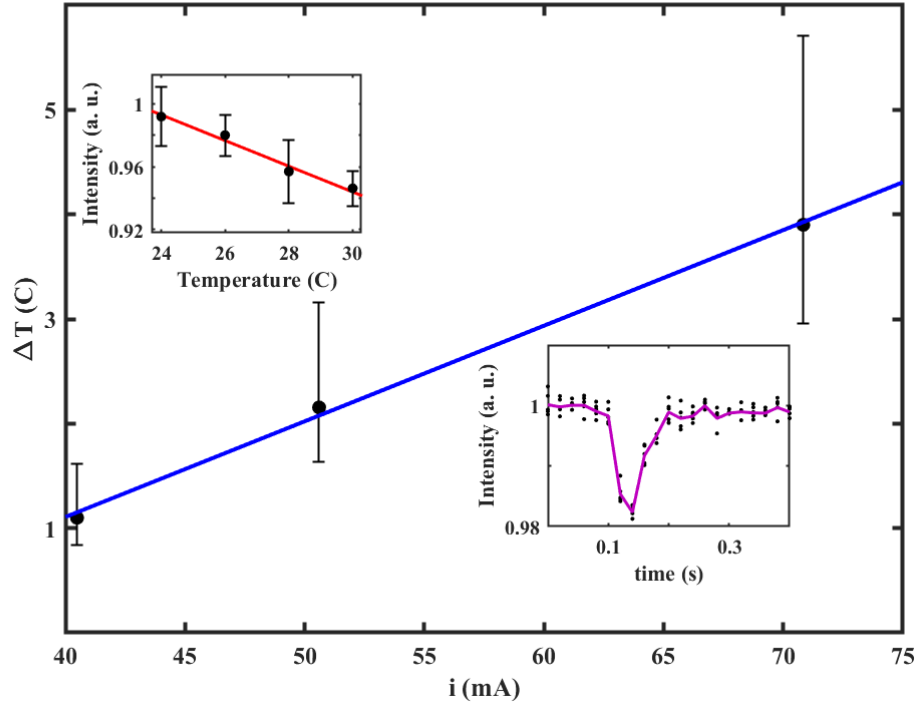
Figure 34: Temperature Calibration of a Heat Pulse. The main plot shows the max temperature experienced by a cell, vs. the current, i, supplied by the laser driver. The calibration was done by taking advantage of the temperature dependence of the fluorescence properties of fluorescein. Inset A: The relative fluorescence of fluorescein as a function of temperature. The dye was calibrated using sealed sample on our microscope. The sample was heated by a thermoelectric heater controlled by a custom code written in Labview (National Instruments, Austin TX). Inset B: An example of a heat pulse on the dye as observed using the setup described in Fig. 35 D. Dots indicate the mean fluorescence intensity, for single trials, over a $12 \times 12\,\mu$m field imaged under 100X magnification. The purple is the mean of all five trials. The frame rate was 50 Hz and the pulse duration was 50 ms.
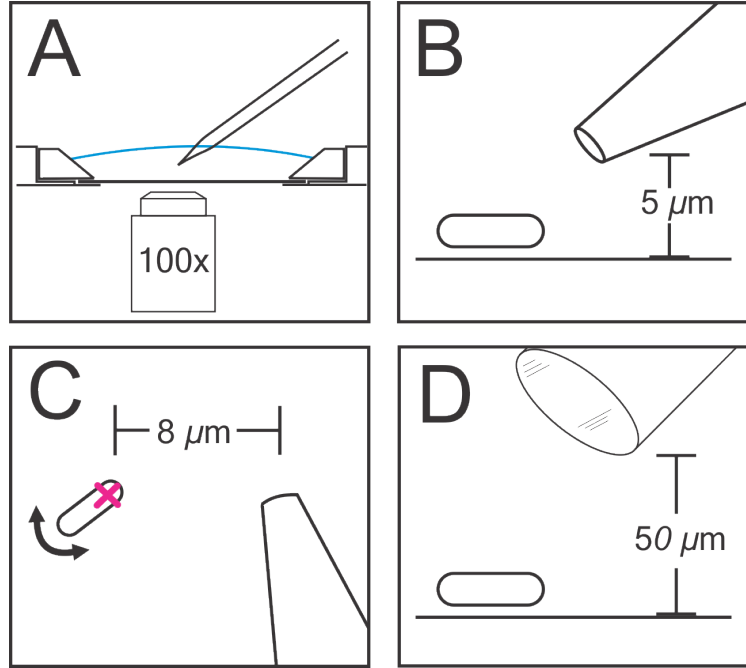
Figure 35: Experimental Setup for Impulsive Stimulation. (A) A micropipette containing a chemoattractant is positioned near a preselected bacterium from above the open chamber. The chamber is made of stainless steel and a #0 cover-slip 2.5 cm in diameter. The chamber is sealed at the bottom by a rubber gasket. The blue curved line indicates the location of the air/water interface, which is approximately 5 mm above the bottom. All imaging was made using a 100X objective. (B-C) To minimize disturbances due to an impulse, the tip of the micropipette is placed $5\,\mu$m above the bottom surface and $8\,\mu$m to the side of the rotation axis of bacterium, which is denoted by the red "x" in (C). (D) For temperature stimulation, a cleanly cleaved optical cable is positioned $50\,\mu$m directly above the bacterium.
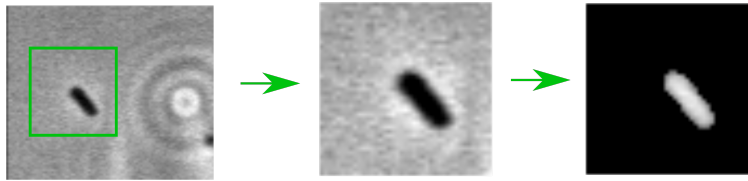
Figure 36: Image Cleanup for Processing. Videos of rotating cells are first cropped around the rotation axis. The video is then inverted to make the bacterium the brightest object in the frame. Finally the video is thresholded to remove the background.
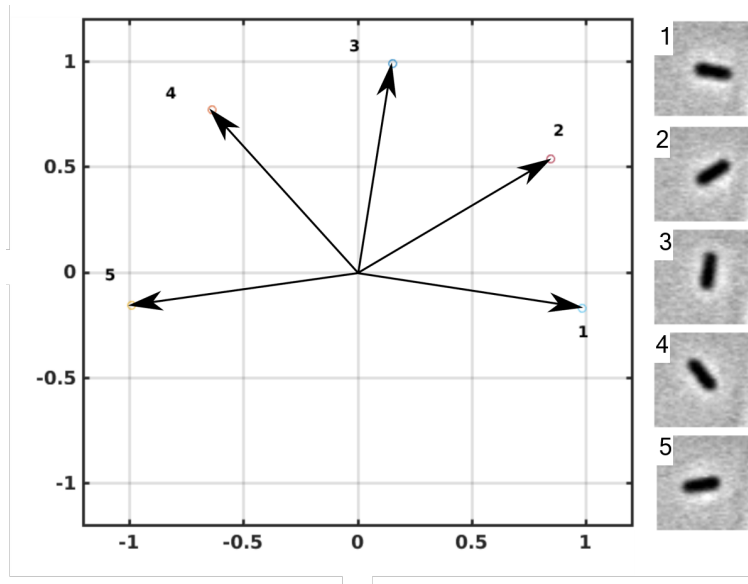
Figure 37: An Example of The Image Analysis Algorithm for Rotating Cells. The orientation vector for each frame on the right is shown. The cell is rotating CCW with the frames captured at 50 Hz.
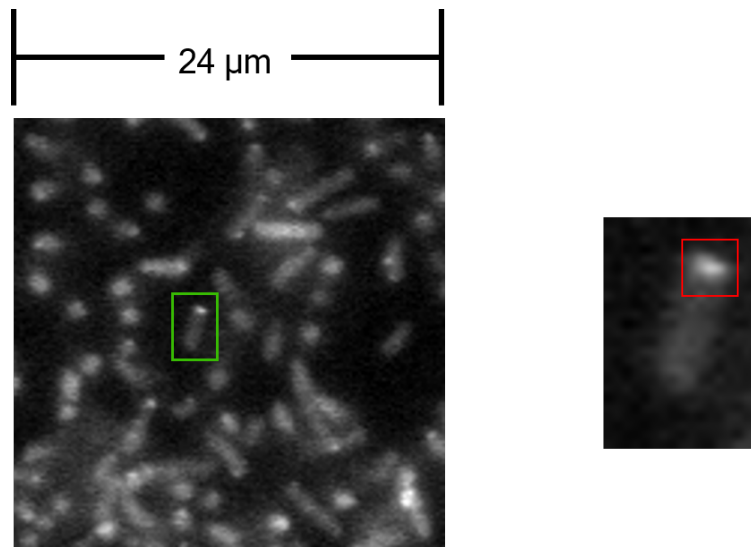
Figure 38: An Example Frame From A Video of A FRET Measurement. The region inside the green box is enlarged to the right to show a single cell with a bright punctum. The red outline denoted the 3×3 box that is searched for the brightest pixel.

APPENDIX B CALCULATIONS

B.1 CALCULATIONS ON THE THRESHOLD OF DETECTION

The method that Adler [10] used to determine the threshold of detection is shown in Fig. 39. This plot should be used to judge experimental uncertainty for the threshold values of 7 nM for serine and 15 nM for aspartate given in Ch. 4. A more conservative estimate instead places an upper bound on the threshold using the lowest concentration that showed a detectable response, which is $C^* < 19 \pm 3$ nM for serine and $C^* < 39 \pm 5$ nM for aspartate.

The statistical method used to determine the threshold number of bindings requires an algorithm to score each trial as "positive" or "negative" for response. The principle requirement of the algorithm is that it is based on the observed behavioral change associated with a chemotactic stimulus. Also, large variability in cell behavior place the additional requirement that the probability of a false positive can be determined. Observation of Fig. 20 shows that the peak bias is roughly at $t_{max} = 460$ ms after the pulse. Let $\omega(t_i)$ denote the rotation state of the cell at time t_i and $\overline{\omega(t_i)}$ denote the time average over a widow of length τ centered on t_{max}. The algorithm used marks a trial positive if $\overline{\omega(t_i)} > \Phi_0$, and negative otherwise. Here Φ_0 the individual cell bias, not that of the entire population, and τ is the time at which the autocorrelation of $\omega(t_i)$ first reaches a value of 0.5.

We found that if only a single frame is used to score, the frame picked influences the final result, so it is instead desirable to average over multiple frames. However, the longer the window becomes, the more difficult it is to estimate the rate of false positives. For a single frame, the probability that the cell is in the CCW direction is simply Φ_0, by definition. If the window is short enough, however, the probability that the average is greater than the background is roughly the probability that a single frame is 1, since there is a high correlation in short times. Fig. 40 shows the autocorrelation function plotted for several cells. We use τ calculated for each cell as the averaging window for that cell, meaning then that the rate of false positives is roughly equal to Φ_0.

B.2 CALCULATING CHEY-P CONCENTRATION CHANGE USING BIAS DATA

The output stage of the chemotaxis network, i.e. the motor response to variations in CheY-p concentration, has been carefully measured by Cluzel et al. [28]. They use a Hill function to characterize the CW bias as a function of CheY**, a permanently active mutant of CheY, with the result:

$$\Phi_{CW}(Y) = 1/(1 + (K_Y/Y)^H) \,,$$

where Y is the concentration of CheY**, $K_Y = 3.2$ μM is the dissociation constant, and $H \simeq 10$ is the Hill coefficient. For this investigation, we found it is more convenient to parameterize the response function using the hyperbolic tangent function:

$$\Phi_{CW}(Y) = (1 + \tanh((Y - K_Y)/(2K_Y/H) \,,$$

where K_Y and H are as in Ref. [28]. Fig. 41 shows that the two schemes are nearly indistinguishable.

B.3 A MODEL OF CHEMOTAXIS BY TU, SHIMIZU AND BERG

The model begins with the assumption that the cell contains n individual and identical "functional units" of a given receptor type. Each one of these units contains N binding sites, i.e., receptor homodimers. A unit is MWC-like in that the receptors of a unit are all either active or inactive. Thus we calculate the activity of the unit as a whole rather than individual receptors.

The activity S of the unit is described by the Hamiltonian $H = (E + \epsilon \sum_i^N \sigma_i)S + \mu \sum_i^N \sigma_i$, where S and ligand binding σ_i takes discrete values 0 or 1. The partition function for this Hamiltonian can be calculated with the result

$$Z = (1 + e^{-\mu})^N + e^{-E}(1 + e^{-\mu-\epsilon})^N \,,$$

where the Boltzmann factor β is assumed to be unity. Using Z one can calculate the mean activity, a, of an effective functional unit,

$$a \equiv \overline{S} = \frac{1}{1 + \exp\left[N(f_m + f_L)\right]} \ , \tag{B.1}$$

where $f_L = \ln\left[(1 + C/k_I)/(1 + C/k_A)\right]$ may be called the free energy of ligand binding, $k_I = C\exp(\mu)$ and $k_A = C\exp(\epsilon + \mu)$ are respectively the dissociation constant of an inactive and active receptor unit, and $f_m = E/N$ the free energy of methylation.

For the partition function Z to be thermodynamically meaningful, it is implicitly assumed that ligand binding/unbinding is rapid compared to the conformational change of receptors and adaptation dynamics. In this fashion, ligand binding is treated as at thermodynamic equilibrium with a defined free energy f_L. The methylation free energy f_m is a slow variable that acts in long times to bring the activity, a, back to its steady-state value, a_0.

To see how ligand binding results in a change of CheY-p concentration in a cell, we invert the activity in Eq. B.1 by writing

$$\ln \frac{a}{1 - a} = N(f_m + f_L) \ .$$

A small variation near the steady state of activity a_0 is given by

$$\Delta a(t) \equiv a(t) - a_0 = -a_0(1 - a_0)N(\Delta f_m(t) + \Delta f_L(t)) \ . \tag{B.2}$$

The observed adaptation in chemotaxis is due to methylation. After a stimulation, we require the activity to return to the stimulus level, i.e. we expect that $\Delta a(t)$ should relax to zero. Phenomenonologically we write

$$\Delta a(t) = \Delta a(0^+)e^{-\frac{t}{t_m}} \ , \tag{B.3}$$

where t_m is the methylation time and $\Delta a(0^+)$ is the activity change at $t = 0^+$ when a step-wise stimulation is applied. It follows from Eq. B.2,

$$\Delta a(0^+) = -a_0(1 - a_0)N\Delta f_L \ , \tag{B.4}$$

where, due to slow adaptation, $\Delta f_m(0^+) = 0$ and $\Delta f_L = \ln\left[(1 + C/k_I)/(1 + C/k_A)\right]$.

As mentioned, the quantity of interest in an experiment is the change in the CheY-p concentration, $y(t)$, at the receptor array. We assume that only active receptor units contribute to replenishment of CheY-p molecules. The equation of motion for y(t) is then given by,

$$\frac{dy}{dt} = k'_a n' - \frac{y}{t_z},$$

where n' is the number of active functional units, k'_a is the phosphorylation rate for an active unit, and t_z is the dephosphorylation time. Given a total number of functional units, n, $a = n'/n$ on average, thus the above equation may be written in terms of the average activity:

$$\frac{dy}{dt} = k_a a - \frac{y}{t_z}, \tag{B.5}$$

where $k_a = nk'_a$. The steady state concentration is given by $y_0 = k_a t_z a_0$. The time dependent solution is solved using Eq. B.4 and B.3, and again assuming a step in ligand concentration at $t = 0$:

$$\Delta y(t) \equiv y(t) - y_0 = k_a \int_0^t e^{-\frac{t-t'}{t_z}} \Delta a(t') dt'.$$

$$= -k_a a_0 (1 - a_0) N \frac{t_z t_m}{t_m - t_z} \Delta f_L(C) \left(e^{-\frac{t}{t_m}} - e^{-\frac{t}{t_z}} \right) \tag{B.6}$$

Finally, by taking the time derivative of Eq. B.6, we obtain the Green's function for the model, which was given in the main text Eq. 5.3:

$$G_Y(t) = k_a N a_0 (1 - a_0) \frac{t_z t_m}{t_m - t_z} \left(\frac{1}{t_m} e^{-\frac{t}{t_m}} - \frac{1}{t_z} e^{-\frac{t}{t_z}} \right). \tag{5.3}$$

The solution of Eq. B.5 for an arbitrary ligand concentration profile is then given by the convolution of Eq. 5.3 with $f_L(C(t))$, or equation 5.2 in the main text.

B.4 A MODIFICATION TO THE TSB MODEL

We require a modification to the model that has the effect of an increased CheZ activity in response to the binding of chemoattractant. We modify Eq. B.3. by the inclusion of an additional term:

$$\Delta a(t) = \Delta a(0^+) \left(-\gamma \delta(t) + e^{-\frac{t}{t_m}} \right) , \tag{B.7}$$

where the use of the delta function accounts for the fact that the enhanced CheZ activity happens on a much faster time-scale than the adaptation by methylation. Use of Eq. B.7 in the convolution of Eq. B.6, followed by a time derivative, yields Eq. 5.6 in the main text.

B.5 SIGNAL PROPAGATION INSIDE A BACTERIUM

We wish to solve the diffusion equation for the CheY-p concentration $Y(x,t)$ inside a cell,

$$\frac{\partial Y(x,t)}{\partial t} = D \frac{\partial^2 Y(x,t)}{\partial x^2} - \lambda Y(x,t) \tag{5.5}$$

subject to the boundary conditions:

$$Y(0,t) = y_0 + \Delta y(t)$$
$$\left. \frac{\partial Y}{\partial x} \right|_{x=L} = 0$$
$$Y(x,0) = Y_0(x)$$

where $\lambda \geq 0$ is the rate of spontaneous decay, $D > 0$ is the diffusion coefficient, $L > 0$ is the length of the cell and $Y_0(x)$ is the steady state solution for a constant concentration at $x = 0$. The since the source is a sum of a constant term and a time dependent term, the concentration, $Y(x,t)$, has the same form:

$$Y(x,t) = Y_o(x) + Y_t(x,t) . \tag{B.8}$$

The steady state solution is found by setting $\Delta y(t) = 0$ and the left hand side of Eq. 5.5 to zero. The result is

$$Y_o(x) = y_o \frac{\cosh\left(\sqrt{\frac{\lambda}{D}}(x - L)\right)}{\cosh\left(\sqrt{\frac{\lambda}{D}}L\right)} \tag{B.9}$$

where constant y_o is related to the mean CheY-p concentration in the cell, $\overline{Y}$. Here we assume that $\overline{Y} = 3\ \mu\text{M}$ as measured in Ref. [28]:

$$\overline{Y} = \frac{1}{L}\int_0^L Y_0(x)\, dx = [Y_p] = 3\ \mu\text{M} . \tag{B.10}$$

Solving this, we find that the constant y_0 is related to $\overline{Y}$ by

$$y_o = \sqrt{\frac{L^2\lambda}{D}} \frac{\overline{Y}}{\tanh\left(\sqrt{\frac{\lambda}{D}}L\right)} . \tag{B.11}$$

Now we must tackle the time dependent solution. The first step is to take care of the inhomogeneous boundary condition at $x = 0$. Let

$$C(x,t) = Y_t(x,t)\, e^{\lambda t} - \Delta y(t)\, e^{\lambda t} \cos\left(\pi\frac{x}{L}\right) .$$

This function is the solution to an *inhomogeneous* differential equation, but with homogeneous boundary conditions:

$$\begin{aligned}
\frac{\partial C(x,t)}{\partial t} &= D\frac{\partial^2 C(x,t)}{\partial x^2} - \left(\frac{\partial\Delta y}{\partial t} + \left(D\left(\frac{\pi}{L}\right)^2 + \lambda\right)e^{\lambda t}\Delta y(t)\right)\cos\left(\frac{\pi}{L}x\right) \\
&= D\frac{\partial^2 C(x,t)}{\partial x^2} + J(x,t) \tag{B.12} \\
C(0,t) &= 0 \\
\left.\frac{\partial C}{\partial x}\right|_{x=L} &= 0 \\
C(x,0) &= 0 \quad .
\end{aligned}$$

The Green's function for this problem can be found in Ref. [95], and is given by

$$G(x, x', t, t') = \frac{2}{L}\sum_{n=1}^{\infty} \sin(k_n x')\sin(k_n x)e^{-Dk_n^2(t-t')}$$

where

$$k_n = \frac{(2n+1)\pi}{2L} \ .$$

Given the Green's function, the time dependent solution is solved by integration:

$$\int_0^t dt' \int_0^L dx' \, G(x,x',t,t') J(x',t')$$

Working out the details of the integration and transforming back to Y, we find the solution to Eq. 5.5 is

$$P(x,t) = y_o \frac{\cosh\left(\sqrt{\frac{\lambda}{D}}(x-L)\right)}{\cosh\left(\sqrt{\frac{\lambda}{D}}L\right)} + \frac{2D}{L} \sum_{n=1}^{\infty} k_n \sin(k_n x) e^{-(Dk_n^2+\lambda)t} \int_0^t \Delta y(t') e^{(Dk_n^2+\lambda)t'} dt'$$

(B.13)

The "input" to this equation, $\Delta y(t)$, is the "output' of the TSB model, Eq. 5.2. It was found that the first 4 terms were sufficient for plotting and fitting purposes, and the solution did not noticeably change with the inclusion of more terms. We used $L = 3 \ \mu$m for the length of the cell, and $D = 7 \ \mu^2$/s, which was estimated from the diffusion coefficients listed in ref. [78] and the measurement in ref. [28].
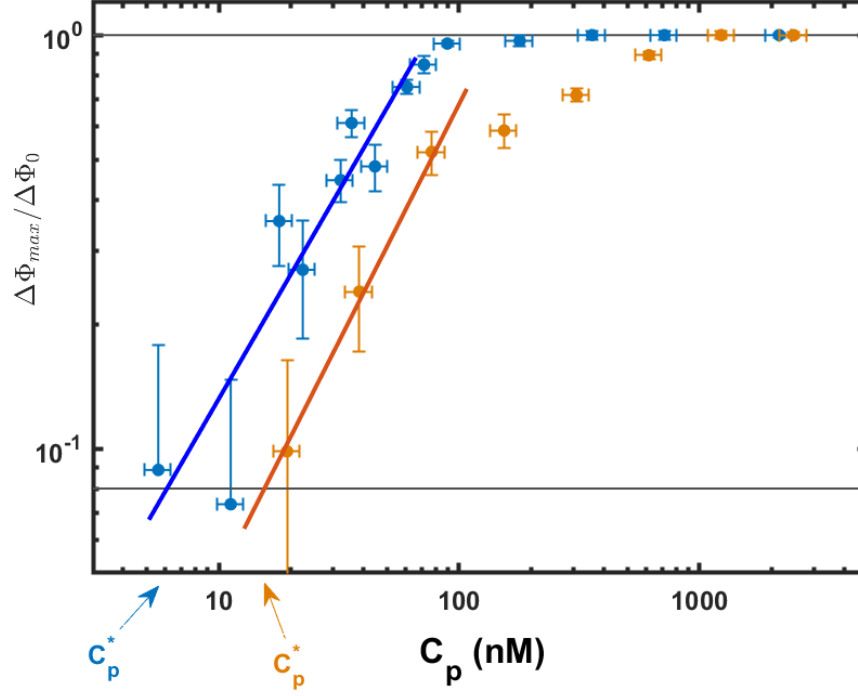
Figure 39: The Population Response R Plotted on a Log-Log Scale. Blue dots are from impulsive serine measurements and orange dots are form impulsive aspartate. The lines extrapolate the data to 8%, which was the average scaled standard deviation of Φ_0. The lines at $\Delta\Phi_{max}/\Delta\Phi_0 = 0.08$ and 1.0 are aids to the eye.
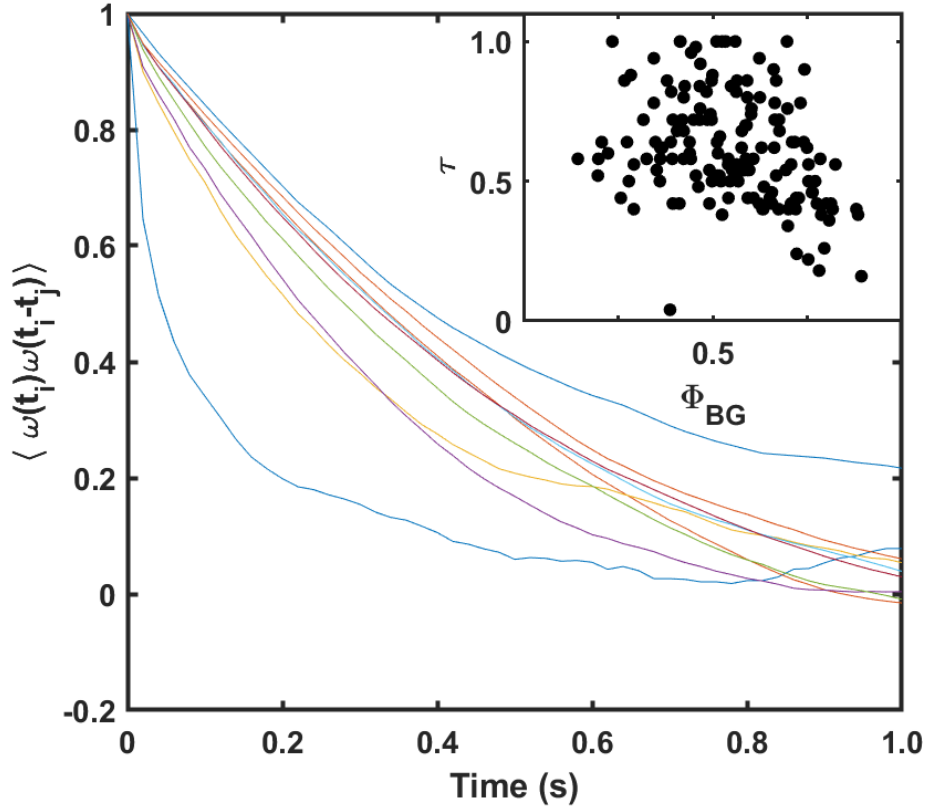
Figure 40: An Example of The Autocorrelation of $\omega(t)$. The traces shown are from bacteria exposed to $C_0 = 1.25 \ \mu M$ serine. Cells that frequently switch will have a rotation state with a rapidly decaying autocorrelation. However this is not correlated with the CCW bias. The inset shows the correlation time, τ, plotted against the individual background CCW bias, Φ_0 for all cells exposed to serine. There is no observable correlation between the autocorrelation time τ and background bias Φ_0.

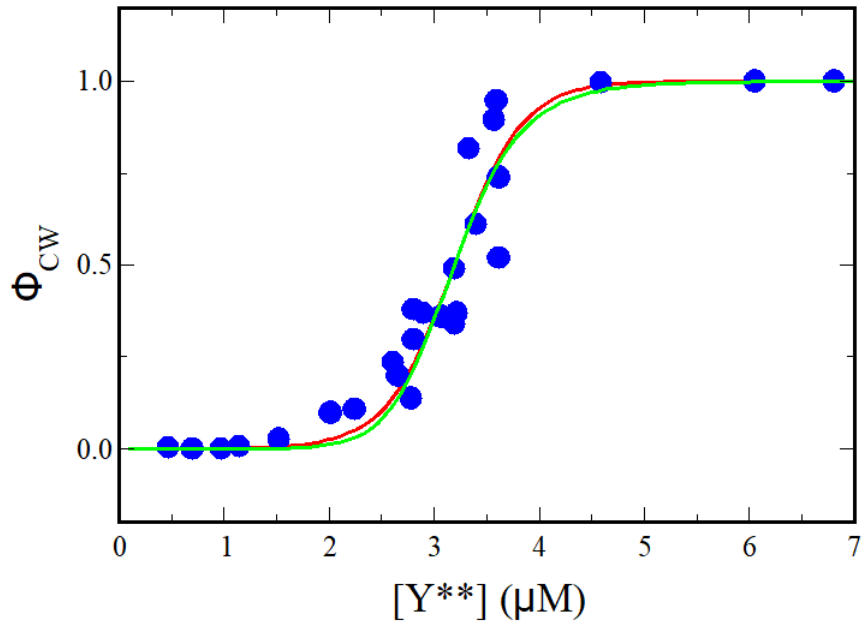Figure 41: *E. Coli* Flagellar Motor Bias. The blue dots are the data from Ref. [28], the green curve is a fit using the Hill function as in the same reference, and the red curve is our parameterization using the hyperbolic tangent function discussed in the main text.

BIBLIOGRAPHY

[1] L. Turner, L. Ping, M. Neubauer, and H.C. Berg. Visualizing flagella while tracking bacteria. *Biophys. J.*, 111:1–10, 2016.

[2] T Hirano, S Yamaguchi, K Oosawa, and S Aizawa. Roles of flik and flhb in determination of flagellar hook length in salmonella typhimurium. *Journal of Bacteriology*, 176(17):5439–5449, 1994.

[3] L. Turner, W. S. Ryu, and H. C. Berg. Real-time imaging of fluorescent flagellar filaments. *J Bacteriol*, 182:2793–2801, 2000.

[4] R.M. Macnab. Bacteria flagella rotating in bundles: a study in helical geometry. *Proc. Natl. Acad. Sci. USA*, 74:221–225, 1977.

[5] R.M. Macnab and M.K. Ornston. Normal-to-curly flagellar transitions and their role in bacterial tumbling: stabilization of an alternative quaternary structure by mechanical force. *J. Mol. Biol.*, 112:1–30, 1977.

[6] N.C. Darnton, L. Turner, S. Rojevsky, and H.C. Berg. On torque and tumbling in swimming escherichia coli. *J. Bacteriol.*, 189:1756–1764, 2007.

[7] Claes Weibull. Movement. In I.C. Gunsalus and R.Y. Stanier, editors, *The Bacteria: A Treatise on Structure and Function*, volume 1, chapter 4, pages 188–206. Academic Press, 1960.

[8] J. Adler. Chemotaxis in bacteria. *Science*, 153:708–716, 1966.

[9] J. Adler and M.M. Dahl. A method for measuring the motility of bacteria and for comparing random and non-random motility. *J. Gen. Microbiol.l*, 46:161–173, 1967.

[10] R. Mesibov and J. Adler. Chemotaxis toward amino acids in *Escherichia coli*. *J. of Bacteriology*, 112(1):315–326, 1972.

[11] R. Mesibov, G. Ordal, and J. Adler. The range of attractant concentrations for bacterial chemotaxis and the threshold and size of response over this range. *J. of Gen. Physiology*, 62:203–223, 1973.

[12] Wung-Wai Tso and Julius Adler. Negative chemotaxis in *Escherichia coli*. *J. Bacteriology*, 118(2):560–576, 1974.

[13] J. J. Falke J. S. Parkinson, G. L. Hazelbauer. Signaling and sensory adaptation in *Escherichia coli* chemoreceptors: 2015 update. *Trends in Microbiology*, 23:257–266, 2015.

[14] J.S. Segall, S.M. Block, and H.C. Berg. Temporal comparisons in bacterial chemotaxis. *Proc. Natl. Acad. Sci.*, 83:8987–8991, 1986.

[15] Mingshan Li and Gerald L. Hazelbauer. Cellular stoichiometry of the components of the chemotaxis signaling complex. *Biophysical Journal*, 186:3687–3694, 2004.

[16] C.A. Studdert and J.S. Parkinson. Crosslinking snapshots of bacterial chemoreceptor squads. *Proc Natl Acad Sci USA*, 101:2117–2122, 2004.

[17] Victor Sourjik and Howard Berg. Functional interactions between receptors in bacterial chemotaxis. *Nature*, 428:437–441, 2004.

[18] Peijun Wang, Cezar M. Khursigara, Lisa M. Hartnell, and Sriram Subramaniam. Direct visualization of escherichia coli chemotaxis receptor arrays using cryo-electron microscopy. *Proc. Nat. Acad. Sci.*, 104:3777–3781, 2007.

[19] V. Sourjik and H.C. Berg. Localization of components of the chemotaxis machinery of *Escherichia coli* using fluorescent protein fusions. *Mol. Microbiol.*, 37:740–751, 2000.

[20] M. Li and G.L. Hazelbauer. Core unit of chemotaxis signaling complexes. *Proc Natl Acad Sci USA*, 108(23):9390–9395, 2011.

[21] H.C. Berg and E.M. Purcell. Physics of chemoreception. *Biophys. J.*, 20:193–219, 1977.

[22] V. Sourjik and H. C. Berg. Receptor sensitivity in bacterial chemotaxis. *Proc. Natl. Acad. Sci.*, 99:123–127, 2002.

[23] Y.H. Tu, T.S. Shimizu, and H.C. Berg. Modeling the chemotactic response of *Escherichia coli* to time-varying stimuli. *Proc Natl Acad Sci USA*, 105:114855–11860, 2008.

[24] C.H. Hansen, V Sourjik, and N.S. Wingreen. A dynamic-signaling-team model for chemotaxis receptors in escherichia coli. *Proc. Natl. Acad. Sci. USA*, 107:17170–17175, 2010.

[25] H.C. Berg and R.A. Anderson. Bacteria swim by rotating their flagellar filaments. *Nature*, 245:380–382, 1973.

[26] M. Silverman and M. Simon. Flagellar rotation and the mechanism of bacterial motility. *Nature.*, 249:73–74, 1974.

[27] S.H. Larsen, R.W. Reader, E.N. Kort, W. Tso, and J. Adler. Change in directions of flagellar rotation is the basis of the chemotactic response in *Escherichia coli*. *Nature*, 249:74–77, 1974.

[28] P. Cluzel, M. Surette, and S. Leibler. An ultrasensitive bacterial motor revealed by monitoring signaling proteins in single cells. *Science*, 287:1652–1655, 2000.

[29] R.M. Macnab and D.E. Koshland. Bacterial motility and chemotaxis: light-induced tumbling response and visualization of individual flagella. *J Mol. Biol.*, 86:399–406, 1974.

[30] R.M. Macnab. Examination of bacterial flagellation by dark-field microscopy. *Journal of Clinical Microbiology*, 4(3):258–265, 1976.

[31] R.M. Macnab and H.P. Dongyeon. Asynchronous switching of flagellar motors on a single bacterial cell. *Cell*, 32:109–119, 1983.

[32] A. Ishihara, J.E. Segall, S.M. Block, and H.C. Berg. Coordination of flagella on filamentous cells of *Escherichia coli*. *J. Bacteriol.*, 155(1):228–237, 1983.

[33] K.A. Fahrner, W.R. Ryu, and H.C. Berg. Bacterial flagellar switching under load. *Nature*, 423, 2003.

[34] S. Terasawa et. al. Coordinated reversal of flagellar motors on a single escherichia coli cell. *Biophysical Journal*, 100:2193–2200, 2011.

[35] Bo Hu and Tu Yuhai. Coordinated switching of bacterial flagellar motors: evidence for direct motor-motor coupling? *Phys Rev Lett*, 110:158703, 2013.

[36] H.C. Berg and Brown D.A. Chemotaxis in escherichia coli analyzed by three-dimensional tracking. *Nature*, 239:500–504, 1972.

[37] Victor Sourjik and Ned S. Wingreen. Responding to chemical gradients: Bacterial chemotaxis. *Current Opinion in Cell Biology*, 24(2):262–268, 2012.

[38] Howard C. Berg. The rotary motor of bacterial flagella. *Annual Review of Biochemistry*, 72(1):19–54, 2003.

[39] J.R. Blake. A note on the image system for a stokeslet in a no-slip boundary. *Proc. Camb. Phil. Soc.*, 70:303–310, 1971.

[40] A.P. Berke, L. Turner, H.C. Berg, and E. Lauga. Hydrodynamic attraction of swimming microorganisms by surfaces. *Phys. Rev. Lett.*, 101:038102, 2008.

[41] H. H. Tuson and D. B. Weibel. Bacteria-surface interactions. *Solft Matter*, 9:4368–4380, 2013.

[42] S. J. Schrag and J. E. Mittler. Host-parasite coexistance: the role of spatial refuge in stabilizing bacteria-phage interactions. *Am. Naturalist*, 148(2):348–377, 1996.

[43] P.D. Frymier, R.M. Ford, H.C. Berg, and P.T. Cummings. Three-diemnsional tracking of motile bacteria near a solid planar surface. *PNAS*, 92:6195–6199, 1995.

[44] Y. Magariyama, M. Ichiba, K. Nakata, K. Baba, T. Ohtani, and S. Kudo. Difference in bacterial motion between forward and backward swimming caused by the wall effect. *Biophys. J.*, 88:3648–3658, 2005.

[45] E. Lauga, W.R. DiLuzio, Whitesides G.M., and H.A. Stone. Swimming in circles: motion of bacteria near solid boundaries. *Biophysical Journal*, 90:400–412, 2006.

[46] H.C. Berg and P.M. Tedesco. Transient response to chemotactic stimuli in *Escherichia coli*. *Proc. Nat. Acad. Sci. USA*, 72:3235–3239, 1975.

[47] M. E. Heimbrook, W. L. L. Wang, and G. Campbell. Staining bacterial flagella easily. *J. Bacteriol.*, 189:1756–1764, 2007.

[48]   Y. Imae, K. Oosawa, T. Mizuno, M. Kihara, and R.M. Macnab. Phenol: a complex chemoeffector in bacterial chemotaxis. *J. Bacteriol.*, 269:371–379, 1987.

[49]   J.H. Yuan, K.A. Fahrner, and H.C. Berg. Switching of the bacterial flagellar motor near zero load. *J. Mol. Biol.*, 390:390–400, 2009.

[50]   A.P. Petroff, X.L. Wu, and A. Libchaber. Fast-moving bacteria self-organize into active two-dimensional crystals of rotating cells. *Phys. Rev. Lett.*, 114:158102, 2015.

[51]   Tuba Altindal. *Determination of bacterial chemotaxis response functions by optical Trapping.* PhD thesis, University of Pittsburgh, 2012.

[52]   Liam F. Garrity and George W. Ordal. Chemotaxis in bacillus subtilis: How bacteria monitor environmental signals. *Pharmacology and Therapeutics*, 68:87–104, 1995.

[53]   Sarah B. Guttenplan, Sidney Shaw, and Daniel B. Kearns. The cell biology of peritrichous flagella in bacillus subtilis. *Molecular Microbiology*, 87:211–229, 2013.

[54]   Matthew Shtrahman. *Probing Vesicles Dynamics in Single Hippocampal Synapses.* PhD thesis, University of Pittsburgh, 2005.

[55]   Robert G. Endres, Olga Oleksiuk, Clinton H. Hansen, Yigal Meir, Victor Sourjik, and Ned S. Wingreen. Variable sizes of escherichia coli chemoreceptor signaling teams. *Molecular Systems Biology*, 4, 2008.

[56]   A. Paulick, V. Jakovljevic, S.M. Zhang, M. Erickstad, A. Groisman, Y. Meir, W.S. Ryu, N.S. Wingreen, and V. Sourjik. Mechanism of bidirectional thermotaxis in *Escherichia coli*. *eLife*, 6:e26607, 2017.

[57]   T. Föster. Zwischendmolekulare energiwanderung und fluoreszenz. *Ann. Phys.*, 2:55–75, 1948.

[58]   V. Sourjik, A. Vaknin, T.S. Shimizu, and H.C. Berg. In vivo measurement by fret of pathway activity in bacterial chemotaxis. *Methods in Enzymology*, 423:365–391, 2007.

[59]   Y.H. Tu. The nonequilibrium mechanism for ultrasensitivity in a biological switch: Sensing by maxwell's demons. *Proc Natl Acad Sci USA*, 105:11737–11741, 2008.

[60]   L.L. Jiang, Q. Ouyang, and Y.H. Tu. A mechanism for precision-sensing via a gradient-sensing pathway: a model of *Escherichia coli*. *Biophys. J.*, 97:74–82, 2009.

[61]   J. Monod, J. Wyman, and J.-P. Changeux. On the nature of allosteric transition: a plausible model. *J. Mol. Biol.*, 12:88–118, 1965.

[62]   J.L. Spudich and D.E. Koshland. Quantitation of the sensory response in bacterial chemotaxis. *Proc. Natl. Acac. Sci.*, 72:710–713, 1975.

[63]   D. Kentner and V. Soujik. Dynamic map of protein interactions in the *Escherichia coli* chemotaxis pathway. *Mol. Syst. Biol.*, 5:238–247, 2009.

[64]   A. Vaknin and H. C. Berg. Single-cell fret imaging of phosphatase activity in the *Escherichia coli* chemotaxis system. *Proc. Natl. Acad. Sci. USA*, 101:17072–17077, 2004.

[65]   Y. Blat, B. Gillespie, A. Bren, F.W. Dahlquist, and M. Eisenbach. Regulation of phosphatase activity in bacterial chemotaxis. *J. Mol. Biol.*, 284:1191–1199, 1998.

[66]   R. Macnab and Jr. D.E. Koshland. The gradient-sensing mechanism in bacterial chemotaxis. *Proc. Natl. Acad. Sci. USA*, 69:2509–2512, 1972.

[67]   S.P. Langley. Energy and vision. *Phil. Mag.*, 27, 1889.

[68]   M. H. Pirenne S. Hecht, S. Shlaer. Energy, quanta, and vision. *Journal of General Physiology*, pages 819–840, 1942.

[69]   J.N. Tinsley, M.I. Molodtsov, R. Prevedel, D. Wartmann, J. Espigulé-Pons, M. Lauwers, and A. Vaziri. Direct detection of a single photon by humans. *Nature Communications*, 7, 2016.

[70]   W. Marwan, P Hegemann, and D. Oesterhelt. Single photon detection by archaebacterium. *J. Mol. Biol.*, 199:663–664, 1988.

[71]   H. Mao, P.S. Cremer, and M.D. Manson. A sensitive, versatile microfluidic assay for bacterial chemotaxis. *Proc. Natl. Acad. Sci. USA*, 100:5449–5454, 2003.

[72]   William Bialek and Sima Setayeshgar. Cooperativity, sensitivity, and noise in biochemical signaling. *Physical Review Letters*, 100, 2008.

[73]   Robert G. Endres and Ned S. Wingreen. Maximum likelihood and the single receptor. *Physical Review Letters*, 103, 2009.

[74]   S. Khan, K. Amoyaw, Spudich J.L., G.P. Reid, and D.R. Trentham. Bacterial chemoreceptor signaling probed by flash photorelease of a caged serine. *Biophys. J.*, 62:67–68, 1993.

[75]   Takashi Sagawa, Yu Kikuchi, Yuichi Inoue, Hiroto Takahashi, Takahiro Muraoka, Kazushi Kinbara, Akihiko Ishijima, and Hajime Fukuoka. Single-cell e. coli response to an instantaneously applied chemotactic signal. *Biophysical Journal*, 107:730–739, 2014.

[76]   S.M. Block, J.E. Segall, and H.C. Berg. Impulse responses in bacterial chemotaxis. *Cell*, 31:215–226, 1982.

[77]   R.D. Pruves. The physics of iontophoretic pipettes. *Journal of Neuroscience Methods*, 1:165–178, 1979.

[78]   K. E. van Holde. *Physical Biochemistry*. Prentice-Hall, New Jersey, second edition, 1985.

[79]   H. Salman and A. Libchaber. A concentration-dependent switch in the bacterial response to temperature. *Nat. Cell Biol.*, 9:1098–1100, 2007.

[80]   Y. Kalinin, S. Neumann, V. Sourjik, and M. Wu. Response of *Escherichia coli* bacteria to two opposing chemoattractant gradients depend on the chemoreceptor ratio. *Journal of Bacteriology*, 192:1796–1800, 2010.

[81]   Anna Yoney and Hanna Salman. Precision and variability in bacterial temperature sensing. *Biophys. Journal*, 108:2427–2436, 2015.

[82]   D.A. Sanders and D.E. Koshland. Receptor interactions through phosphorylation and methylation pathways in bacterial chemotaxis. *Proc. Natl. Acad. Sci. USA*, 85:8425–8429, 1988.

[83]   Li Guoyong and R.M. Weis. Covelent modification regulated ligand binding to receptor complexes in the chemosensory system of escherichia coli. *Cell*, 100:357–365, 2000.

[84]   P Dunten and D.E. Jr Koshland. Tuning the responsivness of a sensory receptor via covalent modification. *J. Boil. Chem.*, 266:1491–1496, 1991.

[85]   J.R. Maddock and L. Shapiro. Polar location of the chemoreceptor complex in the *Escherichia coli* cell. *Science*, 259:1717–1723, 1993.

[86]   V. Sourjik and H.C. Berg. Binding of the *Escherichia coli* response regulator CheY to its target measured in vivo by fluorescence resonance energy transfer. *Proc. Natl. Acad. Sci.*, 99:12669–12674, 2002.

[87]   F.B. Wang, J.H. Yuan, and H.C. Berg. Switching dynamics of the bacterial flagellar motor near zero load. *Proc. Nat. Acad. Sci.*, 111(44):15752–15755, 2014.

[88]   C. N. Dominick and X.L. Wu. Rotating bacteria on solid surfaces without tethering. *Biophysical Journal*, 115(3):588 – 594, 2018.

[89]   H. Fukuoka, T. Sagawa, Y. Inoue, H. Takahashi, and A. Ishijima. Direct imaging of intracellular signaling components that regulate bacterial chemotaxis. *Science*, 7:ra32, 2014.

[90]   I. Graham and T. A. J. Duke. Dynamic hysteresis in a one-dimensional ising model: Application to allosteric proteins. *Phys. Rev. E*, 71:061923, 2005.

[91]   A J Wolfe and H C Berg. Migration of bacteria in semisolid agar. *Proceedings of the National Academy of Sciences*, 86(18):6973–6977, 1989.

[92]   Goro Kuwajima. Construction of a minimum-size functional flagellin of escherichia coli. *Journal of Bacteriology*, 170:2205–33–9, 1988.

[93]   Dieter Braun and Albert Libchaber. Trapping of DNA by thermophoretic depletion and convection. *Physical Review Letters*, 89, 2002.

[94]   Mahmut Demir and Hanna Salman. Bacterial thermotaxis by speed modulation. *Biophysical Journal*, 103:1683–1690, 2012.

[95]   Dean G. Duffy. *Green's Functions With Applications.* CRC Press, New York, 2 edition, 2015.